Universitat de Girona

DYNAMICS AND MIXING IN THE UPPER OCEAN LAYER

Jesus Manuel FIGUEROA RODRIGUEZ

Universitat de Girona

Dynamics and Mixing in the Upper Ocean Layer

by

Jesús Manuel Figueroa Rodríguez

A dissertation
submitted in partial
fulfillment of the requirements
for the degree of doctor

Directed by:

Dra. Elena Roget i Armengol, Universitat de Girona

Dr. Iossif Lozovatsky, Arizona State University

Girona, 2005

ELENA ROGET I ARMENGOL, Professora de la Universitat de Girona i IOSSIF LOZOVATSKY, Professor de la Arizona State Univeristy.

CERTIFIQUEN:

Que el Maestro en Ciencias Jesús Manuel Figueroa Rodríguez ha dut a terme, sota la seva direcció, el treball que, amb el títol Dynamics and Mixing in the Upper Ocean Layer, presenta en aquesta memòria, la cual constitueix la seva Tesi per a optar al Grau de Doctor.

Dra. Elena Roget i Armengol   Dr. Iossif Lozovatsky

Girona, juny del 2005

Para mis padres, por mostrarme el camino. Y
para Astrid, Andrea y Ana Sofia, por recorrerlo
conmigo.

Girona, 2005

Dynamics and Mixing in the Upper Ocean Layer

by

J. Manuel Figueroa Rodríguez

ABSTRACT

The response of the mixed layer depth (MLD) to short–term (synoptic) variations of atmospheric forcing in the North Atlantic Ocean was analysed using CTD data, microstructure profiling, ADCP velocities and atmospheric measurements taken during the last 12 days of April 2001 at 42 stations located close to 53 °N. The transect followed the climatological position of zero annually–averaged wind stress curl (WSC), crossing the Labrador Current and several branches and meanders of the North Atlantic Current. Atmospheric forcing was characterized by relatively high wind speeds (mean value being 10.7 ms^{-1}) and negative surface heat balance. Three strong storms were encountered during the measurements and the wind stress at drift stations reached $0.2 - 0.4$ Nm^{-2}. The averaged amplitude of Ekman transport $\langle M_E \rangle$ was about 1 m^{2}s^{-1}, but during the storms the magnitude of $\langle M_E \rangle$ went up to $3.4 - 3.5$ m^{2}s^{-1}. The meridional transport across 53 °N in the Atlantic is mainly limited to depths below the upper 200–meter layer. The ageostrophic flow in the upper layer was mainly southward and eastward. The meridional ageostrophic transports, M_{Ey}, were usually greater than those calculated using the residuals between ADCP and geostrophic velocities, M_{AG}, but were in the same direction as M_{Ey} when $|M_{AG}|$ exceeded 0.3 m^{2}s^{-1}.

The MLD (h_D) at each station was identified. The deepest observed h_D was 110 m, the mean $\langle h_D \rangle = 45$ m. The MLD was compared with the current reversal depth (CRD is the shallowest depth where the current vector changes the sign of its rotation). The mean and median estimates for CRD appeared to be very close to those for MLD, suggesting that the drift currents were mostly confined to the upper mixed layer. It was found that the MLD is correlated with the friction velocity u_*, and the correlation coefficient is 0.71 when u_* data were time advanced by 12 hrs. The correlation of MLD with the surface buoyancy flux J_b was weak. The ratio between h_D and the Monin–Obukhov length scale $L_{mo} = u_*^3 / J_b$, based on the time shifted u_*, indicates that at almost all stations $h_D / L_{mo} < 1$, suggesting the dominance of wind–induced mixing over convection. Parameterization of MLD in terms of the

Ekman scale $L_f = u_*/f$ (also with time–shifted u_*) yielded the linear dependence $h_D \approx 0.44L_f$ (for $L_f > 30$ m) with the coefficient of determination $r^2 = 0.92$. The MLD was also correlated with the "stratified Ekman scale" $L_{fN} = u_*/\sqrt{fN_{pc}}$, where N_{pc} is the buoyancy frequency in the pycnocline, assuming that the growth of MLD is arrested by buoyancy when MLD reaches L_{fN}. Using L_{fN} with time shifted u_*, the linear regression $h_D \approx 1.9L_{fN}$ was obtained with reasonable statistical confidence. Numerical calculations show that in the steady state MLD is about $1.7L_{fN}$, suggesting that the mixed layer at most stations may have achieved or come close to achieving an equilibrium state.

Techniques for the general processing of microstructure data were developed and compared to those recommended in the literature. The microstructure data obtained were used to estimate the turbulent kinetic energy dissipation rate ϵ.

Mixing layer depth (h_ϵ) is defined as the layer where $\epsilon > 10^{-7}$ Wkg^{-1} and below which dissipation rapidly decreases to $\epsilon > 10^{-7}$ Wkg^{-1}. Mixing and mixed layers are found to be highly correlated $[h_\epsilon = 0.97h_D$, with $r^2 = 0.96]$ because, during the cruise, the mixed upper layer was generated predominantly by active atmospheric forcing.

Probability distributions of the kinetic energy dissipation rate (ϵ) show that, for $z > 16$ m, it is lognormal. In the near–surface layer, where measurements are strongly affected by waves and also possibly contaminated by ship movement, the distribution departs from lognormality. The corresponding mean and median values of ϵ are $\langle\epsilon\rangle = 2.2\times10^{-6}$ Wkg^{-1} and $med\,(\epsilon) = 1.5\times10^{-7}$ Wkg^{-1}. Turbulent diffusivity (K_b), the gradient Richardson number (R_i) and buoyancy Reynolds number (R_{eb}) also present a lognormal distribution. The median of the buoyancy Reynolds number $med(R_{eb}) = 4000$ is high, indicating energetic turbulence within the mixing layer. The R_i distribution function also shows high probability of shear instability in the upper weakly–stratified layer, where $med(R_i) = 0.1$ and the probability of $R_i < 0.25$ is above 60%. It appears that the depth where R_i is close to 0.25 roughly corresponds to the mixing layer depth h_D, suggesting that local shear instability may play a comparable role in the turbulence generation, specifically in the lower part of the mixing layer.

Momentum and buoyancy fluxes were used to explore different scalings for the

vertical structure of $\epsilon(z)$. When only wind induced shear stress is considered, it is found that the vertical structure of $\epsilon(z)$ is not reasonably represented, but if buoyancy production is included, fitting improves considerably. A better fitting was obtained with two approaches based on the similarity theory. First, by considering a weighting factor of 0.6 for buoyancy flux, a parameterization of the form $\epsilon(z) = 2.6\epsilon_1(z) + 0.6J_b$ is obtained, where $\epsilon_1(z) = u_*/\kappa z$ is the law of the wall. Second, a very close correspondence to the data is also obtained when it is assumed that all dissipation above ϵ_1 is due to buoyancy production of forced convection, in this case $\epsilon(z) = \epsilon_1(z) + 3.7J_b$.

The column–integrated dissipation rate $\widetilde{\epsilon}_{int}$ over the mixing layer may account, on average, for about 5% of the wind work at 10 m above the sea surface E_{10}. The ratio $\widetilde{\epsilon}_{int}/E_{10}$ also shows a positive correlation with MLD, indicating the increased column averaged dissipation at a higher MLD. This calls for a rethinking of the commonly used modelling assumption of the proportionality between the buoyancy flux due to entrainment and the rate of wind work imparted on the surface.

Different combinations of numerical values of governing parameters commonly used in various versions of the Munk-Anderson [1948] type formulas were analyzed to parameterize the diffusivity K_b as a function of R_i. For the turbulent Prandtl number, an inverse function on R_i ($P_{rt} = \alpha_t = \left(1 - \frac{R_i}{R_{i\beta}}\right)^{-r}$ was adopted with $r = 1$) and the critical $R_{i\beta} = 0.05$ or 0.1. The exponent p in formula $K_b = \left(K_0/\left(1 + \frac{R_i}{R_{icr}}\right)^p\right)P_{rt}^{-1}$, which is used to parameterize the eddy viscosity, was assigned a value of 0.5 by different authors. It was shown that $p = 1$ makes $K_M \sim \epsilon/N^2$ at $R_i >> R_{icr}$, and the Ozmidov scale serves as the main turbulent length–scale for such a dependence of $K_b(R_i)$. In non–stratified shear flow, $p = 1$ leads to the Tchen (1954) shear scales. These links give theoretical support to $p = 1$ compared to the other mostly empirical values of p. It was also suggested that $p = 2/3$ specifies another turbulent length scale $L_R = (\epsilon/NS_h)^{1/2}$ that separates the inertial and production subranges when they appear in spectra of turbulent kinetic energy. The use of $p = 2/3$ and/or $p = 1$ links $K_b(R_i)$ to specific spectral structures of turbulent fluctuations, when more traditional values of p (0.5,1.5, and 2) do not.

The best fit to the experimental data was obtained with $R_{icr} = 0.1$ and $Ri = 0.1$ for $p = 1$, but $R_i = 0.05$ works better for $p = 2/3$. When turbulence in the

upper layer is mainly driven by wind stress, the diffusivity K_b can be specified using friction velocity at the sea surface, which leads to $K_{sf}(z) = \kappa u_* z^{-1}$. A simple parameterization of K_b ($\frac{K_b}{ku_* z} = 1 - \frac{R_i}{R_{icr}} + \frac{5 \times 10^{-4}}{\kappa u_* z (1 - 5 R_i)^{2.5}}$) gives a successful fit to the bin–median estimates of the normalized diffusivity.

Dynamics and Mixing in the Upper Ocean Layer
by
J. Manuel Figueroa Rodríguez
RESUM

En aquest treball s'estudia la resposta de la capa de barreja oceànica al forçament atmosfèric considerant les dades obtingudes durant 12 dies d'abril del 2001 a 42 estacions diferents a través de l'Atlàntic nord seguint aproximadament la latitud de 53ºN. Aquestes dades inclouen, a més de les variables atmosfèriques, mesures de CTD, velocitats mesurades amb ADCP i dades de microestructura obtingudes amb un perfilador de caiguda lliure. En aquest últim cas, s'han desenvolupat noves tècniques de processament de les dades que també es presenten aquí.

El transsecte estudiat segueix la posició climatològica del rotacional mitjà anual del vent igual a zero i travessa el corrent del Labrador i algunes branques i meandres del Corrent Atlàntic Nord. El forçament atmosfèric durant la campanya es va caracteritzar per vents relativament intensos i fluxos superficials de calor negatius, tot i que, tal com es dedueix de la comparació del gruix de la capa de barreja amb la longitud de Monin-Obukov, la barreja induïda pel vent va dominar sobre la convectiva pràcticament durant tot el transsecte. Sota aquestes condicions s'ha estudiat el transport d'Ekman i el flux ageostròfic i s'ha arribat a la conclusió que el transport meridional estava limitat principalment als 200 m superiors de la columna d'aigua. Els corrents ageostròfics en la capa superior anaven principalment cap al sud i cap a l'est. El gruix de la capa de barreja a cada estació també coincideix en gran mesura amb la fondària mínima on el corrent canviava el sentit de rotació.

S'ha trobat que la fondària de la capa de barreja, h_D, estava altament correlacionada tant amb l'escala d'Ekman com amb l'escala d'Ekman estratificada, L_{fN}; la relació trobada, en aquest últim cas ha estat $h_D = 1,9L_{fN}$. D'acord amb alguns càlculs numèrics que mostren que en estat estacionari $h_D = 1,7L_{fN}$, aquest resultat suggereix que quan es van fer les mesures la capa de barreja en la majoria d'estacions estava pròxima a un estat d'equilibri.

En base als càlculs efectuats de la velocitat de dissipació de l'energia cinètica turbulenta (ϵ) a partir del cisallament de petita escala, s'ha distingit el gruix de la capa on la turbulència era activa, h_ϵ, del de la capa de barreja. S'ha trobat que

ambdues fondàries, però, també estaven altament correlacionades durant la campanya. La distribució de probabilitat de ϵ per a $z > 16$ m ha resultat ser lognormal. També presenten una distribució lognormal la difusivitat turbulenta, el nombre de Richardson per al flux mitjà, R_i, i el nombre de Reynolds de la flotabilitat, R_{eb}. A partir de l'anàlisi d'aquestes distribucions es discuteix la naturalesa de la barreja turbulenta la qual, considerant la mediana del nombre R_{eb} (4000) es veu un cop més que era majoritàriament activa. En la mateixa línia, la probabilitat de $Ri < 0.25$ durant la campanya s'ha trobat que era superior al 60%.

A partir de les dades atmosfèriques s'han calculat el fluxos de moment i de calor a través de la superfície i s'han explorat –basant-se en la teoria de similitud– diferents escalats per a l'estructura vertical mitjana dels valors mesurats d'ϵ i es fa una proposta concreta per a casos anàlegs a l'estudiat.

Calculat el valor de la integral d'ϵ a la capa de barreja es veu que aquest correspon aproximadament a un 5% del treball del vent a 10 m per sobre el nivell superficial, però el valor mitjà en cada estació està correlacionat amb la fondària de la capa de barreja. Aquests resultats semblen indicar que, en contra del que es considera habitualment, un augment en la dissipació mitjana de la capa de barreja indica una capa de barreja més profunda.

Finalment, seguint la línia introduïda per Munk-Anderson, s'han analitzat diverses formulacions de la difusivitat turbulenta en funció de Ri comparant-les amb les dades mesurades. Considerant la bondat de l'ajustament però també les implicacions teòriques subjacents, es proposa una nova parametrització.

ACKNOWLEDGMENTS

Diversae linguae habent diversum modum loquendi

San Agustín, I, 39, 3-2

During the developing of my thesis there were many persons who were very helpful, without their invaluable help I would have never been able to accomplish this work. My acknowledgments goes to all that people, but faced with the impossibility of naming all, I would like to take the opportunity to make an explicit recognition to some of them.

First, I would like to express my gratitude to my supervisors, Dra. Elena Roget i Armengol from the Universitat de Girona and Iossif Lozovatsky from the Arizona State University, whose expertise on data processing, their understanding of turbulence in natural water systems, and patience in their guideance have made this experience more valuable. Thanks to both of you for your invaluable suggestions.

Agraïments

El dia que vaig arribar a Girona vaig marcar un número de telèfon equivocat i vaig rebre com a "benvinguda" les següents paraules: 'sucio extrangero, vuélvete a casa'. Ganes de fer-ho no em van faltar, però vaig considerar que era necessari més que un llunàtic per a que desistís. No vaig fer-ho i avui dia me n'alegro. Després de quatre anys per aquestes contrades puc dir que he fet molts i molt bons amics als que recordaré sempre amb afecte. Sembla que el clixé "Girona té mala entrada, però pitjor sortida" es compleix fil per randa en el meu cas. Trobaré molt a faltar aquesta petita i bonica ciutat i als molt i molt bons amics que hi he fet.

Aquí hauria de posar una frase una mica més original que: "són moltes les persones a les que he d'agrair el seu recolzament durant la meva estada a Girona, davant la impossibilitat d'anomenar-los a tots, etc." Bé, ja està. Aquí queda la frase dita i ..el meu agraïment per a tots, però especialment per a:

Carmen Ortega i família, Ramon i Alexandra, Carles i Marianna i la canalla: Aina, Jofre, Xavier, Albert i Oriol. Gràcies a tots per obrir les portes del seu cor i de la seva casa per a la meva família i per a mi. Ja ens veurem.

A Quim Pérez, per la seva gran ajuda, els llibres deixats, les converses al Cafè Royal, l'intercanvi d'ironies i comentaris àcids. Suposo que algun dia superaràs la por de visitar Mèxic. T'esperarem.

També agraeixo a Xavier Casamitjana, Mercè, Laia i Júlia per la hospitalitat que ens van oferir, per els carnestoltes que vam compartir i les increïbles passejades per les meravelloses muntanyes de la Garrotxa.

A Xavi Sánchez, per les converses tan amenes acompanyades de tabac i cafè durant les quals vam arreglar mig món. L'altra meitat l'arreglarem quan vagis a visitar–nos. Agraeixo també la calidesa de la seva companya Teresa i els somriures de Mariona.

A la Teresa Serra, per tenir oberta la porta del seu despatx i estar sempre disposada a escoltar quan algun problema em rondava pel cap i suggerir solucions.

També pel seu interès per la cuina del meu país i per compartir les seves receptes catalanes amb mi. A Jordi, Queralt i Mireia per les bones estones que vam passar junts.

A l'Elena Roget, Pere Drou, Anna i Gemma, per haver-nos ensenyat amb entusiasme la Cultura Catalana (passejades per la muntanya, cavalcades de reis, els castellers i les desfilades de gegants i cap grossos) a més d'organitzar sopars catalano-mexicans.

A l'Anna Espígol, per les classes gratuïtes de selecció, identificació i cuina de bolets, preparació de bombons i, a més, la seva eficient ajuda en resoldre els petits problemes.

A l'Eduard Vidal, que encara que lent sempre solucionà els problemes informàtics. Gràcies Eduard i sort amb el nou món que vols organitzar en el teu temps lliure.

Ala Judit Molera, per les llargues i tan interessants converses sobre la seva cultura i la meva. D'acord, la conserva ha de ser un mica amargant. Com veus al final tot s'aclareix.

I finalment, però amb igual calidesa a les famílies Cercas–Mas, Feixas–Maneu, Coll–Presa, Palma–Gilbert, Lejerén i Riera–Torró; a ala Lluisa i en Xicu i a tots els pares, mares i nens de l'escola Annexa i el CAP Moltilivi amb els que vam compartir molt bones estones.

Bé, crec que no està gens malament per a algú que va tenir tan mal començament a l'arribar a Girona.

Agradecimientos

A Lina Zúñiga, Julieta Castro e Ivonne Best que con eficiencia me ayudaron a solventar los problemas burocráticos que de tanto en tanto surgieron, pero sobre todo porque que siempre intercalaron mensajes alentadores en sus comunicaciones oficiales.

A todos los que en el Departamento de Oceanografía Física de CICESE que de diversas maneras me apoyaron, pero en particular a Guido Marinone, Edgar Pavía, Paco Ocampo, Julio Sheinbaum, Chema Robles, Armando Trasviña, Alberto Amador, Joaquín García y Carolina Morales.

A Roel Martínez, un mexicano entrañable atrapado por Girona, con el que compartí la nostalgia por nuestro terruño y las diatribas contra la ramplona derecha mexicana. "Quedem a Oaxaca per unes gambes cruas amb llimona a la platja". Y recuerda: Nu jini ra iin yaa kuu kata ra iin.

But a curiosity of my type remains after all the most agreeable of all vices — sorry, I meant to say: the love of truth has its reward in heaven and even on earth. —
Nietzsche, Beyond Good and Evil, 45

El razonamiento no es más que un relámpago en medio de una larga noche. Pero ese relámpago lo es todo.
Henri Poincaré

TABLE OF CONTENTS

LIST OF FIGURES

<div align="right">

CHAPTER 1

Introduction

</div>

This work is about the mixing dynamics of the Upper Ocean Layer (UOL) –a concept to be defined more precisely in the next chapter– of the North Atlantic Ocean along 53°N during the transition from winter to early spring. The focus is on the analysis of a data set (CTD, microstructure, ADCP and meteorological data; more on this later) collected in the aforementioned region. However, instead of starting this introductory chapter with the pertinent background information, it is considered appropriate to make first of all some general comments about turbulence and the underlying philosophy in the analysis of turbulent flows. Independently of these comments, concepts and terms related to turbulence will be discussed as they appear in the text. The next section is about the general importance of turbulence for the ocean mixing processes and presents a review of some work relevant to the main objective of this investigation which is presented in the final section.

1.1 Turbulence

The opening paragraph in the preface to the book by Lesiure (1987) points out that: *turbulence is a dangerous topic which is often at the origin of serious fights in the scientific meetings devoted to it since it represent extremely different points of view, all of which have in common their complexity, as well as an inability to solve the problem. It is even difficult to agree on what exactly is the problem to be solved.* It is not easy to properly define turbulence and most of the authors opt for a list (generally of different length and with different items) of properties to be satisfied by a flow in order to be considered as turbulent. See for example the books by Tennekes and Lumley (1972), Kundu (1990), Tritton (1988) and Frisch (1995). Classically, turbulence is defined by Osborn (1986) as "the random, fluctuating, three–dimensional

motion that is both dissipative and diffusive"; Monin and Ozmidov (1985) define it as "an ensemble of random fluctuations of thermodynamic characteristics in rotational flows", and for Tritton *op. cit.*, turbulence is "a state of perpetual instability". In general, turbulent flows have the following characteristics: they have high values of Reynolds number (defined as $R_e = \frac{UL}{\nu}$, where U and L are characteristic scales of velocity and length in the flow, and ν is kinematic fluid viscosity); their dynamic and thermodynamic characteristics change rapidly and unpredictably in both time and space; they are highly diffusive, dissipative and rotational, and fluctuations of vorticity on large spatial scales generate –by nonlinear interactions– a fluctuating cascade, in which successively smaller vortices are generated down to a limit where kinetic energy reaches length scales small enough for the molecular diffusion to be able to act to dissipate it to heat.

Notwithstanding the intense effort devoted over centuries to the understanding of turbulence, progress toward the development of a satisfactory mathematical theory is limited. The principal difficulty is not a lack of comprehension of the equations of motion for the individual particles comprising the fluid; indeed, for most applications the particles may be treated classically and their trajectories described by Newton's laws of motion expressed in the Navier–Stokes equations. However, it is an impossible task to solve these equations simultaneously for all of the particles in a macroscopic fluid. This way, we have to be content with a simpler description of the evolution of a fluid, much less detailed than at the level of particle trajectories, by averaging the Navier–Stokes equations over all particles in a fluid element. (The average of Navier–Stokes and other pertinent equations are normally calculated following a procedure introduced by Reynolds (1895), as is discussed widely elsewhere and only superficially mentioned in Chap. 2). However, the averaging of the Navier–Stokes equation, due manly to its nonlinear character, introduces a new difficulty, known as the closure problem: the equation for the statistical moments at each order involves higher–order moments. Even in this conceptual framework, largely statistical, turbulent flows are unpredictable, in the sense that a small uncertainty in the knowledge of their initial position at a given initial time will be amplified, making precise deterministic prediction of their evolution impossible.

Although the averaged Navier–Stokes equations properly describe, in principle,

the behavior of turbulent flows, many difficulties are still present. The solution requires so many Fourier harmonics that the problem becomes intractable, both analytically and numerically, and to date much of our quantitative knowledge of turbulence is empirical. Besides, the experimental database is limited because it is very difficult to make measurements of turbulence–related variables even in controlled laboratory systems, not to mention in natural turbulent systems like in rivers, lakes, the atmosphere and the ocean. Additionally, it is very hard to set experimental arrays allowing repetition of the experiments with the same initial conditions, which in nature is an impossible goal. Significant developments in the computer sciences and the advances in numerical schemes allow us to improve the resolution of numerical simulation of turbulent systems; however today's supercomputer resources, and those foreseeable in the near future, are not sufficient to resolve all of the scales involved in fully developed turbulence (Burchard, 2002).

In principle, on an ideal computer capable of solving the Navier–Stokes equation down to the dissipative scales, the problem of modeling turbulent flows is reduced to an *ad hoc* implementation of boundary and initial conditions. In real computers however, turbulence modelers (and also observationists trying to fit data to theories) face another paramount problem: that of including small–scale effects in their calculations and/or balances. Researchers' recognition of the importance of small–scale processes, particularly near boundaries, is reflected by an intense search for "small–scale processes parameterization", *i.e.* representing them by formulae in terms of the model's large–scale variables rather than just as numbers whose validity could be limited to particular conditions (Müller and Garrett, 2004). Large–scale numerical modelers, for example, try to include the more appropriate parameterization of turbulent processes –which are not solved properly by their models– to avoid spurious diffusion and artificial diapycnal mixing, among other problems. In the case of geophysical fluids circulation modeling, this problem is notoriously aggravated near boundaries, especially at abrupt topographic features, when isopycnal slopes are large or if any dominant process become thinner than grid spacing. All of these processes taking place at scales smaller than that of the model are collectively known as *subgrid processes* in the jargon of modelers. Proper representation of subgrid processes is a major issue for numerical fluid modelers, and any improvement on this subject

depends heavily on the proper parameterization of turbulent processes.

Mainly two characteristics of turbulent flows make them extremely difficult to study. First, turbulent flows span a wide range of scales and spatial patterns. And second, the nonlinear character of their dynamics forces each spatial scale to interact with many more and no pattern evolves independently from any others.

In short, when studying turbulent flows it should be kept in mind that there is not any guarantee of a solution to exist for the Navier–Stokes equations –even in their averaged form– and, for now, it does not make any sense to ask for the instantaneous velocity of each particle and we must work on trying to obtain approximations of low–order moments, such as the average or mean square of the fluid velocity over all possible realizations. Additionally, it is important to be aware of the obtainable precision when setting the initial conditions of an experiment because turbulent systems are extremely sensitive to initial conditions making it virtually impossible to repeat individual realizations. Numerical simulations must be carried out with a careful consideration given to the limit of model–solvable scales and those that need to be parameterized. Care must also be exercised concerning the underlying theories about the nature of turbulence when analyzing numerically or experimentally obtained data. See for example the work of Smyth and Moum (2000).

1.2   Ocean Turbulence Mixing

Turbulence and the mixing it produces rule many of the fundamental physical processes taking place in the atmosphere–ocean system, notably those controlling the exchange of properties like momentum, heat and mass through the interface separating the two media, and those steering distribution and variability of physical and chemical properties; this makes turbulent mixing play a central role in climate variability and, consequently, in life. It is not an exaggeration to say that our world and the life it sustains would be totally different without turbulent mixing. The very basic functioning of the atmosphere–ocean system seems to be, at first glance, extremely simple. There is an interchange of energy and mass through the interface mediated mainly by turbulent fluxes. Then, up from the interface into the atmosphere and down to the interior of the ocean it is established a permanent competition is basically established between two kinds of mechanisms: those trying to

increase stratification and those trying to break it. As a consequence of this competition, identifiable boundary layers are formed at both sides of the interface. However, behind this apparent simplicity is hidden a tremendous complexity. Except for a few oversimplified cases, the turbulent nature of the dominant flows makes deterministic analyses impossible, laboratory simulations and *in situ* observations are generally unsatisfying and very difficult to obtain, and numerical simulations limited by both computing capacity and phenomena comprehension.

The prominence of the role played by turbulence in many critical ocean processes cannot be overemphasized. Turbulent water motions affect every aspect of oceanography, as pointed out by Nihoul (1980): "The action of turbulence appears not only in the circulation models of physical oceanographers but equally in the model of chemical distributions, of biological production and of sedimentation"; and by Kraus and Businger (1994): "Exchange of mass, momentum, heat and other water properties through the atmosphere–ocean interface are mediated by turbulence".

A clear example of the complexity and nonlinearity of the interactions between large–scale ocean circulation and ocean turbulence can be found in the underlying mechanisms forcing the Meridional Overturning Circulation (MOC) of the world's oceans –not to be confused with Thermohaline Circulation (THC) which is only a part of MOC– which is considered to be responsible for around half of the ocean's ability to transport heat from the tropics toward the poles. Due to strong cooling events at high latitudes, ocean water becomes denser and in a few locations (*e.g.* the Labrador Sea and the Weddell Sea) it sinks and spreads throughout the ocean, forming deep and intermediate water masses. To satisfy mass conservation, this sinking water must return to the shallow ocean, and actual vertical temperature and salinity (*i.e.* density) distributions show this requires a downward movement of heat and fresh water, presumably ruled by fine– and micro–scale eddies that cannot be suppressed by the stable stratification. Munk (1966) estimated that this balance requires an eddy transport characterized by a diapycnal (across density surfaces) diffusivity of about 1 cm^2s^{-1}. Indeed, general circulation models show that the rate of overturning, and hence poleward heat transport that affects global climate, is largely determined by the diapycnal diffusivity used. For example, the concept of

conveyor belt, introduced by Broecker (1987), depends on the existence of extensive and intensive mixing regions. Variations in position, extension or intensity of such mixing regions may have profound consequences for climate (Rahmstorf, 2003). In a recent work by Mohammad and Nilsson (2004), a numerical model is used to explore the role of diapycnal mixing in the equilibrium response of THC. Their results show that the qualitative behavior depends crucially on the nature of the small–scale vertical mixing in the interior of the ocean and they conclude that, for their numerical model, the nature of the vertical mixing proved to be crucial for the response of the circulation to changes in the surface fluxes of heat and freshwater. The discussion about how THC may be modified as a consequence of variations in vertical mixing is an open one, and although numerical and theoretical results are sometimes divergent and even contradictory, all of them coincide in pointing out the fundamental importance of improving the parameterization of small–scale processes. See also the work of Maraotzke (1997).

The relationship between overturning circulation and micro–scale eddy diffusion, the mechanisms ruling upper ocean dynamics and bottom energy dissipation are examples of the connection between large and small scales. Nonlinear interaction among so many components in the ocean is so complex that it is simply not possible to obtain reliable estimations of the rate of diapycnal eddy diffusion, or of any other important turbulent process, without direct observations of the turbulence itself. During the last three decades, direct observations of eddy motion on the micro–scale range and direct measurements of the vertical spread of tracers allowed more to be learned about the ocean's eddy activity (see Gargett, 1989). Results show that diffusivity is in most places an order of magnitude weaker than required by Munk's balance. Either the conceptual picture of MOC is very wrong or mixing is much more vigorous at certain times and places –*e.g.* transitional periods and boundaries not fully examined– than in the already measured places. An inescapable conclusion is that direct observations are needed.

A better understanding of ocean turbulence and its role in ocean mixing, and how ocean mixing can be accurately parameterized, is essential for developing new ocean circulation models for studies ranging from local ecosystem dynamics to coupled atmosphere–ocean climate (Müller and Garrett, *op. cit.*).

1.2.1 Previous Works

Hopeless as it may seem, the study of turbulence and associated mixing have a long tradition and many successful applications in the study of almost all of the fields of knowledge. For a review, see the work of Hunt *et al.* (2001) and those of Lorke (1998) and Roget *et al.*(2004). In the study of natural water systems dynamics the approach follows mainly two complementary pathways, both linked in great measure to technological advances: measurement of microstructure field of variables like temperature, salinity through conductivity, velocity, and velocity gradients; and computer simulations of relevant dynamical processes. Output data analyses (from both numerical or observational experiments) are carried out within the context of turbulence theory based on the assumption of stationarity, homogeneity and isotropy as postulated by Kolmogorov (see Smyth and Moum, 2000). In nature, turbulence never conforms to this oversimplification, particularly geophysical flows whose physics is greatly complicated by the influence of ambient shear, density stratification, and the presence of boundaries inducing anisotropy. Many advances, however, have been made in the study of turbulence in the ocean; for an excellent, though a bit dated, review see the work of Caldwell and Moum (1995). A more recent compilation may be found in the monography of Kantha and Clayson (2000b). For a review of the influence of turbulence on phyto– and zooplankton see the works of Gargett and Marra (2002) and Yamasaki *et al.*(2002), and for a review on numerical modeling of ocean turbulence see Burchard (2002).

Starting point reviews of turbulence and related topics in the ocean include: ocean mixing (Gregg, 1987, Gargett, 1989, Garrett, 1993); air–sea interactions (Donelan, 1990, Wyngaard, 1992); mixing in stratified fluids (Fernando, 1991); history of microstructure observations (Gregg, 1991); arctic processes (McPhee, 1990); salt fingering (Schmitt, 1994); and applications of the Kolmogoroff spectrum to the ocean (Phillips, 1991).

Understanding the mixing processes in the Upper Ocean Boundary Layer (UOBL) passes through turbulence and the messiness associated with it and the interaction of the many different mechanisms that can trigger or diffuse it (Caldwell and Moum, 1995). Ocean turbulence involves the nonlinear interaction of a wide range of spatial and temporal scales of motion associated with many different forc-

ing mechanisms like surface wind–stress, frictional drag against solid boundaries, or dynamical instabilities produced by internal waves or buoyancy fluxes in a stratified fluid. The absolute and relative strength of these forcing mechanisms and the strength of resultant turbulence shapes boundary layers at the surface and at the bottom of the ocean. All of this interplay of spatial and temporal scales imposes its signature on the structure of the UOBL, whose temporal variability scales range from minutes to years, while spatial variability may range in horizontally from meters to the basin size and vertically from centimeters to hundreds of meters.

The study of turbulence and associated mixing in the upper ocean layers is important for all sorts of problems in oceanography, research activity is so intense and the literature is so abundant that it is not easy to track the evolution of one single subject from the many mentioned in previous paragraphs. Quantification, and even identification, of processes involved in the dynamical balance shaping the upper ocean layer remain to a great degree incomplete due mainly to the difficulties inherent in obtaining good quality observational data of the many processes taking place at the upper ocean layer. Among them, mixing is considered to be particularly important, but also particularly elusive: it takes place over entire ocean basins and is highly anisotropic, it is difficult to observe and to measure, and physics of their associated processes like turbulent diffusion, shear and convective instabilities, wave breaking and overturning are not completely understood.

Direct measurements of small–scale shear, temperature and conductivity microstructure in the UOBL allows the variability range of the kinetic energy dissipation rate (ϵ) and turbulent diffusivity (K_b) as a function of atmospheric forcing and regional background dynamics and stratification to be determined. The importance of these two parameters has been discussed on the basis of microstructure measurements in UOBL by Dillon *et al.* (1981), Shay and Gregg (1984), Imberger (1985), Lombardo and Gregg (1989), Moum *et al.* (1989), Anis and Moum (1995), Terray *et al.* (1996), Soloviev *et al.* (2001), and Lass *et al.* (2003) to name just a few select publications. In those works the influence of surface fluxes on averaged vertical profiles of ϵ in the upper ocean is analyzed, and various scaling procedures are implemented and tested. Note that most of data that have already been used for analysis of oceanic microstructure in UOBL were collected in equatorial, tropical

and subtropical regions (*e.g.*, PATCHEX and TOGA–COARE experiments). Setting aside turbulent measurements taken in the Arctic Ocean under the ice [Padman and Dillon, 1991; McPhee and Stanton, 1996] and in Antarctic waters [McPhee *et al.*, 1996], only a few studies can be mentioned [Simpson *et al.*, 1996; Lozovatsky *et al.*, 1999; Inall *et al.*, 2000; Burchard *et al.*, 2002, Bolding *et al.*, 2002; Lass *et al.*, 2003] where the dependence of ϵ on atmospheric forcing at relatively high latitudes was addressed. All of these observations, however, were made in shallow coastal zones (the Black Sea and the Malin Shelf) or in shallow seas (the North Sea and the Baltic Sea). In a comprehensive review of the geography of ocean mixing, Gregg (1999) shows a map with the sites of microstructure measurements, which indicates that no such measurements have been carried out in the open ocean poleward from $40\,°$N. The situation has not changed since then.

Seasonal variations in atmospheric forcing are most distinct in mid–latitudes (between $40\,°$N and $60\,°$N in the Northern Hemisphere). During the warm season (late spring – early autumn) atmospheric heat flux enters the ocean through the sea surface, but in winter and early spring large areas of the North Atlantic Current are influenced by persistent negative (upward) heat flux. This convection–favorable buoyancy exchange between the ocean and atmosphere, in combination with pre-dominant high winds, generates and maintains turbulence in UOBL. Microstructure measurements in the UOBL at a zonal, cross–ocean, upper–mid–latitude transect can give valuable information on the basin scale variability of mixing intensity for a specific season. Such measurements (to be presented in Chapters 3 and 4; especially those in the upper 200–meter oceanic layer) have been conducted during the 9th cruise of the R/V Akademik Ioffe in April 2001, using Neil Brown Mark III and MSS [Prandke and Stips 1998; Prandke *et al.* 2000] microstructure profilers.

1.3   Objectives

Turbulent motions in a stratified fluid intermingle fluid parcels from different parts of the flow, thereby enhancing mixing across concentration gradients through molecular diffusion. Knowing the rate of ocean mixing is of capital importance for many reasons, including an ocean model's ability to predict global circulation, climate change, pollutant dispersal and primary productivity relies on a proper quantification

of the subgrid–scale effects of turbulence. In previous sections it was established that the study of turbulence and ocean mixing is a complex problem, that their importance in most of the ocean processes is crucial and that field observations are fundamental for both comprehension of the turbulence *per se* and a better understanding of the mechanisms controlling those processes. Questions about ocean turbulence are many and tools are reduced: an unfinished theory, computers not powerful enough for numerical modeling and scarce data sets. As pointed out in first paragraph of this chapter, this work is about analyzing a data set including microstructure data collected simultaneously with hydrographic and meteorological observations in a key –from many points of view– oceanic region. Though circulation, hydrographic and meteorological conditions of the zone have been studied for a long time and much is known about them, this is –to the best of knowledge– the first time that observations of microstructure have been taken, and especially in conjunction with ADCP, CTD and meteorological observations; this information offers a rare opportunity to analyze and describe the upper ocean structure in light of the prevailing velocity field, hydrographic conditions, atmospheric forcing and microstructure information, *i.e.* this is the main objective of this work. Analysis is not process–oriented, focusing instead on bulk properties of mixing induced by atmospheric forcing during the winter–spring transition season, characterized by predominantly stormy winds and a downward (positive) surface buoyancy flux.

This work is structured as follows. After this introductory chapter, a general description of the ocean variability scales, the structure of the ocean water column and the major processes controlling upper ocean dynamics are presented in Chapter 2, followed by a presentation of the energy equation and the most basic elements of turbulence theory. Chapter 3 presents a microstructure data set and the methodology followed to process the data, from cleaning and filtering, down to the obtention of the kinetic energy dissipation rate (KEDR). The field campaign is described in Chapter 4, where the obtained hydrographic and meteorological data are described and the methodology used for the calculation of atmosphere–ocean bulk fluxes is presented. In addition, an analysis of the observed upper layer velocity field is made. In Chapter 5 the depth of the upper quasi homogeneous layer (h_D) –a layer inside the UOBL to be presented in 2.2.1– and that of the isothermal layer depth are calculated and

their correlation is explored. A comparison of (h_D) as obtained from CTD data and microstructure profiles is also made, and later their transect structure is analyzed. Finally, three scalings of (h_D) are presented: the Monin–Obukhov length–scale, the Ekman length–scale and the Ekman stratified length–scale. In Chapter 6 the vertical structure of KEDR is presented and its dependency on buoyancy and momentum fluxes and obtained parameterization are presented. After this, the concept of mixing layer depth h_ϵ –explained at 2.2.1– is compared with h_D. Then, some basic statistics of mixing parameters are presented followed by the exposition of an obtained mixing scheme based on the Richardson's number. Finally an estimation of the column integrated dissipation rate, compared to the work exerted at the ocean surface by the wind, is presented. A summary and conclusions are presented in Chapter 7.

CHAPTER 2

Background

The purpose of this chapter is to establish the minimal set of concepts, terms and assumptions constituting the framework for the presentation and discussion of this work. The first section provides a brief explanation of the spatio–temporal scales of water motion in the ocean. Then there is a section where it is presented a review of the upper ocean structure and major processes controlling their dynamics is presented to introduce the nomenclature to be used in this work, mainly because there are not any unified criteria in the field and sometimes different names are used for the same purpose. In the final section a statement of the basic governing equations –without details about their derivation– with emphasis on the energetic budget is presented, and followed by a presentation of the very fundamentals of Kolmogorov turbulence theory and the definitions of some of their scales and adimensional parameters.

2.1   Ocean Variability Scales

The ocean is a very inhomogeneous medium whose dominant feature is its variability. That variability occurs over a wide range of temporal and spatial scales and its is manifested in their properties like temperature, salinity, density, velocity and distribution of chemicals and biological species. This inhomogeneity follows a dynamical equilibrium ruled by the complex interplay of two kinds of agents acting in opposite directions: those tending to accentuate the gradients in the distribution of ocean properties, and those acting to smooth such gradients. Among the first group are the temporal and spatial variability of received and emitted radiation, evaporation and precipitation, freezing and melting. The second group includes ocean circulation, planetary tidal forcing and their interaction with bottom topography and

basin morphology, internal and surface breaking waves, wind forcing and in general all those processes associated with the production and enhancement of stirring and mixing.

Ocean variability occurs on all sorts of time and space scales: from seconds to millenniums, and from millimeters to a global scale, going from the ephemeral capillary waves, whose influence is limited to the very first millimeters of the ocean surface, to cooling events that can mix the ocean down to thousands of meters, or El Niño and North Atlantic Oscillation events whose influence may affect the entire globe. Some of those variations are periodical and obviously linked to clearly identifiable forcing agents of known frequencies, *e.g.* tidally forced movements, inertial motions, daily or yearly heat cycles. Some other signals are far from periodical and their signature is many times obscured by their interaction with others, or they are so weak that it is not an easy matter to elucidate their generation, or the degree of their influence on atmosphere–ocean dynamics. Finally, some perturbations take place at the limits of our observational capacity: they have such long periods that the length of our registers do not allow us to characterize them properly. Or, on the other hand their length and time scale are so short that it is not possible to resolve them except in a statistical sense. Denman (1994) considers that motions in the ocean may be grouped into four space–time ranges:

- **Rotational Range**: This range encompasses the largest length and time scales; motions occur primarily in the horizontal (are two–dimensional), length scales are greater than 100 meters and time scales greater than one inertial day. This includes ocean basin circulations such as gyres, rings and eddies that are influenced by the effects of the Earth's rotation (the Coriolis force).

- **Buoyancy Range:** In this range, length scale approaches the depth of the upper ocean mixed layer (from one meter to hundreds of meters, but bigger on exceptional occasions) and includes internal waves and small–scale eddies. Fluid motion makes a transition from two–dimensional to three–dimensional flow, with periods on the order of minutes to many hours. Buoyancy Range motions are strongly ruled by gravity and stratification of the water column.

- **Inertial range:** In this range gravity and molecular viscosity are dominated

by inertial forces. Motions are turbulent, three–dimensional and occur mainly on a small–scale (several meters to several centimeters) and over periods ranging from several seconds to several minutes.

• **Viscous Range:** This range is dominated by fluid motions taking place in the smallest possible scale: from molecular to less than a few centimeters. Motions are dissipated by molecular viscosity, and kinetic energy of the viscous–scale flow appears in the fluid as heat.
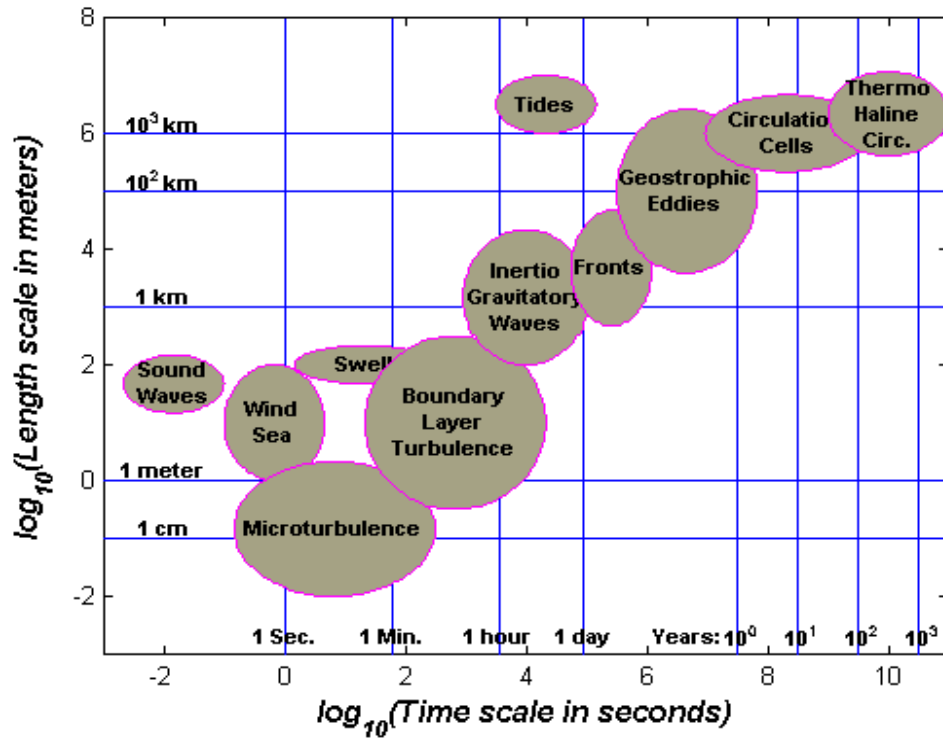
Figure 1. Temporal and spatial scales of typical processes taking place at the ocean. Modified from von Storch and Zwiers (1999).

Making a clear–cut separation of space–temporal ranges is not possible. Denman's classification, despite the flexibility of its proposed limits, excludes important scales of variability (*e.g.* tides, wind sea and sound waves). In Fig. 1, modified from von Storch and Zwiers (1999), the most relevant range of scales in the ocean are represented by ellipses centered on what is considered to be their most characteristic

values in space and time: their axes indicating variability limits. Note that the scale in the horizontal axis of the figure is linear in the logarithm of time in seconds, while that of the vertical axis is linear in the logarithm of length in meters. Some vertical lines are inserted to indicate the location of time units of common use; similarly, horizontal lines are included to point out at the position of some selected lengths.

This work mainly concerns analyzing processes taking place in the upper ocean layer, where complex interactions of motions belonging to the four aforementioned ranges of ocean variability take place. In Section 1.2 it was established that the link between large and small–scales is turbulence–enhanced mixing. In the words of Pickard and Emery (1990), "Small scale turbulence is essential to energy and mass transport vertically in the water column. In the ocean the vertical flux of properties such as horizontal water velocity, heat, salinity, and nutrients are primarily dependent upon turbulence".

2.2 Upper Ocean Boundary Layer

The portion of the ocean known as the Upper Ocean Layer (UOL) or Upper Ocean Boundary Layer (UOBL) is defined as that part directly influenced by surface forcings such as heat flux, wind stress, and surface waves (Anis and Moum, 1995). The occurrence of all of these processes confers great importance to the very first meters of the ocean column from many points of view (physical, geological, chemical and biological) and motivates great scientific interest. Müller and Garret (2004) consider that, in a some way the ocean may be thought of as a physical system whose behavior is ruled by what happens in their three boundary layers: the already mentioned UOBL, the Bottom Ocean Boundary Layer (BOBL) and the Lateral Ocean Boundary Layer (LOBL). This assertion is founded in the fact that with the exception of tidal forces, geothermal plumes rising into the ocean and intense vertical convection taking place in a few places, the rest of the forcing agents like wind, surface buoyancy fluxes associated with heating, cooling, evaporation, precipitation, bottom friction and ice formation act and communicate their influence through boundary layers that are thin compared to ocean depth. Thorpe (1999) considers the existence of a fourth type of boundary layer, that formed at the surface of an ocean partially or completely covered with ice (ICBL). Its structure –being isolated from atmospheric

forcing– depends greatly on the nature of the ice cover and whether it is accumulating or melting, as well as being strongly influenced by tidal forcing. In spite of their importance for ocean dynamics and that of the processes taking place there, the BOBL, LOBL, and ICBL are not given any further consideration in this work. However, it worth mentioning reported evidences about the influence of internal waves –reflected or generated in he BOBL and LOBL– affecting the structure of the UOBL. Interested readers may consult the works of Garret *et al.* (1993), Marotzke (1997), Ledwell *et al.* (2000), St. Laurent *et al.* (2001) and McPhee–Shaw and Kunze (2002).

UOBL is also a key component in the studies of climate, biological productivity and marine pollution. It is the link between the atmosphere and the deep ocean and directly affects the air-sea exchange of heat, momentum and gases. Moreover, turbulent flows in the mixed layer affect biological productivity by controlling both the supply of nutrients to the upper sunlit layer and the light exposure of phytoplankton. Interaction between the atmosphere and the ocean takes place through their interface and it is mediated by the many processes taking place at their boundary layer. Depending on dominant process, this interaction confers to the water column a characteristically vertical distribution of their properties for each place and time. The next section is devoted to providing a brief description of what is generally considered to be the average structure of a sea water column down to the thermocline.

2.2.1 UOBL Structure

Generally, the UOBL includes both an upper mixed layer –which is directly or indirectly subject to the influence of the atmosphere– and a highly stratified zone below it, where vertical gradients of most of the ocean's properties are maximum and whose response to atmospheric forcing is slower and thus the deep ocean is isolated from it. Some other layers, however, are identifiable. From surface to depth, the typical structure of the upper ocean layer consists of a sequence of layers illustrated by the diagram shown in Fig. 2, whose scales are only indicative. In Fig. 2a the typical structure of vertical gradient of horizontal velocity is shown (units are s^{-1} but scale is arbitrary); the typical vertical temperature profile is represented, also using an arbitrary scale in °C, in Fig. 2b; and Fig. 2c presents an exploded view of

the first layer using a logarithmic vertical scale. The width, and even the existence, of each layer depends on the kind of processes, and their relative importance, taking place during measurement time. In the first layer, known as the Ocean Surface Layer (OSL), the vertical velocity gradient usually has a relatively high and constant value and temperature typically increases linearly from its value at the surface by around one centigrade (see Fig. 2b). Although such a gradient, as shown in panel (c) of the same figure, is far from being linear in the first millimeters of the ocean surface, that tiny layer is called the Cool Skin Layer (CSL). Due to data limitation, neither OSL and CSL are being considered in this work and interest is centered in the next layer, which is known as either the Upper Ocean Mixed Layer (UOML) or the Upper Quasi–Homogeneous Layer (UQHL) the name preferred in this work, which is characterized by low and constant values of the vertical velocity gradient (Fig. 2a) and almost constant values of temperature (Fig. 2b). It is important to point out here that the lower depth limits of constant values of temperature and those of velocity do not necessarily coincide. The last layer, known as the Seasonal Thermocline (ST), is characterized by a maximum vertical gradient of temperature and a narrow local maximum in the vertical velocity gradient.

Later in this work, the depth of the UQHL (hereafter denoted by h_D) will be differentiated from the depth of the *mixing layer depth* (h_ϵ) defined as the depth where turbulence is found to be active and usually considered as that where ϵ rapidly decreases from about 10^{-7} Wkg^{-1} to $\sim 10^{-8}$ Wkg^{-1}. As will be discussed h_ϵ can be smaller, larger or equal to h_D.

Seasonal averages –over 8 years– of vertical temperature distribution at four points in the Atlantic Ocean were chosen to illustrate the UQHL vertical structure and its spatio–temporal variability, shown in Fig. 3. Data, obtained from Levitus Data Bank[1] correspond to a four very different oceanographic regions, and each group of profiles is representative of mean conditions inside a square of ~ 100 km per side centered at the position indicated in each panel. Profiles shown in Fig. 3a correspond to a tropical area close to the equator, a region where the depth of the UOBL is limited to ~ 200 m and the annual heat cycle is more evident at the level

---

[1]http://dss.ucar.edu/datasets/ds285.0/
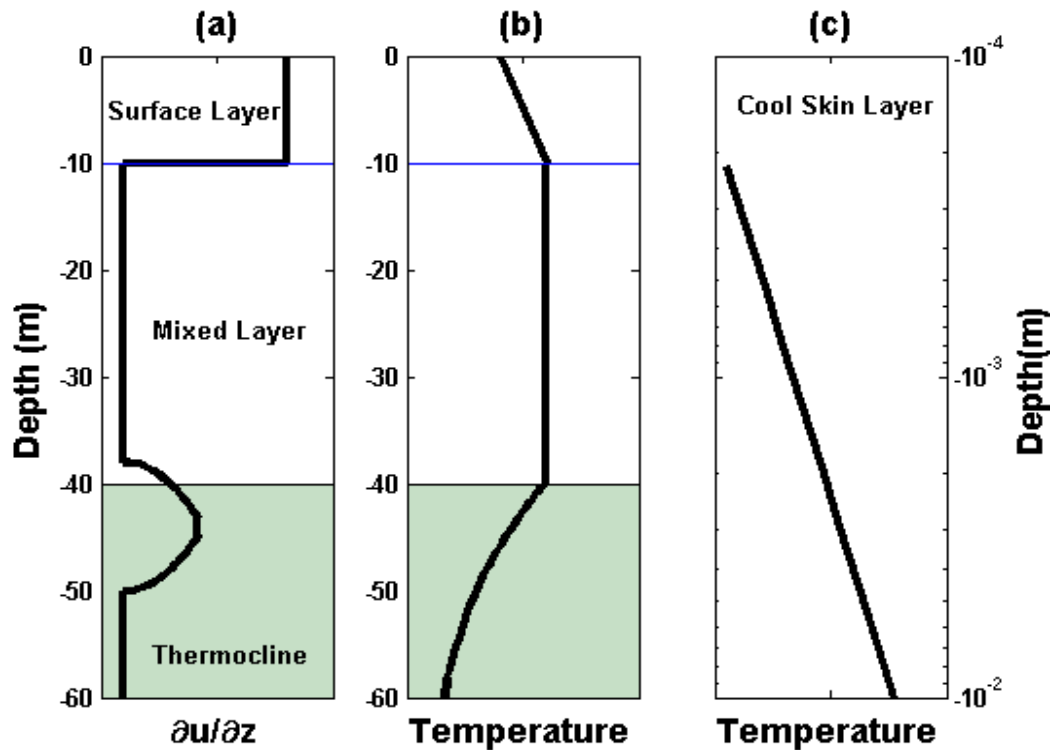
Figure 2. Typical vertical distribution of (a) vertical gradient of horizontal velocity; (b) temperature, and (c) temperature in the first ten meters, with emphasis on the first centimeters.

of the thermocline than at the UQHL whose depth is close to ∼50 m. In Fig. 3b the profiles closely correspond to a transitional zone between tropical and temperate regions. The seasonal cycle is evident in the first hundred meters of the water column, the mixed layer depth varies between ∼30 m and ∼100 m while the seasonal thermocline varies moves accordingly, and temperature changes are more evident close to the surface. In part (c) of the figure, profiles correspond to a region close to the upper limit of a temperate zone, UOBL variation can be observed down to ∼400 m, and the sea surface temperature variation is wider. While profiles in panels (a), (b) and (c) are from data at different latitudes but at the same longitude (40 °W), profiles shown in Fig. 3c are from the same latitude (50 °N) as those in panel (d) but different longitudes. They are located ten degrees to the west (∼700 km) and are closer to the coast. In this case the variability in UOBL is even wider but vertically
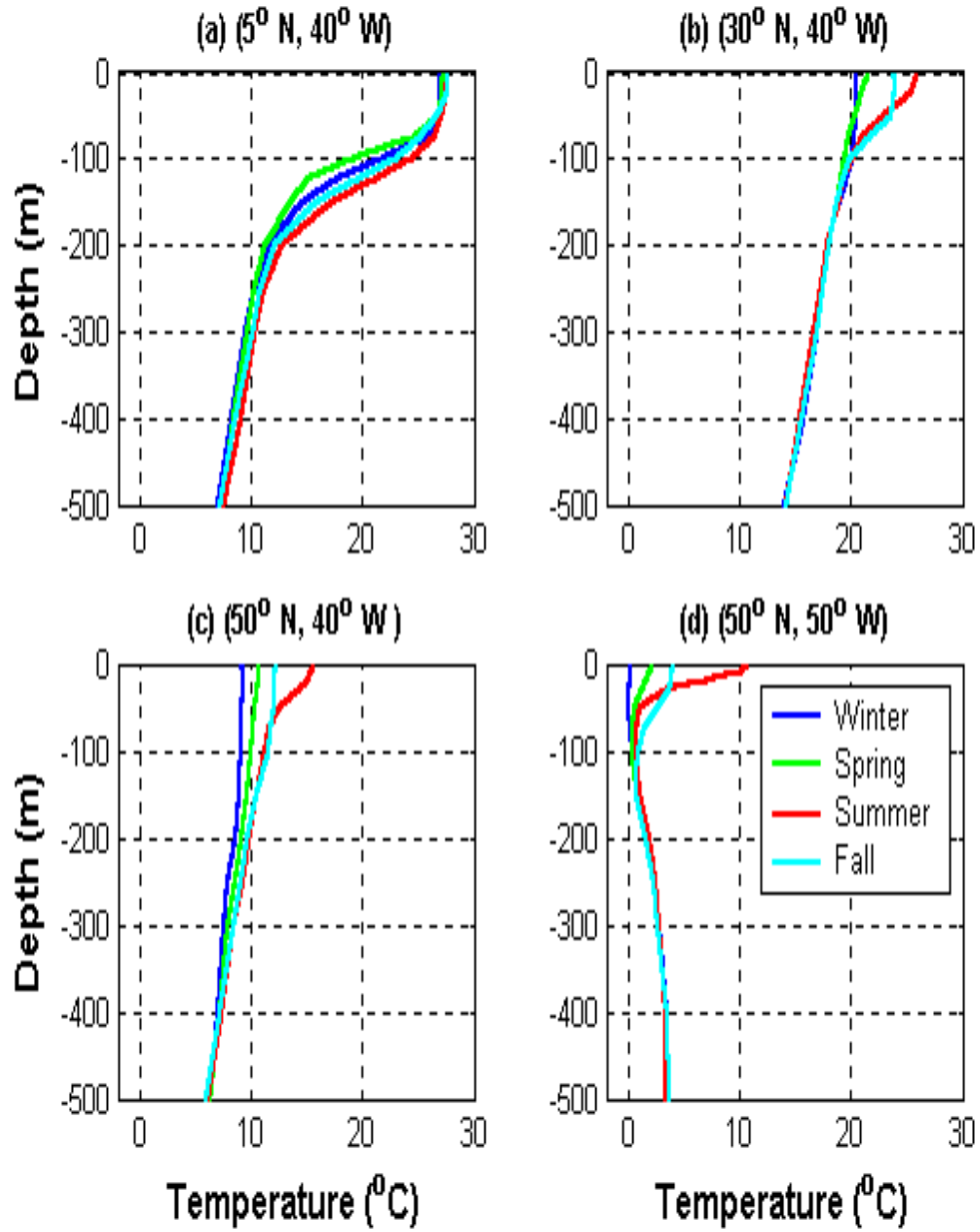
Figure 3. Yearly cycle, averaged over eight years, of vertical distribution of temperature averaged over a square of ∼100 km per side, centered at the position indicated over each panel.

restricted to the first one hundred meters. The scale at which profiles were plotted does not allow the OSL to be appreciate in any profile because its depth rarely exceeds ten meters. Data analyzed in present work were collected in a region close to $50\,°$N during the transitional time from winter to spring.

The variability of the UOBL depends on many factors. In Fig. 4 (taken from the Internet[2]) an illustrated view of the most important processes associated with each of its layers is presented. And the following paragraphs provide a brief description of each layer and its most conspicuous associated physical processes.

Cool Skin Layer (CSL)

In Fig. 2(c), a drawing representing the first ten meters of the vertical profile of temperature is plotted using a logarithmic scale for the depth axis to put the emphasis on the very top layer called the sea surface microlayer or the Cool Skin Layer (CSL). Temperature in this tiny region is known as skin temperature, while that registered in the layer directly underneath (OSL) is known as bulk or turbulent temperature or Sea Surface Temperature (SST). Any difference between these two temperatures (usually in the range of tenths of K) is known as cool skin effect, and is due to differences in the attenuation of the short–wave radiation taking place across the very first millimeters of the ocean column and/or to the net heat flux across the surface (MacIntyre, 1974). The first report on the existence of a temperature gradient just below the surface of a water body was made by Woodcock and Stommel (1947). Two basic works on the subject, by Ewing and McAlister (1960) and by Saunders (1967), used direct measurements and dimensional analysis to demonstrate the existence of a very thin laminar layer whose width, depending on atmospheric conditions, is in the order of $0.5\,$mm, and is characterized by having a lower temperature (by around 0.5 K; henceforth its name) than that of the water beneath it.

Dynamics of the cool skin layer is important *per se*, but the advent of satellite mounted instruments opened an active line of research on the subject, for two main reasons: first, the obtention of algorithms for the calculation of cool skin layer temperature as a function of radiation; and second, to properly parameterize the differences between that temperature and bulk temperature, the one that is really im-

[2]http://www.hpl.umces.edu/~lzhong/mixed_layer/sml.htm

portant for the determination of heat fluxes between atmosphere and ocean (Donlon and Robinson, 1997 and Donlon *et al.*, 2002). In Fig. 4 cool skin layer is represented by a wavy line in two tones of blue, and some of the most relevant processes that take place through it are illustrated. For a recent review of the physics of the ocean cool skin layer see the work of Kantha and Clayson (2000b).
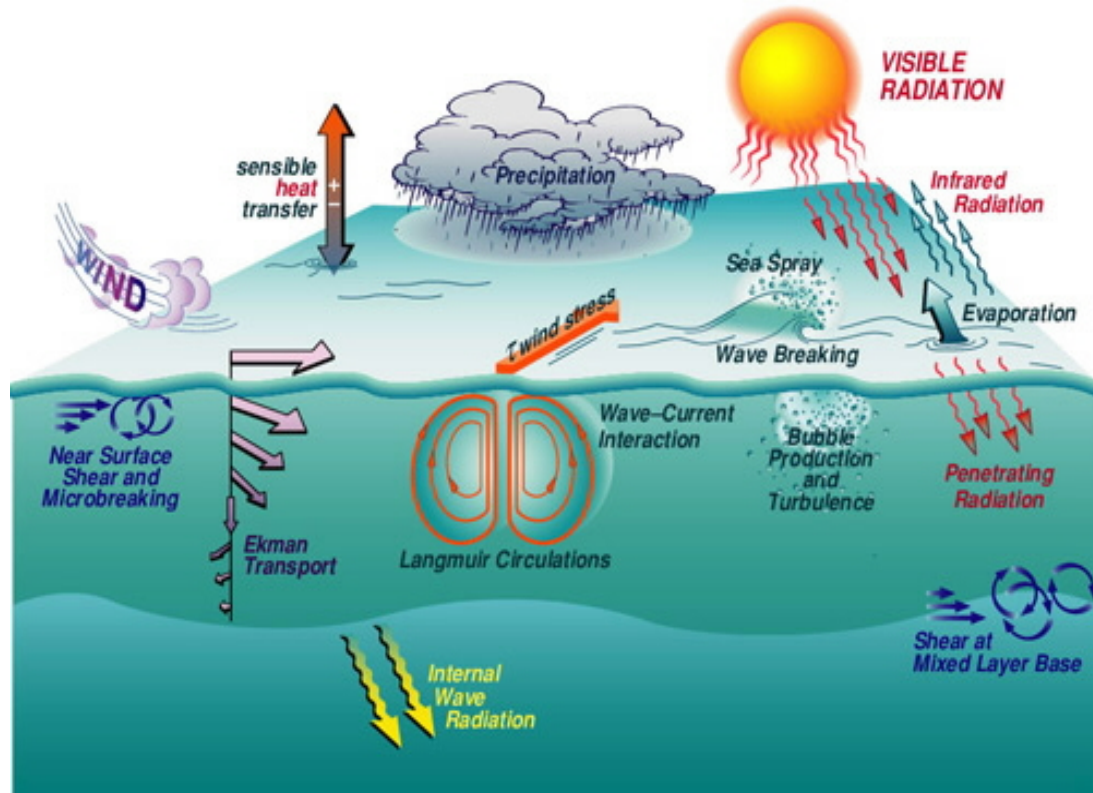
Figure 4. An illustrated view of the most important processes shaping the upper ocean boundary layer. The scale of the drawing is arbitrary. Drawing obtained from http://www.hpl.umces.edu/~lzhong/mixed_layer/sml.htm

Ocean Surface Layer (OSL)

The OSL is defined as the layer under direct influence of the forcing taking place at the surface of the ocean and its typical width is around ten meters, but depending on the atmospheric conditions, it can be wider or nonexistent. It is the zone of highest variability where the exchange of properties like heat and momentum take place. Wind forces high shear values inducing near–surface turbulence; it also

intervenes in the formation of the Ekman spiral which has a profound influence on ocean circulation, modulates the rate of evaporation, induces a circulation known as Langmuir whose influence can be extended to the upper ocean mixed layer, and takes part in the formation and breaking of waves, which in turn forces mass exchanges by injecting bubbles into the ocean or sea spray into the atmosphere. Also taking place in this layer are the absorption of most of the radiative energy coming from the sun and modifications of density due to heat fluxes, precipitation, ice formation (or melting) and runoff from rivers. The surface layer is definitely the most active layer of the ocean and the complexity of the processes occurring there is overwhelming.

Besides being the layer where major forcing takes place, the surface layer is also important because one of the most valuable parameters in physical oceanography and meteorology is defined there: the sea surface temperature or bulk temperature, defined as the temperature measured in the first meter of ocean column and denoted by T_s in this work. The importance of this variable resides first on in its wide use in ocean dynamics, in the study of upper ocean processes, and its use as a boundary condition for models, in the parameterization of air sea fluxes, and in its role as a crucial indicator for climate and its variability; second, records of SST are among the longest and most reliable to date, dating back 100 years or so in many places; and third, it is the easiest to obtain and many methods can be used to measure it: fixed or free buoys, research vessels, ships of opportunity and, during the last 20 years, from satellite mounted radiometers, among others.

Upper Quasi–homogeneous Layer

The UQHL is generally considered the mixed region in the upper ocean where there is little variation in temperature or density over depth (Kara *et al.*, 2000). This layer, called the ocean boundary layer (OBL) by Anis and Moum (1995), results from a competition among the processes acting near the interface between the atmosphere and the ocean, the turbulent energy dissipation rate, and the shear presence and radiation of internal waves at their lower limit known as the thermocline. Knowing the vertical extension of a mixed layer is very valuable information that can help to improve atmosphere–ocean modeling, and also to understand many aspects of ocean variability and productivity (Obata *et al.*, 1996). In addition, it is valuable because

its thickness determines the volume or mass over which the net surface heat flux is distributed (Chen *et al.*, 1994). However, due to its great variability, determining the ocean mixed layer depth is not an easy task and many criteria are used to do it. For a recent review and a new proposal –to be used in this work for data analysis– see the work of Kara *et al.* (*op. cit.*).

Besides the complex interaction of the many phenomena being present in the UQHL, it is there where photosynthetic organisms live because light is most abundant, and being not free swimmers their movements are controlled by the intensity of the mixing, see Gargett and Marra (2002) and Yamazaki *et al.* (2002). The solar energy flux and the heating rate are reduced to half of their value at about 1 meter (Apel, 1987) but there is still significant light and heating at 100 m (called the euphotic zone). If the mixed–layer is too deep, then phytoplankton will spend a greater proportion of their lifetime in a darker environment. Generally, the mixed–layer is nutrient rich at the end of the winter, when light levels are low. As the surface light increases, the mixed layer shoals and phytoplankton suddenly have enough light to grow and do so in a spring bloom.

Seasonal Thermocline

Below the mixed layer, there is a transitional region with a strong temperature gradient and temperature decreases rapidly with depth. This transitional layer is called the seasonal thermocline and marks the boundary between warmer surface waters and colder and deeper waters. Being the bottom of the surface mixed layer, the depth of the thermocline changes as the water column above is restratified or mixed. Consequently, and depending on the geographic zone, it is generally shallow in spring and summer, deep in autumn, and disappears in winter (see Fig. 3). In the tropics, winter cooling is not strong enough to destroy the seasonal thermocline, and a shallow feature sometimes called the tropical thermocline is maintained throughout the year. The seasonal thermocline is followed by another layer known as the permanent thermocline, where water is not influenced by surface forcing and its motion scale is in the range of millenniums.

Besides being the borderline separating waters of very different temperatures, from the point of view of mixing processes, two phenomena of capital importance

occur in the thermocline: the generation and propagation of internal waves, and the formation of intense velocity gradients; see, for example, the works of Moum (1996) and Gregg *et al.* (1996).

2.3 Governing equations

The most basic equations for the analysis of Newtonian fluid dynamics are those of Navier–Stokes (Navier, 1822 and Stokes, 1845) expressing the balance of momentum, the equation for mass conservation –known as the continuity equation– and pertinent equations for fluids following conservative scalars along with the corresponding equations of state. The whole set of equations is prototypical of a nonlinear problem and is rarely used in its full expression. So, as discussed in Section 1.1, instead of this, simplified versions tailored for a specific problem are used. Presentation and derivation of the basic equations are omitted here; a step by step derivation can be found in most of the standard textbooks on geophysical fluid dynamics and/or turbulence dynamics, those of Batchelor (1967), Gill (1982), Kundu (1990) and Tritton (1989) being among the most highly recommended. The next paragraphs present the equation expressing the Turbulent Kinetic Energy (TKE) balance, of central importance in this work, and some other pertinent relations. The presentation is done without a thorough derivation –interested readers are referred to previously mentioned books and to one by Burchard (2002)– and emphasis is put on the meaning of each term in that equation. Equations are presented in a mixture of tensorial and vectorial notation, an almost standard costume in fluid mechanics and specially in physical oceanography. Symbols and concepts are explained as they appear for the first time in the text, and, though redundant, if necessary, they will sometimes be reintroduced, hopefully to the benefit of clarity.

2.3.1 Turbulent Kinetic Energy Equation

The standard approach to handling turbulence dynamics is to take the so–called *Reynolds average* of the Navier–Stokes equations and of those for scalars, mass conservation and state equations; although no detailed discussion of this procedure is given, it worth mentioning that it is based on the introduction of a decomposition (the so–called *Reynolds decomposition*) of the instantaneous (dynamic and thermo-

dynamic) variables into two components: the mean and the random fluctuations around the mean, which are assumed to satisfy very specific statistics (see Tennekes and Lumley, 1972 and Kundu, 1992). This approach introduces the concept of turbulent fluxes, and that of Reynolds stress, used to describe the transfer of momentum associated with turbulent fluctuations in the same way that the tensor of viscous stress describes the transfer of momentum due to molecular viscosity; both concepts are crucial for the current understanding of turbulence. Also, the Reynolds decomposition the equations for the mean flow and those for the variance of the fluctuations around the mean to be obtained. For the velocity field this leads to a very important equation, that of Turbulent Kinetic Energy (TKE) defined as $e = \frac{1}{2}u_i'^2$ with u_i' being velocity fluctuations around the mean value of velocity $U_i = \langle u_i \rangle$, with $i = 1, 2, 3$. Next, the TKE equation is presented without details, for a step–by–step derivation see Kundu (1992). Under the hydrostatic and Boussinesq approximations and using the decomposition and averaging procedure introduced by Reynolds, the so called Turbulent Kinetic Energy Equation is obtained after some algebraic manipulation:

$$\frac{\partial(\frac{1}{2}\overline{u_i'^2})}{\partial t} = -\frac{\partial}{\partial x_j} \underbrace{\left(\frac{1}{2}U_j\overline{u_i'^2} + \frac{1}{2}\overline{u_i'^2 u_j'} + \frac{1}{\rho_0}\overline{p'u_j'} - 2\nu\overline{u_i'e_{ij}'} \right)}_{A} \underbrace{- \overline{u_i'u_j'}\frac{\partial U_i}{\partial x_j}}_{B} + \underbrace{\frac{\overline{\rho'u_i'}}{\rho_0}g_i}_{C} - \underbrace{2\nu\overline{e_{ij}'e_{ij}'}}_{D}$$

$$(1)$$

where i and j runs from 1 to 3, t stands for time, and an orthogonal coordinate system is used where x_1, x_2 and x_3 directions are positive to the east, north and upwards, respectively, $\overrightarrow{g} = (0, 0, g)$ is the gravity vector, U_j is the mean field velocity vector, p' are pressure fluctuations, ν is known as the kinematic viscosity coefficient and is defined as the ratio $\frac{\mu}{\rho_o}$ where μ is the dynamic viscosity coefficient (a value depending on fluid and its thermodynamic state) and ρ_o and ρ' are, respectively, the mean state value of density and its fluctuations. Finally, $e_{ij}' = \frac{1}{2}(\frac{\partial u_i'}{\partial x_j} + \frac{\partial u_j'}{\partial x_i})$ is the strain rate tensor.

A short discussion about the physical meaning of each term is presented next.

- **A**. *Transport term.* This term represents the transport of turbulent kinetic energy and no production of any kind is involved in it. The first and second elements in this term account for energy transported by mean flux and by turbulence itself, respectively; the third element is due to correlations between pressure and velocity

fluctuations and the last one represents viscous transport. This term is not considered in the present work, which implies that the TKE will be considered as being locally produced and dissipated.

- **B**. *Shear production term.* This represents the rate of generation of turbulent kinetic energy by the interaction of the Reynolds stress $(\overline{u_i'u_i'})$ with mean velocity shear $\frac{\partial U_i}{\partial x_j}$. Values of this term are positive and represent a gain of turbulent kinetic energy at the expenses of mean kinetic energy. The same term with a different sign appears in the mean kinetic energy equation (not shown).

- **C**. This term is known as the *buoyant production of turbulent kinetic energy* but –despite its name– it can also act to "destroy" it, depending on the background density profile, *i.e* an instable background density profile transfers TKE to potential energy and in this sense it is *destroyed.*

- **D**. The last term –without the negative sign– accounts for the viscous dissipation rate of turbulent kinetic energy. It is known as the *kinetic energy dissipation rate* (KEDR) and is commonly designated by an epsilon (ϵ). The importance of this term is capital and its values are normally in the order of those for turbulence production terms. Under considerations to be presented later, KEDR is calculated through estimations of the small–scale shear variance like $\epsilon = 7.5\nu\overline{(\frac{du'}{dz})^2}$ or by fitting the spectra of data to standard shapes considered to be universal.

2.3.2 Basics of Kolmogorov's Theory and of Turbulence Scales

Following Richardson's ideas, Kolmogorov (1941a, b) hypothesized that, for an isotropic turbulent flow, energy cascades from large scale fluctuations where turbulence extracts energy from the mean flow to the smallest fluctuations, where they can be affected by molecular viscosity, in a way determined solely by ϵ, which is an essentially inviscid process. However, statistics of the smallest eddies in a turbulent flow depend on two parameters: viscosity (ν) and dissipation rate (ϵ). This, so–called "direct cascade" is related to vortex stretching (Tennekes and Lumley, 1972). The physical picture emerging from Richardson and Kolmogorov's ideas is that of a large scale flow being unstable to eddies somewhat smaller in scale, and these eddies growing to develop still smaller eddies. This way, energy is transferred to smaller

and smaller scales in a cascade–like process ending with the generation of small enough eddies to feel the effects of viscosity. However, another vision of turbulence exists. Gibson (1999) argues that there is the possibility of an "inverse cascade" so that instabilities appearing at small scales propagate to larger ones from where a larger amount of energy goes into the turbulent flow, where it is finally dissipated to smallest scales.

Besides providing a physical picture for the understanding of turbulence mechanisms, Kolmogorov's ideas provide arguments to guess –by rigorous spectral analysis or by dimensional arguments– the spectral shape and energy flux thorough it. Argumentation is not reproduced here, yet it is exposed in many textbooks and for a through discussion see that of Monin and Yaglom (1981). Kolmogorov's ideas on turbulence also allow the scales at which specific physical processes start –or stop– being dominant are found. This way the existence of a range (called the *inertial range*) of wavenumbers (k) is established where inertial terms –but not forcing or dissipation– are dominant. In this range, as already commented, the energy spectrum (S) is only a function of the energy flux (ϵ) and of the wavenumber; dimensional arguments show that the functional relationship is given by

$$S(k) = K_c \epsilon^{2/3} k^{-5/3}, \tag{2}$$

where ϵ and k were previously defined and K_c is the universal Kolmogorov constant which is approximately equal to 0.5 for a one–dimensional and to 1.4 for a three–dimensional spectrum (Monin and Yaglom, 1981). Angular wavenumber notation is used, then k is measured in cycles per meter (cpm). This spectral form has been observationally verified many times, the first using observations of a very high Reynolds number flow in a tidal channel by Grant, Stewart and Moilliet (1961).

At high wavenumbers, in the inertial–dissipative subrange ($k \geqslant k_\eta$, with $k_\eta = 1/\eta_k$, and η_k defined by Eq. 5 ahead), where the energy spectrum depends not only on ϵ, but also on ν and is given by: $S(k) = K_c \epsilon^{2/3} k^{-5/3} \varphi(k/k_\eta)$, where φ is a nondimensional universal function which can be defined either experimentally or theoretically.

In order to specify $\varphi(k/k_\eta)$ theoretically, the equation for TKE balance should be spectrally transformed. Nonlinear turbulent transport among various scales trans-

forms to the energy transfer between the different wavenumbers, $F(k)$. This transport is significant in all of the wavenumbers. When turbulence is considered to be statistically steady, homogeneous, and locally isotropic, then the spectral energy equation (see Eq. 1) can be simplified to:

$$F(k) = \epsilon - 2\nu \int k^2 S(k) \, dk \tag{3}$$

where $S(k)$ is a 3D energy spectrum. To solve this equation, a closure between $S(k)$ and $F(k)$ has to be put forward.

Panchev and Kesich (1969) reviewed different closure schemes and proposed their own, giving the non dimensional spectrum:

$$S_{nd}(k_{nd}) = \left(k_{nd}^{-5/3} + \sqrt{\frac{3}{2}}k_{nd}^{-1}\right) \exp\left(-\frac{3}{2}k_{nd}^{4/3} - \sqrt{\frac{3}{2}}k_{nd}^2\right) \tag{4}$$

where $k_{nd} = kK_c^{3/4}/(\epsilon/\nu^3)^{1/4}$, and S_{nd} is nondimensionalized by $K_c^{9/4}(\epsilon\nu^5)^{1/4}$. This was a satisfactory solution for data available at that time (Stewart and Grant, 1962 and Grant *et al.*, 1968) and was later supported by numerous measurements in various natural environments (Gregg,1999). The corresponding one–dimensional spectra have no analytical form and must be obtained from (4) by numerical integration. An empirical, one –dimensional, universal shear spectrum $S_{sh}(k)$ introduced by Nasmyth (1970) is now also widely used as a reference spectrum in oceanographic applications.

Scales where TKE is dissipated by molecular diffusion due to viscosity –known as Kolmogorov's turbulence scales– for the length (η_k) , time (τ_k) and velocity (ν_k) are also derivable by dimensional argumentation. They are given by:

$$\eta_k \sim \left(\frac{\nu^3}{\epsilon}\right)^{1/4}, \tag{5}$$

$$\tau_k \sim \left(\frac{\nu}{\epsilon}\right)^{1/2}, \tag{6}$$

$$\nu_k \sim (\nu\epsilon)^{1/4}. \tag{7}$$

More precisely, according to Stewart and Grant (1962), scales where dissipation is the maximum are about $(6 - 10)\,\eta_k$. In their work, measured KEDR ranged from 10^{-9}

to 10^{-3} Wkg^{-1} and Kolmogorov's scale from 2×10^{-4} to 5×10^{-3} m. This is the range of spatial scales, according to term D of Eq. 1, to be considered when computing KEDR from the variance of small scale shear. Analysis of turbulent flows is mainly based on Kolmogorov's theory, and dimensional analysis is one of the most basically used tools. This makes it necessary to define many adimensional parameters (and some dimensional ones) to quantify the relative importance of the agents controlling flow behavior. Most of the parameters necessary for this work will be defined during the exposition, few of them –in a manner of small glossary– are briefly introduced here.

- **Ozmidov scale:** this is an important length scale in stratified flow study, defined as $L_O = \sqrt{\epsilon/N^3}$, where $N = \sqrt{-\frac{g}{\rho_0}\frac{\partial \rho}{\partial z}}$ is the Brunt–Väisälä frequency. N, also known as the buoyancy frequency, is the oscillation frequency of a fluid parcel displaced a small vertical distance from its equilibrium position in an stable environment. L_O is the vertical length scale at which the buoyancy force is of the same order of magnitude as the inertial forces and also the scale above which eddies are deformed by stratification. The Ozmidov scale is the largest that can overturn, *i.e.* buoyancy has only a minor effect on smaller scales but dominates larger ones. Overturning can occur at scales greater than L_O if internal waves are present. The variability range of this scale goes from a few cm in the thermocline to several hundred meters in weakly stratified and/or highly energetic flows. Because isotropy of turbulent fluctuations is amended when KEDR is computed from small–scale shear, comparison of their scales with the Ozmidov scale must be performed as an *a posteriori* test. (Note that L_O is a function of ϵ) Turbulence is considered isotropic and active when their spatial scales (L) are in the range $11\eta_k \leq L \leq 0.6L_O$.

- **Gradient Richardson's number:** is defined as the ratio of the squared value of the Brunt–Väisälä frequency and the mean squared value of shear $R_i = N^2/S_h^2$, with $S_h^2 = (dU/dz)^2 + (dV/dz)^2$ and U and V being the orthogonal components of the horizontal part of the velocity vector. It is indicative of the stability state in stratified flows (Miles, 1961). The evaluation of the gradient Richardson number by approximating local gradients by finite differences across layers is known as the bulk Richardson number (R_{i_b}).

- **Diffusivity:** is defined on the context of one of the most used (and useful, though questioned) closure schemes for the parameterization of Reynolds fluxes, consisting of considering $\overline{u'w'} = -K_m \left(dU/dz \right)$, $\overline{v'w'} = -K_m \left(dV/dz \right)$ and $\overline{b'w'} = -K_b N^2$ in the averaged Navier–Stokes equations; with K_m being the vertical diffusivity coefficient for momentum, K_b the vertical diffusivity coefficient for mass and $b' = (g/\rho_o)\, \rho'$ the buoyancy. In the same context other diffusivity coefficients can be defined for scalars like salinity and temperature. This work is only related to K_b, which is later analyzed in light of a parameterization of K_b as a function of the Richardson number.

- **Flux Richardson number.** R_f, is a metric of the shear efficiency of mixing and is defined as the ratio of the C term and the B term of Eq. 1. This ratio reflects the increase of potential energy of a fluid divided by the production of turbulent kinetic energy. It is defined positively for stable stratification and negatively for instable (convective) background.

- **Mixing efficiency:** the parameter $\gamma = R_f/(1 - R_f)$ is the mixing efficiency (Dillon, 1982). It is equivalent to the ratio of C and D terms of Eq. 1. Because for well developed turbulent fluxes it is found that R_f values are close to 0.166, γ it is normally considered to be constant and equal to 0.2. However, Dillon (1982) considers this a good approximation only for weakly forced mixing regimes. A wide scatter of γ values has bean reported by Yamazaki and Osborn (1993) and numerically reproduced by Smyth and Moum (2000). In general, γ and R_f values depend on the state of turbulence. In this work, turbulence at the UQHL is considered active and the canonical value of 0.2 is used.

- **Reynolds buoyancy number:** an adimensional number defined as $R_{e_b} = \epsilon/\nu N^2$. It is used as a metric for the validity range of the isotropy assumption in the study of turbulence in stably stratified waters. Gargett *et al.* (1984) consider that this assumption holds if $R_{e_b} > 200$, but some other authors (*e.g.* Jonas *et al.*, 2003) found that for values over $R_{eb} > 20$ the assumption of isotropy may hold. An alternative definition is obtained including a normalizing constant α usually considered to be equal to 30 in $R_{e_b} = \epsilon/\alpha\nu N^2$. This way isotropy hold from $R_{e_b} \geq 1$. The last definition is used in this work.

<div align="right">CHAPTER 3</div>

Microstructure data: measuring and processing

During the North Atlantic campaign –to be described in next chapter– a set of microstructure data was collected using an MSS profiler (Prandke and Stips, 1998; Prandke *et al.* 2000). Microstructure profiling (usually 2–3, rarely 7–8 casts taken for station; see Figure 9 in Chap. 4) was conducted in parallel with CTD measurements but –due to weather conditions– not at all of the stations. To the best knowledge, these are the first microstructure measurements acquired in the region. This chapter starts with an exposition of the technical specifications of used microstructure profiler; this is followed by an overview of one of the standard methodologies in common use for the processing of raw microstructure data, which is presented together with the alternatives used in this work for the calculation of the falling velocity of the instrument falling, the edition and the despiking of microstructure data. After that, the two main methods in common use for the obtention of KEDR are explained and some examples of the obtained results are shown. Finally, filtering methods used for denoising shear data are presented, also with some comparative examples.

3.1 The microstructure Profiler

A commercial MSS (Micro Structure System) profiler developed by a consortium of companies, which were participants of the MITPC project (Improved Microstructure Technologies for Marine Near Surface Flux Studies), funded by the European Community (Prandke *et al.* 2000), was used in this study. The profiler consists of a stainless steel cylinder, 100 cm in length and 10.6 cm in diameter. It encapsulates electronics and a set of sensors at its lower end, which are protected by a guard (see Fig. 5). The data is transferred to an on–board computer via an almost neutral buoyancy elastic cable. The same cable is used to recover the profiler

after each free–falling cast. To maintain a constant falling speed of about 0.7 ms^{-1}, the profiler should have a negative buoyancy of about 1 kg, which can be regulated by special buoyancy rings of different weights. The profiler carries microstructure sensors (for small–scale shear and fast temperature), sensors of conductivity, temperature and pressure, and an accelerometer. The sensitivity of the microthermistor is $0.001\,^{\circ}$C and its response time is 7 ms. The precise temperature sensor (Pt–100) has a sensitivity of $0.001\,^{\circ}$C, an accuracy of $0.010\,^{\circ}$C, and a time response of 160 ms. The corresponding characteristics of the 7–pole conductivity cell are 0.001 mS/cm, 0.01 mS/cm, and 100 ms, respectively. The vertical resolution of the airfoil shear probe (PNS 98) is limited to 0.5 cm. This value is determined by the geometry of the sensor. The laboratory calibration tests of the shear probe indicate lowest measurable dissipation rates of about 10^{-11} Wkg^{-1}, although the lowest in situ noise level of shear measurements is equivalent to $\sim 10^{-9}$ Wkg^{-1}.
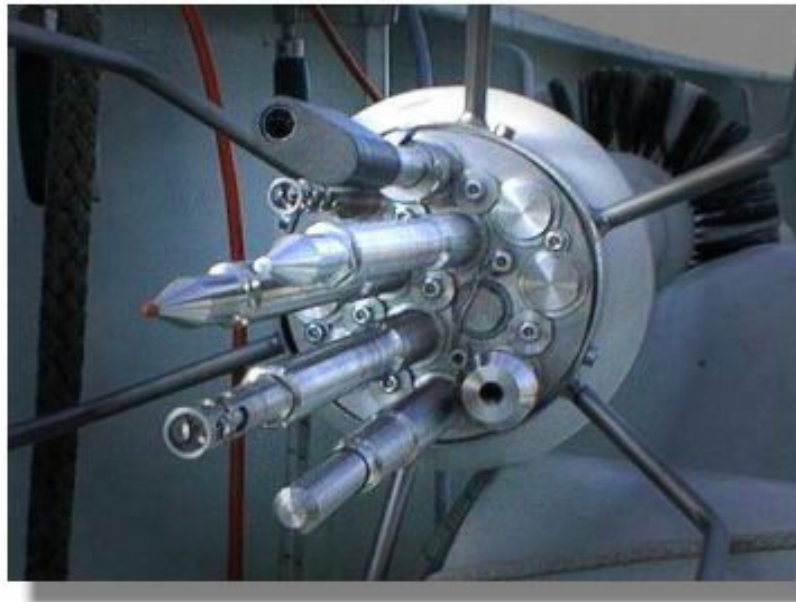
Figure 5. The MSS rear end showing their sensors. For more details access the homepage http://www.isw-wasser.com/products/mss.html

3.2 Editing and despiking

Microstructure data are usually noisy, especially in the very first meters below the surface. Therein, the signals are contaminated by ship–induced movements and the unstable falling speed of the profiler. The data at the end–points of the cast are also heavily contaminated, because of the cable tension, which introduces high–amplitude vibrations. Since starting and ending segments in the cast cannot be recovered by any denoising procedure, they were removed from the analysis. Spikes and faulty data segments are always present in microstructure records, generated by the presence of numerous debris (organic and inorganic), abrupt failures in communication links or malfunctioning of the sensors, and it is not possible to eliminate them completely (Moum and Lueck, 1985). However, these spikes and contaminated data segments must be identified and removed. Editing microstructure data cannot be done manually, considering the huge amount of information collected by microstructure sensors and, therefore, various statistical approaches must be applied. For example, Prandke *et al.* (2000) suggest excluding bad samples or assigning a fixed value to them by calculating the mean μ_0 and standard deviation σ_0 for each consecutive pre–determined segment and replacing that data outside the interval $(\mu_0 \pm n\sigma_0)$ where $n = 2.7$ with μ_0. This type of despiking works well if those data limits are known *a priori*, or noise is generated by a known source, but this is usually not the case for microstructure measurements. For the edition of microstructure data used in this work, it was developed an interactive and efficient graphic MATLAB interface to identify isolated spikes, bad values or gaps in the records. Upon completion of this step, a procedure similar to that of Prandke *et al.* (2000) was applied, but instead of replacing bad samples by the mean value calculated at each segment, a cubic spline interpolation was used if the number of bad or missing points were less than fifty (about 5 cm of the record) and $n = 2$ was used. If a data gap was larger than 5 cm, the record was divided into several separated segments, with none of the gaps exceeding 5 cm.

3.3   Falling velocity and small–scale shear profiles

Accurate calculations of the falling velocity of the profiler V_f is a very important step in microstructure data processing because the output signal of the airfoil sensor e_{out} is proportional to V_f^2, and proportionality is given by $e_{out} = \rho S_0 V_f^2 \frac{du}{dt}$, where S_0 is the cross–sectional area of the cylindrical part of the sensor (Paka *et al.*, 1999). The time derivatives $\left(\frac{du}{dt}\right)$ were calculated by finite differences, with further filtering by a Butterworth low–pass filter, which had a frequency response function equivalent to a 3–point running average filter. To convert time–sampled signals to depth–dependent ones, a proper estimation of falling velocity is required from the pressure signal, which is also contaminated, mainly by wave–induced variations of the sea–surface and possible tilting of the profiler. To reduce fluctuations in the pressure signal, which in principle ought to be a monotonic function of time, it was filtered by fitting a second order polynomial to consecutive segments of data (usually 25 dbar in length) and then connecting the segments using 5–point running average filtering over the whole profile. The falling velocity is then computed by taking the time derivative of the smoothed pressure signal, minimizing errors in the calculation of $\frac{du}{dt}$ and hence ϵ.

3.4   Calculation of the dissipation rate

In the next two sections the fundamentals of the two methods used to calculate ϵ from microstructure shear measurements are explained and some examples of obtained results are given.

3.4.1   Computation of variance

In the equation for turbulent kinetic energy balance (Eq. 1) it was established that the term labeled "D" of that equation accounts for their dissipation rate. Such a term is defined as

$$\epsilon = 2\nu \overline{e'_{ij}e'_{ij}}, \tag{8}$$

where $e'_{ij} = \frac{1}{2}(du'_i/dx_j + du'_j/dx_i)$ is the second order tensor, which is known as the *fluctuating strain rate tensor*. This tensor symbolizes the deformation rate of fluid particles due to the velocity gradients fluctuation field; the commonly used value

for kinematic viscosity[1] ν for water at 20 °C is about 10^{-6} m^{2}s^{-1}. This expression for ϵ clearly indicates that only at small scales, where the strain rate is high, is this term of the same order as the other terms in the equation of turbulent kinetic energy balance. Furthermore, (8) also shows that KEDR can be computed using the variance of small–scale shear: $\overline{(du_i'/dx_j)^2}$.

In aquatic systems, airfoil sensors mounted in different types of profilers allow one shear component to be measured, or two components, if sensors are combined (Osborn, 1974). Therefore, local isotropy of turbulent fluctuations has to be assumed to calculate KEDR. If so, Eq. 8 reduces to

$$\epsilon = 7.5\nu\overline{\left(\frac{du'}{dz}\right)^2}, \tag{10}$$

where all turbulent scales must be considered for variance computation.

3.4.2 Comparison with universal spectra

Universal spectra provide not only a better understanding of turbulence dynamics, but also help to infer information about KEDR when shear cannot be satisfactorily resolved experimentally in a wide wavenumber subrange (whether because of instrument limitations, or noise contamination). Because shear spectrum $S_{sh}(k)$ is k^2 times the velocity spectrum $S(k)$, in locally–isotropic turbulence, KEDR can then be calculated using the one–dimensional velocity spectrum $S(k)$ as follows:

$$\epsilon = 15\nu\int k^2 S(k)dk. \tag{11}$$

In this case, a universal curve is used as a guidance to recover the corresponding loss of variance in a disregarding range by introducing a correction factor depending on the cut–off frequency and KEDR (Peters *et al.*, 1988 and Prandke *et al.*, 2000).

In Fig. 6, a nondimensional experimental shear spectrum measured in the upper ocean (line with circles) is plotted together with the corresponding nondimensional universal Panchev–Kesich (heavy line) and the Nasmyth (dashed line)

---

[1]To include dependence of ν (m$^2 s^{-1}$) on temperature measured in °C the following polynomical function is widely used:

$$\nu = (1.79247 - 0.05126103T + 0.0005918646T^2)10^{-6} \tag{9}$$

shear spectra. The Kolmogorov scaling, $S_{nd}(k) = \frac{1}{2\pi} S_{sh}(k) / (\epsilon^3/\nu)^{1/4}$ and $k_{nd} = 2\pi k / (\epsilon/\nu^3)^{1/4}$ were used to adimensionalize the spectra with an integrated estimate of $\epsilon = 2 \times 10^{-8}$ Wkg^{-1}. In this case, the experimental spectrum shows good agreement with the universal spectra at high wavenumbers, but not at low k. However, integration of the normalized Panchev–Kesich spectra shows that the variance within the unresolved segment at low k accounts for only about 5% of the total variance.

When the same experimental spectrum is nondimensionalized using different ϵ values, say two times greater (crosses) and two times lower (stars), *i.e.* $\epsilon = 4 \times 10^{-8}$ Wkg^{-1} and $\epsilon = 10^{-8}$ Wkg^{-1}, the obtained curves depart markedly from the universal spectra, indicating that fitting is a sensitive procedure for obtaining correct estimates of KEDR. Note that the Panchev–Kesich spectrum contains more power at lower wavenumbers and rolls off slightly faster at high wavenumbers, compared to the Nasmyth spectrum. These differences should be considered for high dissipations, when small–scale shear at low wavenumbers is not well resolved and, therefore, an appropriate correction when calculating the shear variance must be introduced.

Fitting the experimental spectra to the empirical procedure has an advantage over the variance calculation, because it is not necessary to do any cleaning of the shear signal. The fit need not to be applied to the whole wavenumber range, but only to a reliable "clean" subrange, where the universality is assumed.

Fig. 7 shows an example of the fitting of the shear spectra, taken from various turbulent layers, and which are plotted together with a family of Panchev–Kesich theoretical spectra calculated for different values of dissipation rates shown in the plot in Wkg^{-1}. Before fitting, the experimental spectra (crosses) were usually smoothed (dotted lines) and then the KEDR was determined from the closest theoretical curve in a wavenumber subrange of the best fit. If the smoothed spectra fit a number of theoretical curves within several subranges nicely, the corresponding dissipation rates were averaged to obtain the most reliable mean estimate of the KEDR. The lowest spectrum in the figure represents a noise–level segment of these shear measurements, taken in the upper pycnocline of the North Atlantic (Roget *et al.*, 2004).

So far, no formal parameters have been suggested to quantify the goodness of fitting for shear spectra as has been done when calculating KEDR by comparing
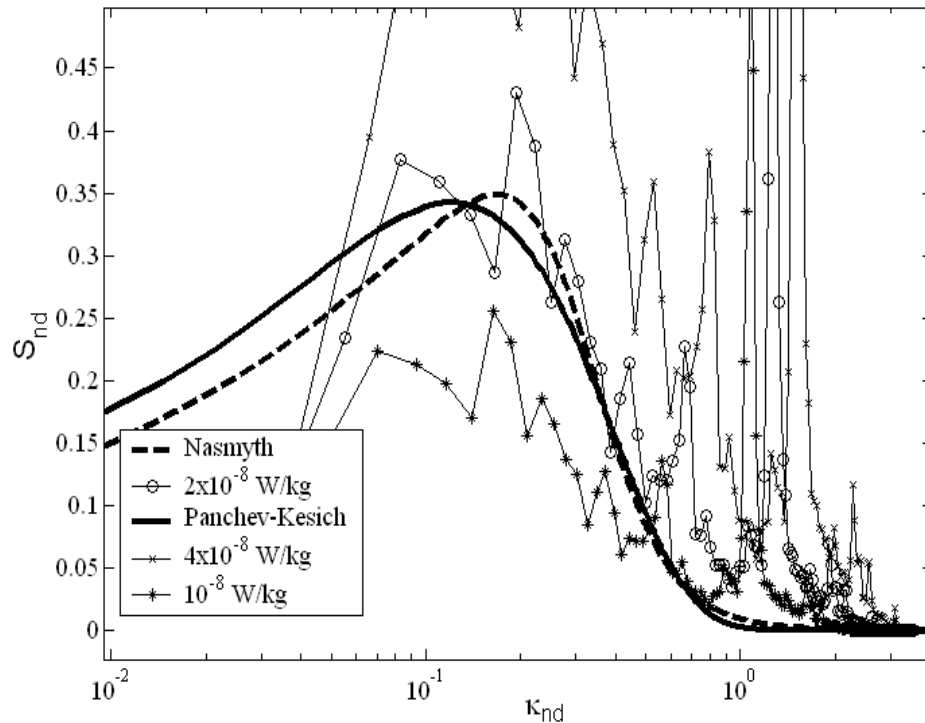
Figure 6. Theoretical (continuous line: Panchev–Kesich) and experimental (broken line: Nasmyth) reference spectra compared with the spectra computed from small–scale shear data (Atlantic cruise) assuming different dissipation rates as indicated in the figure legend.

microstructure temperature spectra with the universal Batchelor spectrum [Ruddick *et al.*, 2000; Luketina and Imberger, 2001 and Sanchez, 2001].

Although averaged velocity spectra often exhibit the universal shape, individual spectra in low energetic regimes can deviate substantially from the universal and therefore the variance loss correction, which is based on the assumption of universality, introduces a random error. Regarding the assumption of universality, Moum *et al.* (1995) consider that: "Systematic analysis to compare measured spectra with universal form is needed. This is a topic for further research requiring a careful consideration of the physics involved". However, when KEDR is not very low and isotropic conditions are fulfilled, even individual spectra usually behave as universal.
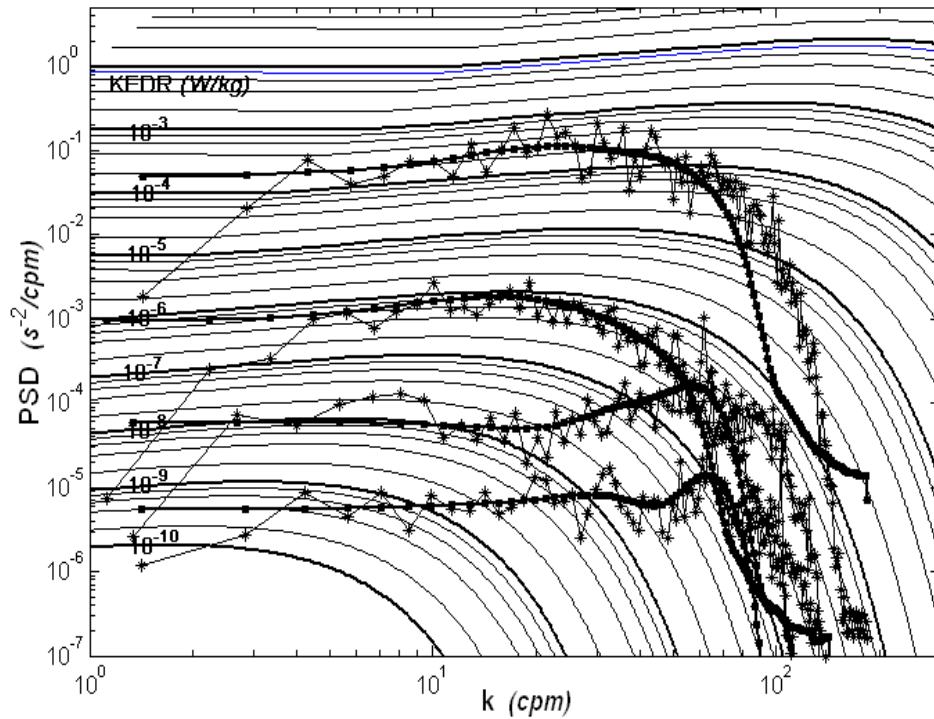
Figure 7. The oceanic shear spectra in the background of a family of theoretical Panchev-Kesich spectra (smooth lines) before (crosses) and after (dots) denoising. Thicker lines indicate one decade of alteration in the dissipation rate, as indicated by the numbers next to the curves.

3.5 Denoising Shear Data

Whether the kinetic energy dissipation rate is computed from the variance of small–scale shear or by fitting the empirical spectra with the universal curves in the inertial–viscous subrange, both approaches deal with noise–contaminated signals. Identification of noise is a mandatory task, which can be of help in choosing the best possible method for KEDR computation and even sometimes in avoiding denoising, as was shown in Fig. 7. However, cleaning data is still an important step that can be done either by using several classical digital filters, or by wavelet denoising, as applied to measurements taken with the MSS profiler.

3.5.1 Classical digital filtering

Low frequency noise in microstructure shear data is usually caused by a combined effect of the thermal drift of the airfoil probe and the low frequency motions of a profiler. To clean this kind of data contamination, classical digital high–pass filters can be applied (Press *et al.*, 1990). The Butterworth filter was used to remove possible large–scale fluctuations in shear signals with scales larger than 0.5 m, which corresponds to half of the total instrument length. This filtering was applied directly to the airfoil signal before computing the physical shear. The high–frequency electronic noise was removed by a low–pass digital filter. Sometimes, a localized, narrow–frequency noise can appear in the signal because of the mechanical resonance of the profiler. Such localized peaks, around 40 Hz in this case, can be deleted by a Lanczos window (Hamming, 1983) designed for a specific wavenumber band. A band–pass Lanczos filter has a very sharp frequency response function and therefore hig–amplitude peaks can be removed without significant changes in the adjacent frequency bands.

3.5.2 Wavelet denoising

Wavelets are being used in geophysical applications to identify localized structures (Foufoula *et al.*, 1994) and they have recently been found to be useful in denoising microstructure temperature data before computing Thorpe scales in thermally stratified layers (Piera *et al.*, 2001). Wavelet denoising projects (decomposes/transforms) a signal onto a specific orthogonal function base, which accounts for different scales (decomposition levels). Once the coefficients (base coordinates) are obtained, the denoising procedure thresholds them above a certain level in order to keep only the non–contaminated signal removing the noise selectively from the scales that should be filtered. After thresholding, the inverse transform is performed.

Noise amplitudes are often comparable with amplitudes of real microstructure signal from a shear probe. Moum and Lueck (1985) showed, for example, that the lowest dissipation level of about 10^{-10} Wkg^{-1} measured by their profiler was a reflection of the pseudo dissipation rate, which can be calculated from the accelerometer signal (Prandke and Stips, 1996). Yamazaki and Osborn (1993) found a noise level of KEDR close to 10^{-9} Wkg^{-1}. Similar values are reported by Roget *et al.* (2004).

This can be seen in Fig. 7, where spectra with low energy levels exhibit a characteristic flatness at low wavenumbers, indicating a wide–range of noise. This type of contamination could be related to artificial fluctuations produced by a protection guard and a float used to prevent mechanical damage to the profiler during measurements, however a definite source of this white noise has not been identified yet. In these cases, the wavelet approach can help to reduce contamination in microstructure data.

An example of wavelet denoising capabilities is given in Fig. 8, based on the Atlantic measurements. In the left panel, the original shear spectra (crosses) for two 0.5 m segments of data are shown. The upper one pertains to the near–surface turbulent layer and the lower one is from the thermocline. Wavelet denoising can remove high–frequency amplitudes and smooth the resonant noise in a different way than the Butterworth low–pass and Lanczos band–pass filters discussed above. The resulting spectra, after the wavelet denoising procedure, are shown in the figure with squares.

Furthermore, if white noise is assumed, it can be removed from all the scales by lowering the detailed coefficients for all levels of decomposition. In this case a threshold value of 0.06 s^{-1} was used for all of the stations. This value was chosen after careful analysis of the detailed coefficients at low–dissipation segments found below the upper turbulent layer. For these segments, the first level of decomposition –which in this case accounts for scales in the range $(1-2) \times 10^2$ cpm– reflects a pure noise because it was assumed that no physical signal at these wavenumbers can be measured. Threshold values at several stations, where the weather conditions ranged from calm to stormy winds, were determined based on the median of the first level of detail coefficients. The mean value of the threshold was found to be of 7.1×10^{-2} s^{-1} with standard deviation of 9×10^{-4} s^{-1}, indicating a relatively constant background noise. Therefore 6×10^{-2} s^{-1} was chosen as a conservative estimate for the threshold. The spectra obtained after wavelet denoising (see the open dotted line in Fig. 8) indicates that the noise reduction is more important for low–dissipative layers than for highly–dissipative patches; in fact, the spectrum for the latter is very little affected by the wavelet denoising.

In the right panel of Fig. 8, the KEDR profiles calculated at each consecutive

2–meter segment using different approaches are presented. A comparison of the dissipation profiles obtained from the shear variance after only high and low–pass filtering (heavy line) with those computed after wavelet denoising (dashed line) show that the levels and the structure of the KEDR profiles in the upper turbulent layer are almost unmodified by the wavelet denoising. However, below the thermocline the difference made by wavelet denoising is profoundly evident. A third KEDR profile (thin line) is also shown in the right panel of same figure. This is obtained by fitting non–denoised spectra with universal curve.

In this work, after editing, despiking and denoising shear data –following procedures mentioned in previous sections– calculated spectrum for every one meter section of profiles was compared to the theoretical Panchev–Kesich form (as shown in Fig. 8) for the estimation of the kinetic energy dissipation rate. The obtained values will be used for the analysis to be presented in Chapter 6.
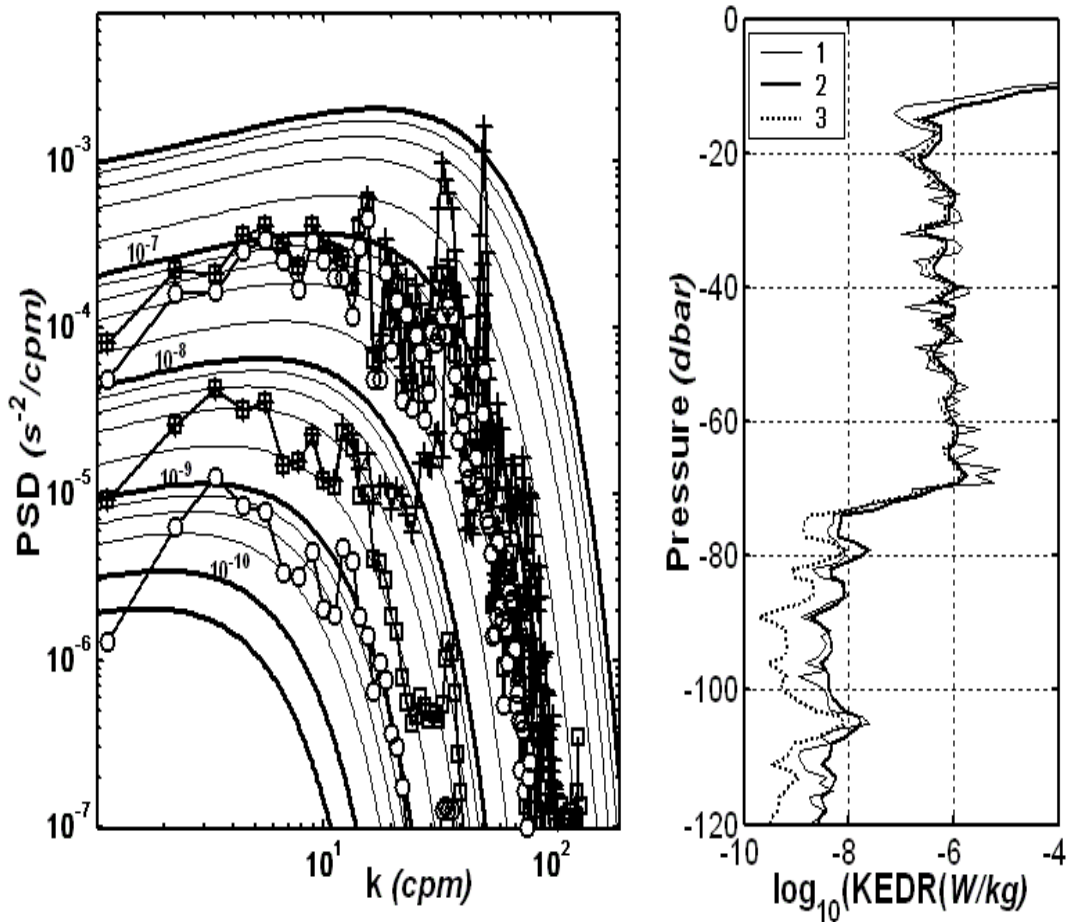
Figure 8. Left panel: Spectra of two different segments of shear data after different denoising options compared to a series of Panchev-Kesich curves for various KEDR. The original spectrum (line with crosses); the same one after high-pass filtering (line with squares); and after wavelet denoising (line with circles). Right panel: The kinetic energy dissipation rate, KEDR, profiles calculated for the same data according to different approaches: (1) fitting experimental spectra with the theoretical ones within a non-contaminated wavenumber range; (2) using the variance of small-scale shear signals after removing high frequency noise; (3) using the variance of small-scale shear signals after wavelet denoising (high-pass filtering and thresholding).

CHAPTER 4

Observations in the North Atlantic

As mentioned in previous chapters, data used for this work come from an observational campaign conducted along a hydrographic line crossing the North Atlantic Ocean, a transect following approximately the $53\,°$N parallel. In the first section of this chapter concise descriptions of the cruise, the instruments used, and the data sets obtained (with the exception of those of the microstructure which were introduced in the previous chapter, and whose results will be presented in Chap. 6) are given. The following section explains the methodology used for the calculation of bulk fluxes –heat, mass and momentum– from meteorological data and presents the obtained results. Next, the prevailing hydrographic conditions and dominant currents found during the experiment are presented within the context of known climatology of the region. After that, the Ekman transport as calculated from the ADCP observed velocity field is discussed and, finally, the methodology used to estimate the ageostrophic currents field which is presented and discussed.

4.1 The Cruise

From April 17 to 1 May 2001 an oceanographic cruise, organized by the P.P. Shirshov Institute of Oceanology of Moscow[1] across the North Atlantic Ocean on board R/V Akademik Ioffe. The cruise started at the port of St. John's, Canada, and concluded at the port of Kiel, Germany. Cruise track is shown in Fig. 9. It covered 42 hydrographic stations where data about oceanic and atmospheric phys-

---

[1]Other participating institution were:
Universitat de Girona, Girona, Catalonia, Spain;
Arizona State University, Tempe, AZ, USA
McMaster University, Canada.

ical variables were gathered. Sampling started at the Newfoundland shelf break (52.700 ° N, 51.883 ° W) and finished at the continental slope of Ireland (51.433 ° N, 14.433 °W); The distances between stations varied but was 50 km on average except during the first stage, crossing the Labrador Current, where denser (15 km on average) sampling was used. Collected data included: full–depth CTD measurements using a Neil Brown Mark III (NBIS) profiler attached to a twelve–bottle Rosette water sampler system, this system was used to take discrete temperature measurements to keep control of the CTD quality measurements and water samples to trace concentrations of dissolved oxygen and silicates; high resolution CTD velocity shear microstructure measurements were collected using an MSS profiler –see the previous chapter– from surface to the 200 meters of depth at most of the stations; vertical profiles of U (east–west) and V (north–south) components of the velocity vector were measured in the range of 16–600 m with a vertical resolution of 8 meters and the measurements were collected along the transect and at drift by a ship–mounted ADCP profiler equipped with GPS navigation; finally, standard meteorological observations were continuously collected during the cruise by an on-board automatic meteorological station, the "Wetos 625", and also using a portable automatic system, the "Davis Weather Monitor II". Stations with MSS and NBIS measurements are shown in Fig. 9 by solid circles. The MSS casts were skipped at a number of stations (open circles) because of severe weather conditions and/or shortage of personnel.

Prior to the cruise, all NBIS sensors were calibrated at the testing facility of the Federal Department of Marine Navigation and Hydrography (BSH, Hamburg). The CTD data were processed according to the WOCE standards and the salinity obtained at every station with an Autosal 8400B on–board salinometer was to control the conductivity channels of NBIS.

The main objective of the cruise was to contribute to the study of interannual and decadal variability of the thermohaline water structure in the transitional zone between subtropical and subpolar gyres of the North Atlantic. The expedition is part of the following scientific programs: "World Ocean" and "Purposive Scientific–Technological Program", both of the USA Federal Research Program; "Program of Basic Research", of the Russian Academy of Sciences; and the international WOCE–
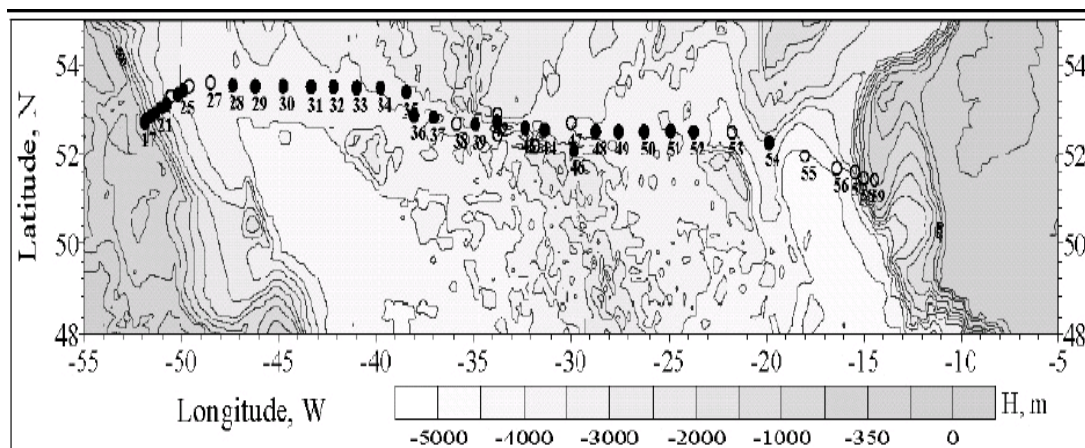
Figure 9. The cross-Atlantic transect taken by R/V Akademik Ioffe in 2001, 17 April – 1 May. Stations with MSS and NB measurements are marked by filled circles; those with only NB profiling are shown by open circles. The first digit in the station numbers is omitted; they must be read as 917–959.

CLIVAR program. For detailed information about the cruise see Tereshchenkov (2002).

4.2 Atmospheric and Hydrographic Conditions

In this section, a general description of the atmospheric and hydrographic conditions found along transect is provided. For the hydrography, it is done in two parts: first the basin scale structure of hydrographic field is described in the context of what is expected to be found in the region; then the upper two hundred meters of the transect are described in the context of the observed meteorological conditions.

4.2.1 Meteorological Data

Standard meteorological information was recorded at an elevation of 18 meters from the ship's mast. The obtained meteorological data –reduced to the standard elevation of ten meters– and total cloudiness[2] are presented in Figures 10 and 11.

---

[2]Obtained from NASA databank located at the internet address http://ingrid.ldgo.columbia.edu/SOURCES/.NASA/.ISCCP/.D2/ and interpolated to station position.
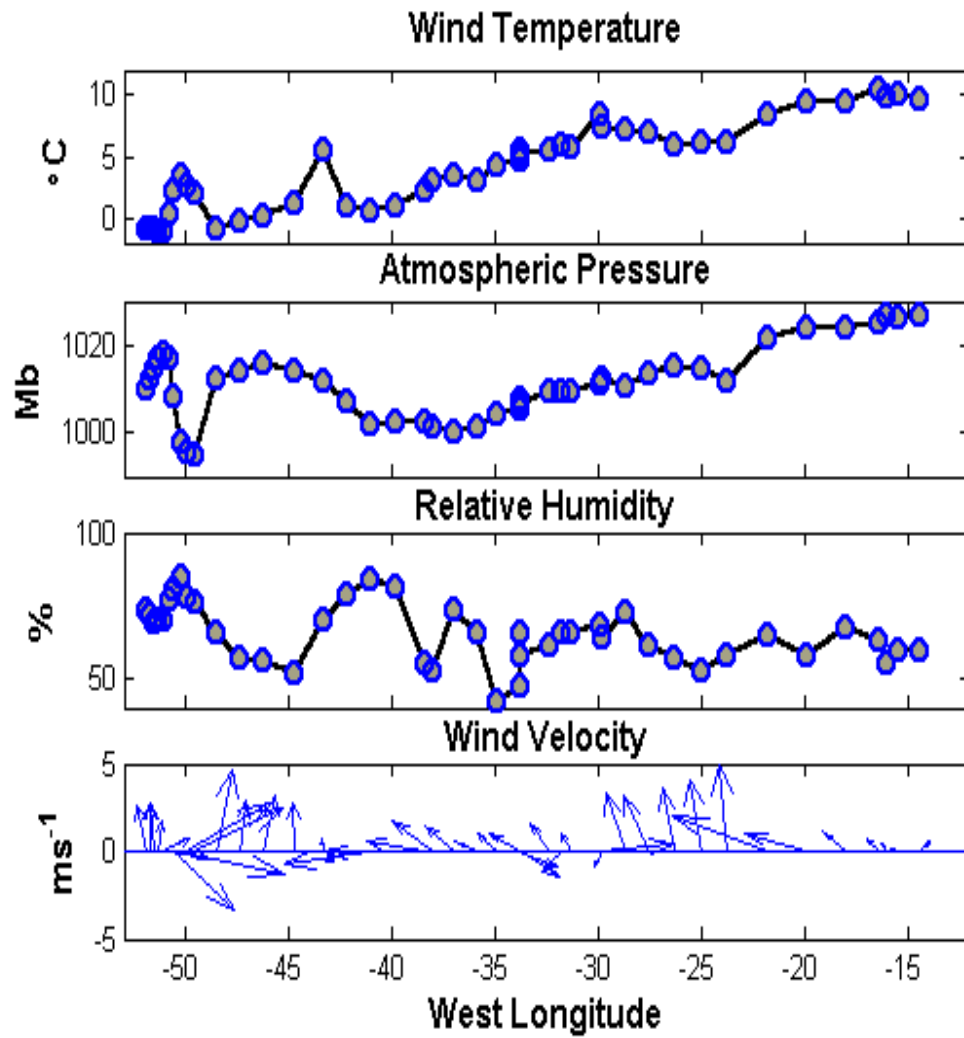
Figure 10. Average values during the time used to take measurements at each station of wind temperature, atmospheric pressure, relative humidity and wind velocity.
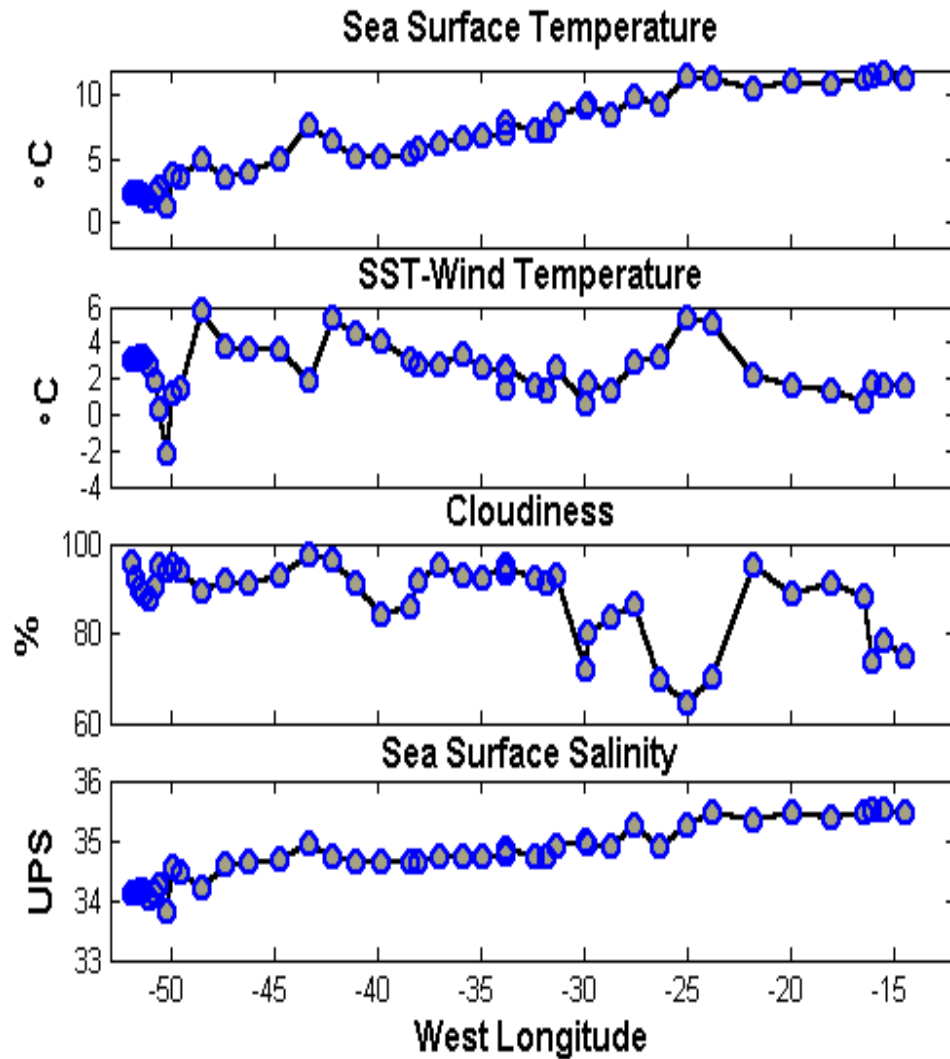
Figure 11. Average values during the time used to take measurements at each station of sea surface temperature (SST), SST minus wind temperature, cloudiness as measured by satellite and sea surface salinity.

In addition, wind velocity was also measured using a sonic anemometer but only the average values at each station are used. All of these variables are necessary to estimate of the bulk fluxes.

West of ∼45 °W, all of the variables [wind velocity, relative humidity, sea surface temperature (SST), wind temperature and atmospheric pressure] show the typical behavior of a frontal zone: local extreme values in a relatively short distance –i.e. intense gradients– corresponding to the Labrador Current and to the edge of the Gulf Stream as they become the North Atlantic Current. This behavior is even evident in variables that usually exhibit a close–to–random character, like relative humidity and cloudiness. East of that latitude most of the variables – with the exception of cloudiness and relative humidity– show values rising almost continuously to the east, except at a single station close to ∼42 °W where there was a wind temperature maximum, and apparently a bad data point which, nevertheless, is supported by a local maximum in sea surface temperature and in salinity. It worthwhile to point out here that stormy conditions prevailed during most of the time and wave height –data not reported– was sometimes estimated to be around four meters, with some events considerably higher. Cloudiness was almost always around 95% except for the transect between 30 °W and 27 °W where it fell to values close to 60%. Differences between the SST and wind temperature are also shown, and it can be seen that except for one station, close to 50 °W, they were always positive, i.e. ocean surface temperature was greater than air temperature. The sign of these differences determines the direction of latent heat fluxes, conventionally considered negative if going into the atmosphere.

Next, atmospheric data and ocean surface information were used to calculate turbulent heat fluxes and buoyancy fluxes.

Bulk Heat Fluxes

Turbulent fluxes of momentum (τ_w) and heat (sensible Q_H, and latent Q_L) are defined by the standard Reynolds averages (see Bussinger *et al.*, 1971) which are expressed by:

$$\tau_w = \rho_a \overline{u'w'} = -\rho_a u_*^2, \tag{12}$$

$$Q_H = \rho_a C_{pa} \overline{T'w'} = -\rho_a C_{pa} u_* T_*, \tag{13}$$

$$Q_L = \rho_a L_e \overline{q'w'} = -\rho_a L_e u_* q_*, \tag{14}$$

where u', w', q' and T' are, respectively, the fluctuations of horizontal and vertical wind velocity and those of specific humidity and temperature, while ρ_a, C_{pa} and L_e stand for air density, specific heat of air and latent heat of vaporization. The "starred" variables on the left–hand side (u_*, T_* and q_*) are scaling parameters related to the Monin–Obukhov similarity theory (MOST) and their definition is implicit in equations 12, 13 and 14: $u_* = \sqrt{-\overline{u'w'}} = \sqrt{-\tau_w/\rho_a}$, which is known as "friction or frictional velocity" and is one of the most fundamental parameters in MOST; while $T_* = -\overline{T'w'}/u_* = -Q_H/\rho_a C_{pa} u_*$ and $q_* = -\overline{q'w'}/u_* = -Q_L/\rho_a L_e u_*$. In practice, formulas 12, 13 and 14 are not very useful because it is not easy to obtain reliable measurements of fluctuating variables. Instead, a set of standard formulas –known as *bulk formulas*– expressing fluxes in terms of more easier–to–measure variables (Smith *et al.*,1996) are used:

$$\tau_w = -\rho_a C_D U(u_s - u_l), \tag{15}$$

$$Q_H = \rho_a C_{pa} C_H U(T_s - T_l), \tag{16}$$

$$Q_L = \rho_a L_e C_E U(q_s - q_l). \tag{17}$$

Here, u_s is the ocean surface current, T_s is the temperature and q_s the water vapor ratio at the ocean surface level, while u_l is one of the horizontal wind velocity components and T_l and q_l stand for those values of temperature and humidity measured at the standard level of $z_l = 10$ m above the surface [in most of the measurements from a ship mounted instruments z_l is not equal to 10 m, and observations need to be corrected assuming a logarithmic vertical profile for the atmospheric variables]; U is the average wind speed, while C_D, C_H, and C_E are coefficients parameterizing momentum (the drag coefficient), sensible and latent heat transfer, respectively.

Values of transfer coefficients are traditionally calculated following the MOST formalism [see Large and Pond (1982), Panofsky and Dutton, 1984; Geernaert, 1990; Smith *et al.* (1996)] in which:

$$C_D = \kappa^2 \left(\ln \left(\frac{z}{z_0} \right) \right)^{-2} \tag{18}$$

$$C_H = C_D^{1/2} \kappa \left(\ln \left(\frac{z}{z_0} \right) \right)^{-1} \tag{19}$$

$$C_E = C_H^{1/2} \kappa \left(\ln \left(\frac{z}{z_0} \right) \right)^{-1} \tag{20}$$

where κ is the von Karman constant considered to be equal to 0.41, and $z_0 = \alpha u_*^2/g$ is the roughness parameter and the constant α in their definition is known as the Charnok constant [Charnok, 1955], whose value is usually considered to range between 0.010 and 0.035 (Garrat, 1992). Variants of this formalism are many and they may be classified mainly into three groups; first: C_H and C_E are considered as being constant and equal to 1.1×10^{-3} [DeCosmo et $al.$, 1996]; second: C_H and C_E equal but proportional to an arbitrary function of bulk Richardson number $C_H = C_E = 0.9 \times 10^{-3} f(Ri, z/z_0)$ [Makin, 1996 and Makin, 1998]; and third: those where the roughness parameter z_0 is considered to be a function of friction velocity [Smith, 1980; Doneland, 1990; Beljaars, 1994; Fairall, 1996].

Formulas (15, 16 and 17) were used to calculate bulk fluxes using the data set collected during the Atlantic Ocean experiment. Clearly, results depend on the chosen values for transfer coefficients which in turn depend on the chosen MOST variant used for their calculation. For present calculations it was used the TOGA COARE scheme (Fairall et $al.$, 1996) was used and implemented in a set of MATLAB functions released in the Sea–Mat internet site[3]. In this variant –of the third type of those mentioned in the previous paragraph– the roughness length is calculated by an iterative process using the equation of Smith (1988)

$$z_0 = \alpha \frac{u_*^2}{g} + 0.11 \frac{\nu}{u_*}. \tag{21}$$

Besides, three corrections are included: gustiness velocity correction [Godfrey and Beljaars, 1991] in the computation of the mean wind speed; cool–skin layer correction for non–radiative sea surface measurements; and the Webb correction (Webb, 1980) to the latent heat fluxes. This last correction is done to satisfy the requirement of zero dry mass flux through the ocean surface and its magnitude is normally around 4 Wm^{-2}. Details about the algorithm are extensively presented in Fairall et $al.$ (1996).

---

[3]$http://sea\text{–}mat.whoi.edu/index.html$

Radiative Fluxes

Long–wave radiation

Net long–wave heat fluxes (Q_B) were calculated following the Berliand and Berliand (1952) approach, considered to be the best option by Fung *et al.* (1984), and also recommended by Fairall *et al.* (1996). The approach consists basically of considering the ocean surface as a gray body, and to parameterize the atmospheric influence on long–wave radiation by the temperature difference between the atmosphere and ocean surface, water vapor pressure and a cloud correction factor, that is

$$Q_B = 4\varepsilon_w \sigma T_a^3 (T_s - T_a) + \varepsilon_w \sigma T_a^4 (0.39 - 0.05\sqrt{e(T_a)})C_f, \qquad (22)$$

where ε_w is the emissivity of water, σ is the Stefan–Boltzman constant, T_s is the already defined surface temperature and T_a the air temperature measured at the surface, e is water the vapor pressure and C_f is a cloud correction factor. In general, C_f is a function of the cloudiness fraction (C) having the form $C_f = 1 - a_1 C^1 - a_2 C^2$, where the value of the coefficients depend on the dominant cloud type, which may vary from region to region and from season to season. Fung *et al.* (1984) consider that it is not clear which parametrization is best for C_f . In this work, that proposed by Bunker (1976) $[C_f = 1 - 0.72C]$ was used because it is specifically formulated for the North Atlantic Ocean region. Values used for the cloudiness fraction are averages taken over three–hour periods and where obtained from the International Satellite Cloud Climatology Project (ISCCP) at the already cited NASA databank.

Short–wave radiation

To calculate the net short–wave radiation (Q_s) entering the ocean the formula proposed by Payne (1972) was used:

$$Q_s = Q_s^o (1 - \alpha_s)(1 - 0.6C^3), \qquad (23)$$

where Q_s^o is the clear sky value for short–wave radiation corrected by atmospheric transmittance usually taken as a constant value of around 0.7. In this work the transmittance was obtained using the first three modes of an EOF decomposition done with over 8 years of satellite data measured in the area (ISCCP), *i.e* a variable

transmittance –ranging from 0.6 to 0.8– for each station was used. α_s is the sea surface albedo calculated by interpolation in the dataset of Payne (1972), where albedo is carefully calculated as a function of the sun altitude and transmittance, and C is the already defined cloudiness fraction.

Buoyancy Flux

Temperature and salinity gradients create fluxes of mass and heat, whose effects on buoyancy are known as buoyancy fluxes. Evaluation of the bulk buoyancy fluxes from meteorological data was done using the formula proposed by Gill (1982)

$$J_b = C_{pw}^{-1} g\alpha Q_T + g\beta s(E - P) \tag{24}$$

where C_{pw} is the specific heat of water at constant pressure, g is the value of gravity, $\alpha = -\rho^{-1}\partial\rho/\partial T$ is the thermal expansion coefficient of seawater, $Q_T = Q_S + Q_B + Q_H + Q_L$ is the total heat flux, $\beta = \rho^{-1}\partial\rho/\partial s$ is the coefficient of saline contraction, s is salinity, E the evaporation rate and P precipitation. The salinity term was not included in the present calculation due to the lack of precipitation data. This is a general practice, justified on the consideration that the contribution of sensible and latent heat fluxes to J_b is much more larger than that of the rest of the terms (Marshall and Schott, 1999). However, Moore *et al.*(1996) proved that in a specific region in the Labrador Sea, precipitation can provide a positive buoyancy as large as the negative buoyancy due to heat fluxes.

Results of the Atlantic Campaign

In Fig. 12 the resulting turbulent fluxes are presented. The upper panel shows the obtained wind stress. Given their definition (see Equation 15), results are inevitably an image of wind velocity magnitude, as can be seen in a comparison with Fig. 10. There are three noticeable events where wind stress have maximum values: first, around 50 °W; second, close to 40 °W; and a wide one between 27.5 °W and 20 °W. These events are also reflected as minimums –maximum ocean heat losses– in the values of sensible and latent heat fluxes (also shown in Fig. 12). Except for the station close to 50 °W, turbulent fluxes of heat are negative. This exception is due to the sea surface being colder than wind temperature and the dominating sensible heat fluxes in that station.
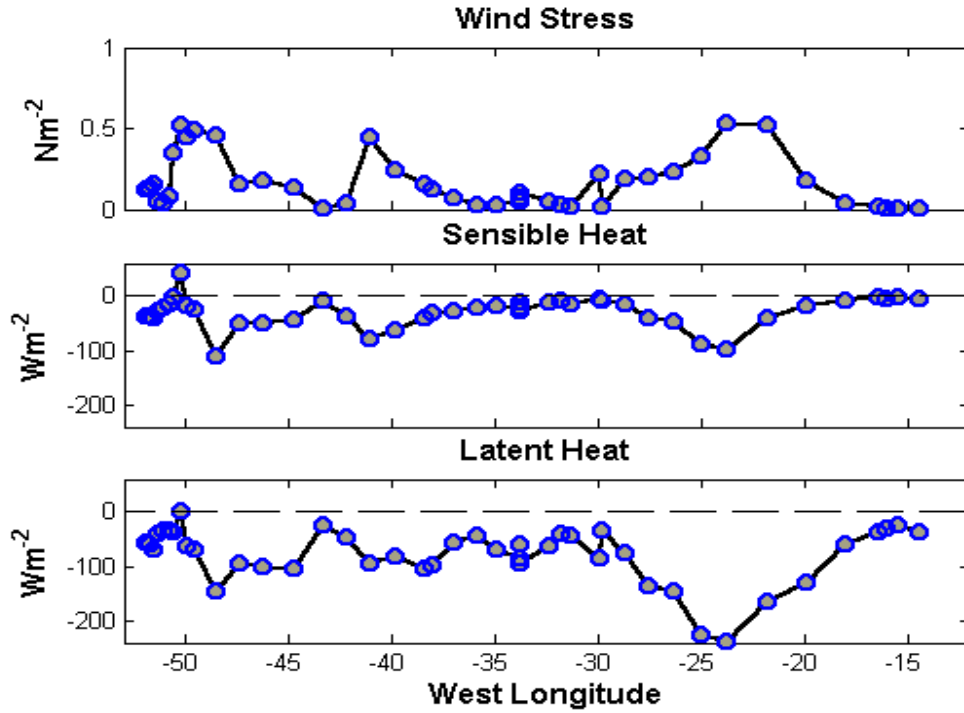
Figure 12. Turbulent fluxes of momentum (wind stress, τ_w) in the upper panel sensible heat (Q_H) in the central panel, and latent heat (Q_L) in the lower panel.

Figure 13 shows plots of various fluxes: in the upper panel long–wave heat fluxes (Q_B) are plotted; the next panel shows plots of short–wave heat fluxes (Q_S); then total heat fluxes are plotted (Q_T); and, finally, the lower panel offers the calculations of buoyancy fluxes (J_b). As can be seen from Equation 22, Q_B depends in a complex way on ocean temperature, air–ocean temperature difference and the amount of clouds, parameterized by the percentage of sky coverage (see Figures 10 and 11). This dependence is reflected in a maximum value associated with the positive difference of air–ocean temperature at $50\,°$W, and a wide minimum corresponding to the region of low cloudiness values; the rest of the stations present an almost constant value of -40Wm^{-2}. Short wave heat fluxes depend mainly on season of the year and the clear sky value (Q_o). This is calculated using astronomic tables and can be considered to be a function of position and time so their variations come from albedo and cloudiness. In the plot of this variable the daily cycle is evident: stations covered at night are those where Q_S is zero, those with values close to
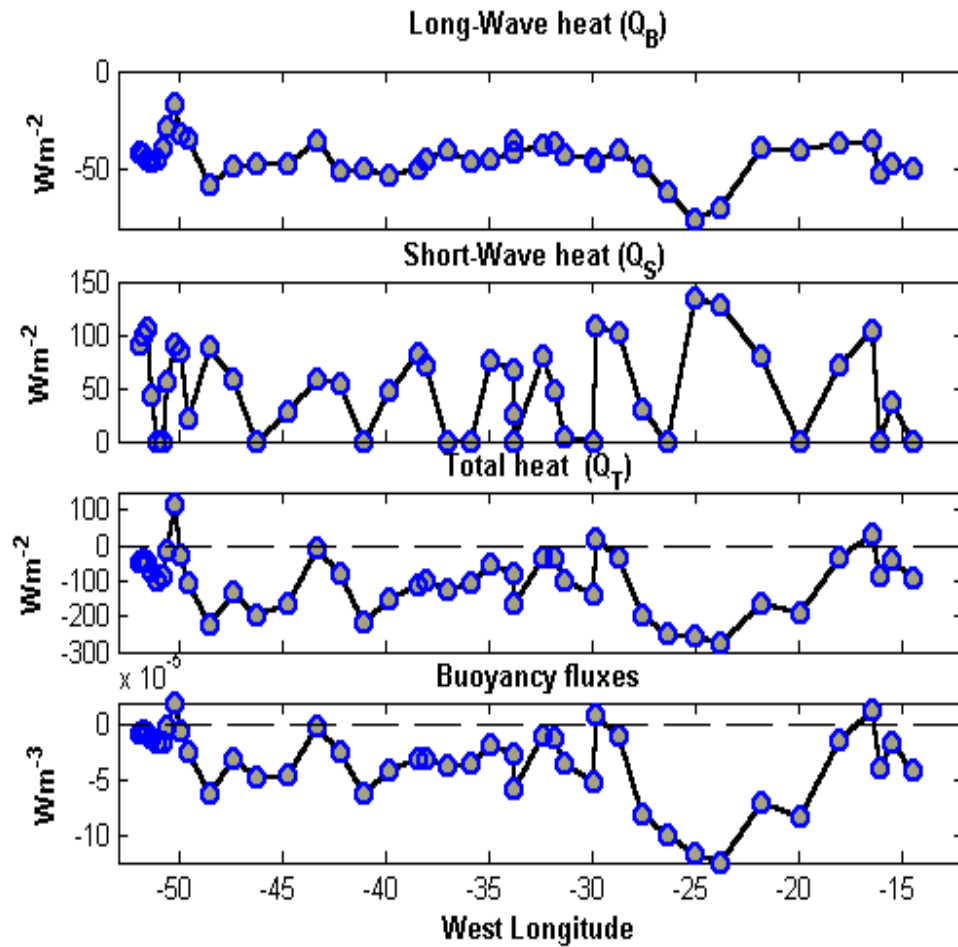
Figure 13. From top to bottom of figure: long–wave heat fluxes (Q_B), short–wave heat fluxes (Q_S), total heat fluxes $(Q_S + Q_H + Q_B + Q_L)$ and buoyancy fluxes (B). See text for explanation.

$100\mathrm{Wm}^{-2}$ correspond closely to local noontime, and those with intermediate values were taken during the morning or the afternoon. For stations west of $30\,°\mathrm{W}$ daily maximums are greater than those corresponding to the rest of the stations, which are connected with regions of minimum cloudiness. Results –which are simply total heat fluxes (Q_T) times a constant– show that with the exception of three points (the first one is linked to the already mentioned station close to $50\,°\mathrm{W}$; for the others there is not any obvious explanation), buoyancy values are negative and variability associated with the daily heating cycle is evident. Explaining that variability in terms of parameters like existing stratification, depth of mixed layer and the rate of

turbulent kinetic energy dissipation is one of the objectives of this work.

Finally, it is important to point out that average values of calculated fluxes generally correspond to those previously reported for the region (Marshall and Schott, 1999; Moore *et al.*, 1996).

4.2.2   General hydrography

The hydrographic transect roughly coincided with the climatological position of the annual–mean zero wind stress curl (WSC), which borders subtropical and subpolar gyres of the North Atlantic (Willebrand 1978, Hellerman and Rosenstein 1983, Ehret and O'Brien 1989). This zone closely corresponds to the northernmost position of the Gulf Stream and then turns to the east following the North Atlantic Current (Marshall *et. al* 2001). North of this line the climatological WSC is positive, thus forcing a cyclonic subpolar ocean gyre. To the south, an anticyclonic subtropical gyre is present, driven by negative WSC. Deviations from these climatological states are most frequently observed during the winter–spring and autumn–winter transitional seasons (Halpern *et al.* 1994). The maps of WSC patterns for the second part of April 2001 are shown at the IFREMER website[4] based on weekly–averaged CERSAT data. During the first week of measurements, the WSC mean field was very patchy, indicating high variability of winds. From 23 April to 29 April, the averaged WSC showed well–defined anticyclonic gyres over the central and eastern part of the transect with typical values of $-2 \times 10^{-7} \, \mathrm{Pam}^{-1}$. These basin–scale variations of the WSC are likely to be responsible for the observed general west to east deepening of the thermocline (see Fig. 14).

To give a general overview of regional hydrography, observed distribution of temperature and salinity from surface to bottom are presented in this section. In the next section discussion is centered on the upper 200 meters, where the main interest of this work is focused. Fig. 14 shows the vertical distribution of temperature along the hydrographic section, while Fig. 15 presents the salinity field. Figures show the typical distribution for the region in the winter to spring transitional period. Next –following the works of Dickson and Brown (1994), Talley (1996) and Worthington

---

[4]http://www.ifremer.fr/cersat/facilities/browse/mwf/qscat_week.htm
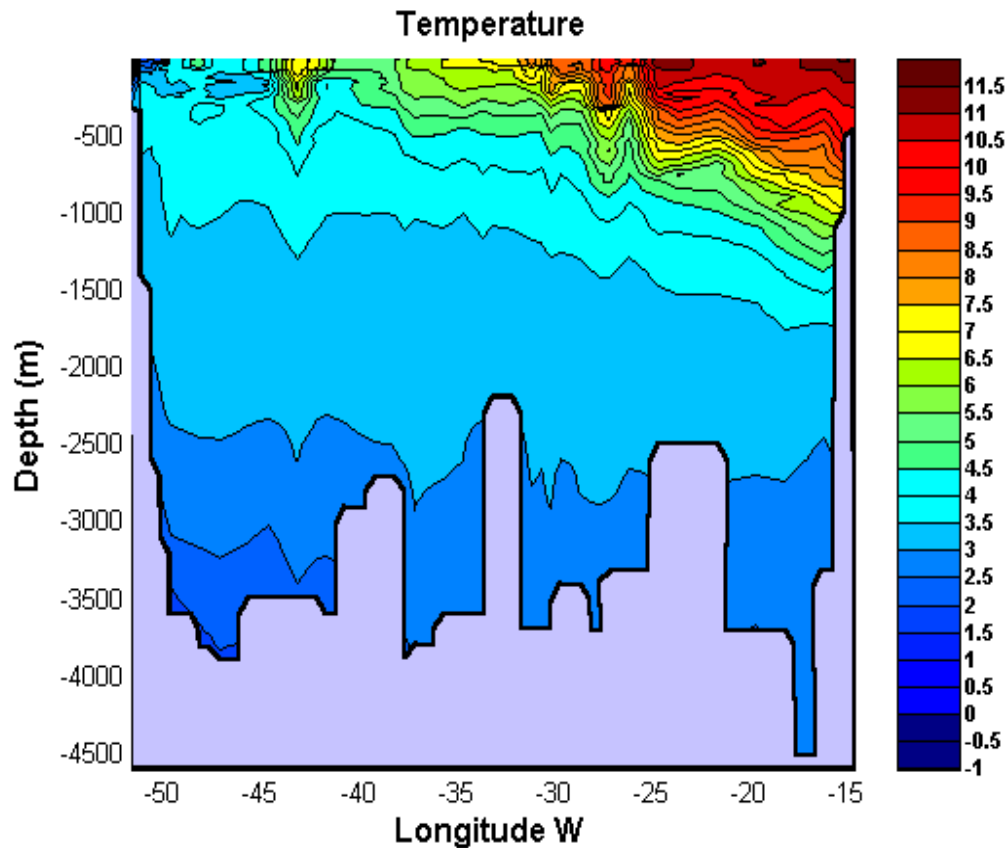
Figure 14. Vertical distribution of temperature along the hydrographic transect. The vertical axis is depth in meters, the horizontal axis is longitude. Temperature is contoured every half degree.

(1981) – the most conspicuous hydrographic features are described.

• **Atlantic Mode Water (AMW):** The core at the east side of the section, delimited by the isotherm of 7.5 °C (Fig. 14) and the isohaline of 34.9 PSU (Fig. 15) is characteristic of Mode Water. This water is created by modification in the vicinity of ocean fronts and is characterized by the presence of minima in their vertical gradients properties. This water is called **Atlantic Water (AW)** when flowing into the arctic domain through the Norwegian Seas.

• **North Atlantic Deep Water (NADW):** This water mass fills the depth range between 1000 and 4000 meters with a layer of relatively high salinity (above 34.8 PSU) and high oxigen content (above 5.5 ml/l) due to its convective origin.
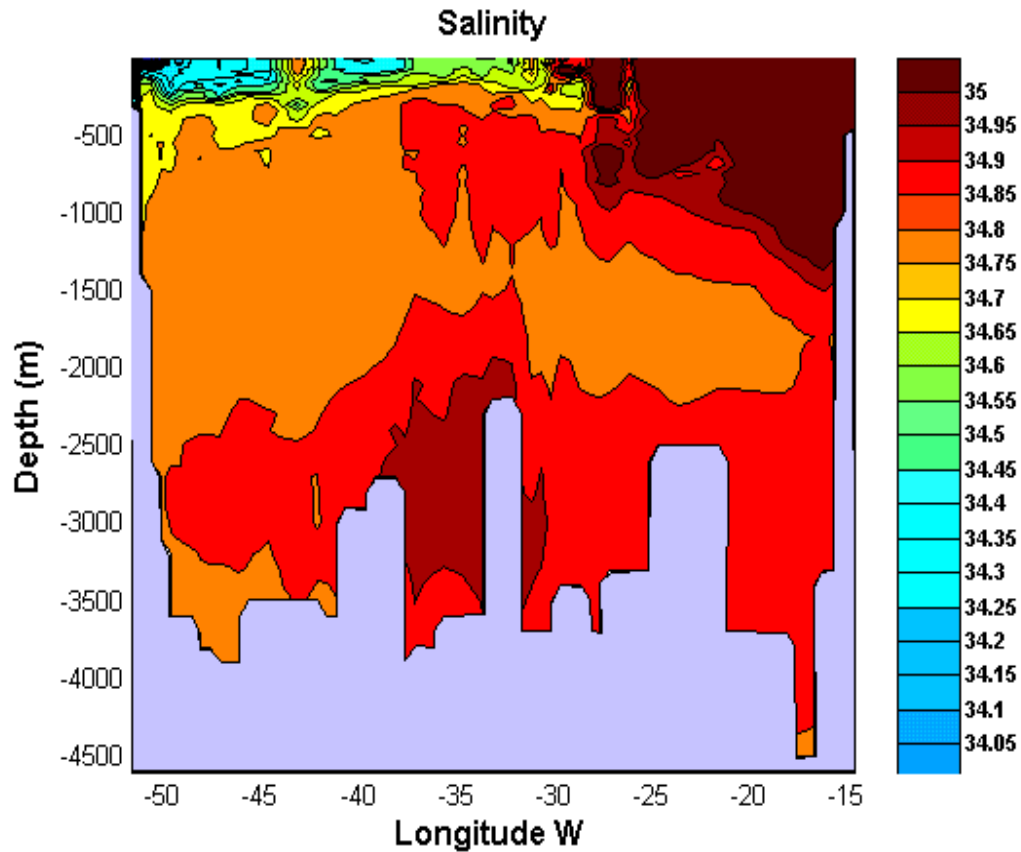
Figure 15. Vertical salinity distribution. The vertical axis is depth in meters, the horizontal axis is longitude. Contours every 0.05 PSU.

- **Labrador Sea Water (LSW):** This water, formed by convection in the Labrador Sea, is the nearly homogeneous volume present at the western side of the section with temperatures ranging between 3 and 3.6 °C and salinities from 34.86 to 34.96 PSU between 500 and 2000 meters where it mixes with **NADW.**

- **Labrador Current:** The cold and fresh water nucleus at the western side between surface and around 400 meters corresponds to the water carried by the Labrador Current. This water presents a temperature and salinity minima close to −2 °C and 33 PSU, respectively. Those values are not evident in temperature and salinity sections due to scale problems.

- **Frontal Structures:** Finally, the region between 40 ° W and 35 ° W grossly limited to the first 500 meters corresponds to the frontal zone where the Gulf Stream

bends west to give way to the North Atlantic Current. This is a zone of intense vertical and horizontal gradients. During almost all of the cruise stormy weather was crossing the section and some of the features present in the data –especially close to the surface– may be due to its influence.
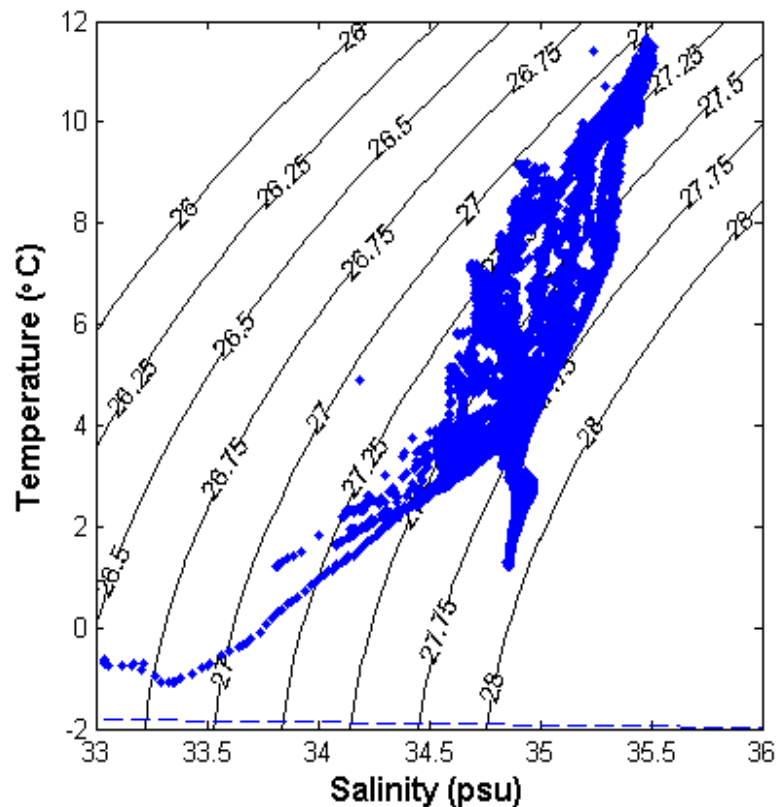
Figure 16. The T–S diagram for the CTD data. The broken line crossing the figure around -2 °C indicates the freezing point for sea–water.

In Fig. 16 the T–S diagram of all of the collected data is shown. In this diagram the characteristic fan–like structure of the upper waters of the North Atlantic Ocean is evident, with low salinity and temperature values at the western side increasing gradually towards the eastern side (see Figures 14 and 15). With increasing depth the water acquires an almost isopycnal character.

4.2.3 Upper 200 meters

Along the transect it is possible to identify two distinct segments in the whole cross–basin section which exhibit different thermohaline structures and flow dynamics in the upper layer. They are presented separately. The first segment is a slanted section covered by 10 stations –from station 917 to 926– between (52.71 °N, 51.87 °W) and (53.52 °N, 49.58 °W). This section is mainly influenced by the cold along–slope flowing of the Labrador Current. Starting from station 926, section becomes approximately zonal and contains 32 deep–ocean CTD stations between (53.60 °N, 48.51 °W) and (51.43 °N, 14.43 °W). This section crosses multiple branches and meanders of the North Atlantic Current.

Slant Section

A general increase with depth of potential temperature (θ), salinity (s) and specific potential density (σ_θ) in the upper 200–meters of the across–slope section is shown in Fig. 17. Contribution of stable salinity gradients to the density stratification prevails over non–stable temperature gradients, ensuring the stable vertical structure of mean density. Mesoscale thermohaline intrusions, which are evident in Fig. 17a and b, do not substantially affect the density spatial structure, *i.e.* they are isopycnal or are close to being so. The only near–surface lens of cooler and fresher water, centered at latitude 50.20 °W, clearly exhibits local baroclinic fronts, which may be associated with a mesoscale eddy meandering in a diameter ∼20 miles. The depth of the upper quasi-homogeneous layer west of 50 °W does not exceed 22 m. At station 925 (53.43 °N, 49.90 °W), the thickness of the upper quasi homogeneous layer sharply increases to 80 m due to preceding wind–induced stormy mixing.

In the thermohalocline, below 50 m, a dome of isopycnal contours (Fig. 17c) can be related to quasi–geostrophic countercurrents that are associated with a large cyclonic eddy (or a meander). These local baroclinic fronts may also represent a branch of the Labrador Current (the southeast up-slope flow west of 51.40 °W) and an oppositely–directed branch of the North Atlantic Current (offshore northwestern flow between 50.50 and 50.20 °W). These currents are well identified at the along– slope section of ADCP velocity shown in Fig. 18b. A boundary between the two is
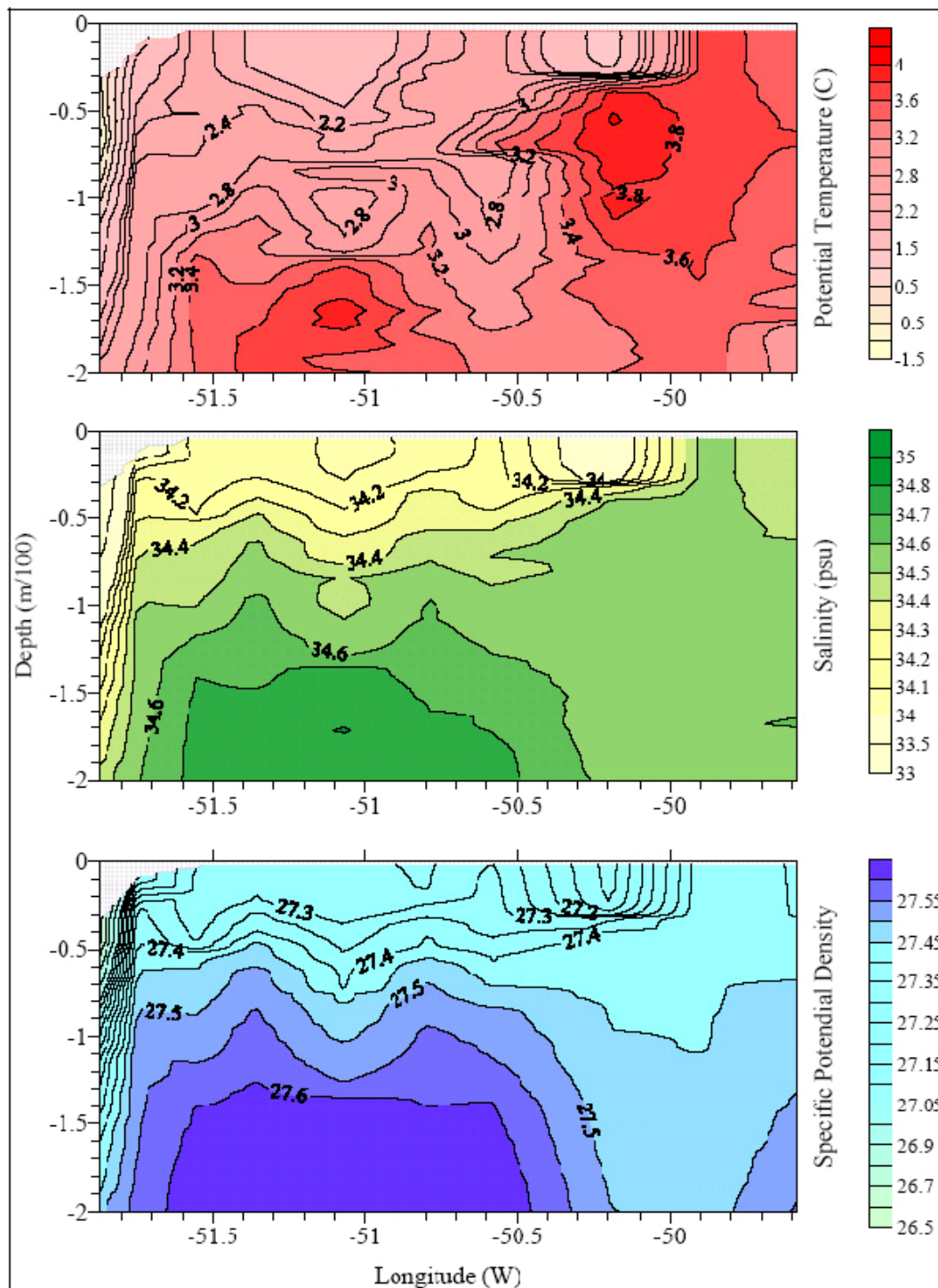
Figure 17. Upper 200–meter of vertical distribution along the slant section transect (Stations 917–926) for: (a) potential temperature, (b) salinity, and (c) potential density.
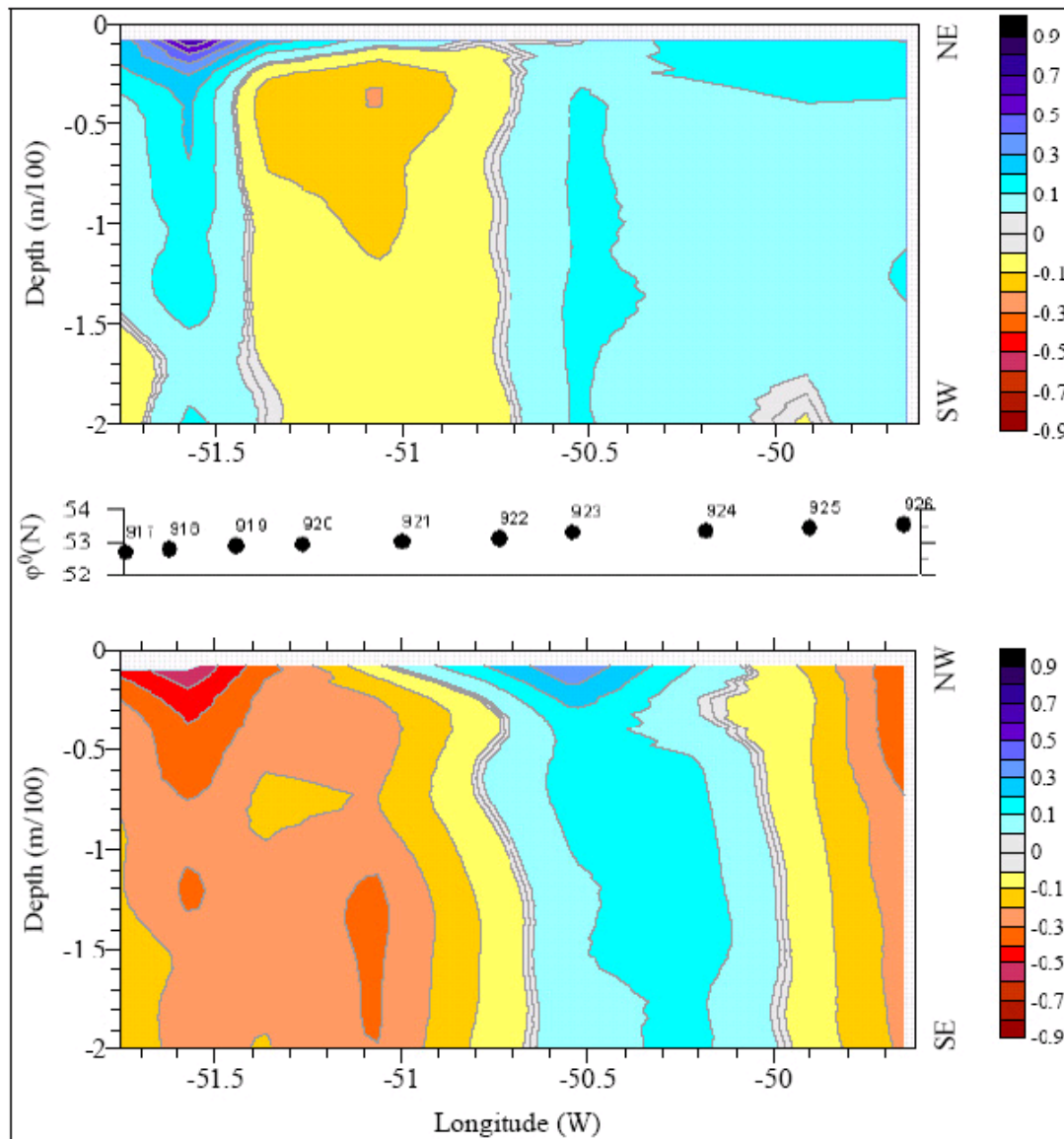
Figure 18. Vertical distribution of ADCP currents (station data only) in the upper 200–meter layer at the Canadian slope section of the transect (Stations 917–926; see middle insert for station position). In the upper panel the across–slope component (u_{sl}) is contoured and directed roughly SW–NE (positive sense). In lower panel it is plotted the along–slope component (v_{sl}) whose positive sense is roughly directed SE-NW. Contours are labeled in ms^{-1}.

evident at 50.65 °W. A map of the geostrophic circulation in the Labrador Sea [Fig. 2 of Lazier and Wright (1993)] shows a narrow northwestern flow penetrating into the main stream of the Labrador Current at 53 °N, 50.5 °W, just in the middle of the slant transect, and then turning to the north and east. Therefore, the observed northern current centered at about 50.3 °W is interpreted as a branch of the warmer North Atlantic Current rather than a section of an eddy or meander of the Labrador Current. This is corroborated by the ADCP data in Fig. 18a, b, where a southeastern flow is seen east of 50 °W, west of which the flow is northward. The Labrador Current extends further to the east up to 48 °W (see the southeastern flow at the left side of ADCP panels, Fig. 18).

Zonal Section

After station 926 the transect meets the North Atlantic Current (Fig. 19). The corresponding contour–plots of θ, s and σ_θ in the upper 200 meters along the zonal section (Stations 926–959) are given in Fig. 20. Temperature and salinity increase continuously in an eastward direction and the density decreases as the transect crosses the Gulf Stream transformed waters. There are, however, two distinct regions at 44 °–45 °W and between 25 °–28 °W with highly alternating horizontal gradients of θ, s, and σ_θ. The first is associated with a warm meander, where the potential temperature at $z = 150$ m is equal to 6.6 °C (Station 931), while it is 3.4 °C thirty miles to the west (Station 930) and 4.1 °C thirty miles to the east (Station 932). The ADCP meridional component in Fig. 19b clearly depicts two counter flows of anticyclonic circulation in this meander. In the second region, a loop of warm–cold meander pair leads to the formation of local frontal zones between Stations 948 and 951. The temperature difference at $z = 200$ m across the eastern front (warm meander) exceeds 2.5 °C, and across the western front (cold meander) it is about 3.5 °C. The internal frontal zone, which separates the cores of the two meanders, is characterized by $\delta\theta > 2.5$ °C at a distance of 40 miles. The basin–scale and large–to–mesoscale variability of the thermohaline and the density structure in the upper 200–meter layer below is mainly governed by geostrophic circulation. Time–space variations of atmospheric forcing determine the ageostrophic dynamics of the upper layer and the synoptic scale variability of the mixed layer depth (see Chap. 5).
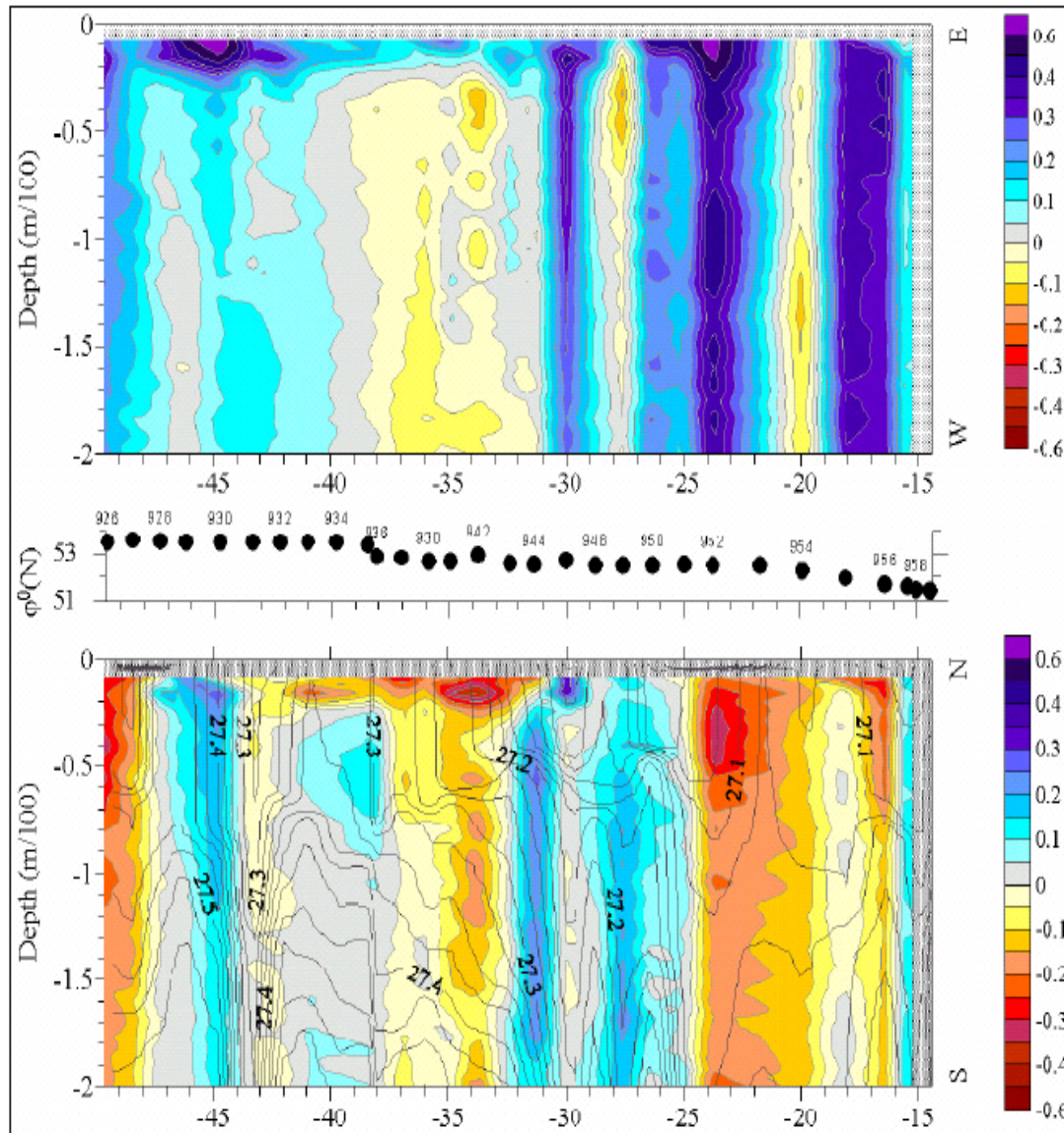
Figure 19. ADCP currents in the upper 200 meter layer along the zonal section of the transect (Station 926 – 959; see middle insert for station position). Upper panel: zonal component; lower panel: meridional component. Colored contours are given in ms^{-1} and line contours included in the lower panel correspond to specific density, included to facilitate the comparison with Figure 20.
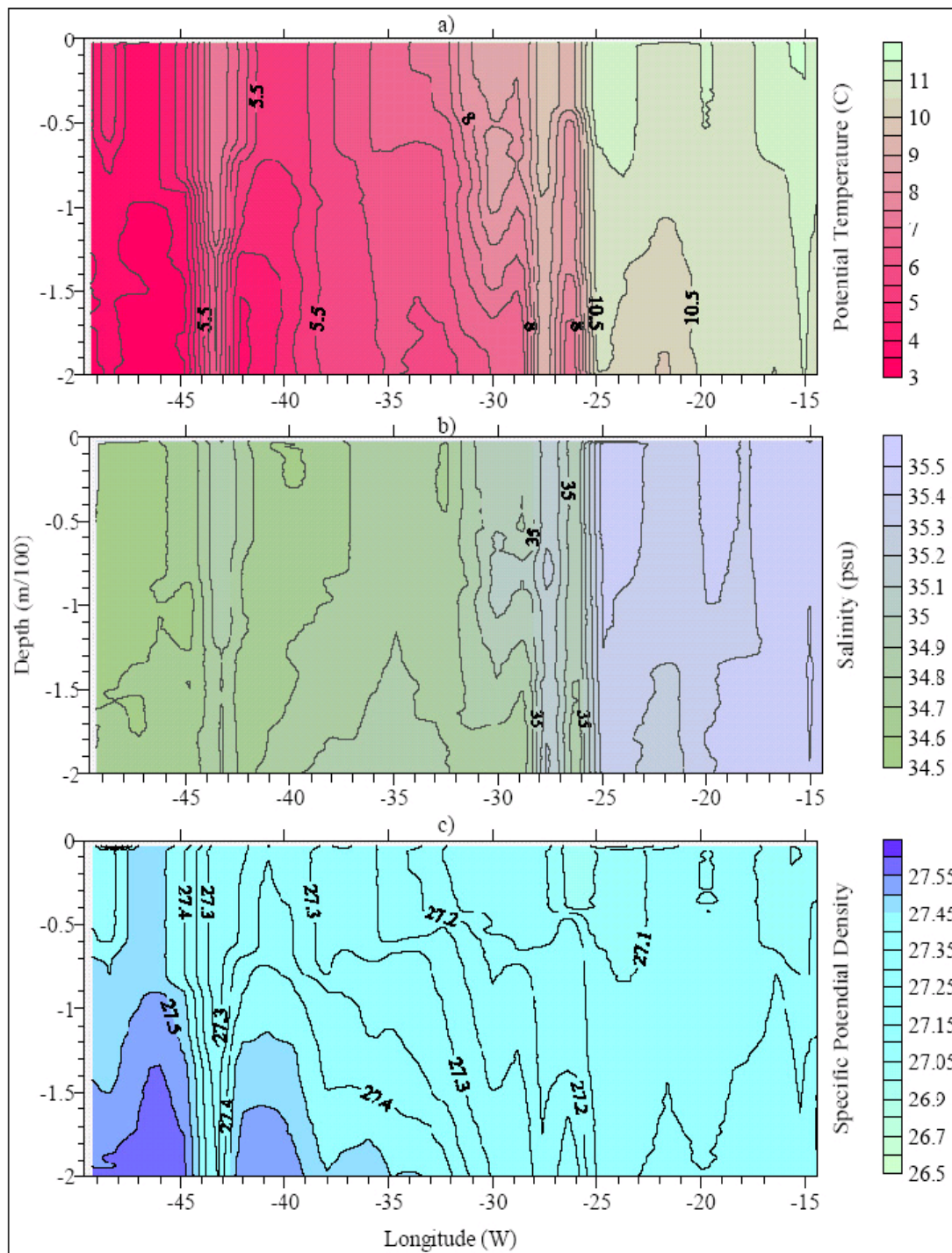
Figure 20. The upper 200-meter layer of potential temperature (a), salinity (b) and potential density (c) contour plots along the zonal trans-Atlantic section (Stations 926 – 959)

4.3 Ageostrophic Currents and Ekman transport

In this section an analysis of the observed current in the upper layer is made. The analysis is carried out following two works, those of Chereskin and Roemmich (1991) and Wijffels *et al.* (1994) [hereafter CR91 and WFB94 respectively] which are among the first to analyze ageostrophic dynamics of the upper oceanic layer using ADCP and CTD measurements in equatorial and tropical regions. The ageostrophic meridional transport across $11.0\,°$N in the Atlantic Ocean was calculated in CR91 and a similar investigation for $10.0\,°$N in the Pacific was made in WFB94. At these latitudes, the inter–annual variability of wind speed is relatively small. However, at $53.0\,°$N, a series of atmospheric cyclones that often cross the Atlantic in early spring significantly influence the upper layer. In Fig. 21 the observed average wind vectors at each station and the calculated Ekman transport vectors are plotted together; stormy periods –though evident in wind magnitude– are indicated in the figure. From the Ekman transport vectors the prevalence of southward and eastward ageostrophic flows in the upper layer during stormy periods is noticeable as is that the direction of the Ekman transport is $90\,°$ to the right of the wind vectors. The transport amplitudes (M_E) have been calculated using

$$M_E = \frac{|\tau_w|}{f\rho_w} \tag{25}$$

where τ_w is wind stress calculated in Section 4.2, ρ_w the sea surface density and the f is the Coriolis parameter. The averaged amplitude of M_E is about $1\ \mathrm{m^2 s^{-1}}$, while the range of highest values –found at Stations 927 and 952– is 3.4–$3.5\ \mathrm{m^2 s^{-1}}$.

Following CR91, geostrophic currents between stations was computed first, then the results, interpolated to the station position, were averaged from ADCP meridional components, assuming that flow maintains a geostrophic balance at a specific depth (z_G) located below the mixed layer depth. The depth assigned by CR91 was $z_G = 250$ m and WFB94 used $z_G = 250$ m. In this work, the computation of ageostrophic velocities (V_{ag}) was done using two reference levels, $z_G = 200$ m and 500 m without any noticeable significant difference; this suggests that the ageostrophic meridional transport across $53\,°$N in the Atlantic is mainly limited to depths below the upper 200–meter layer. If, within the upper layer, V_{ag} represents a wind–driven current component, then the meridional Ekman transport M_{AG} at each
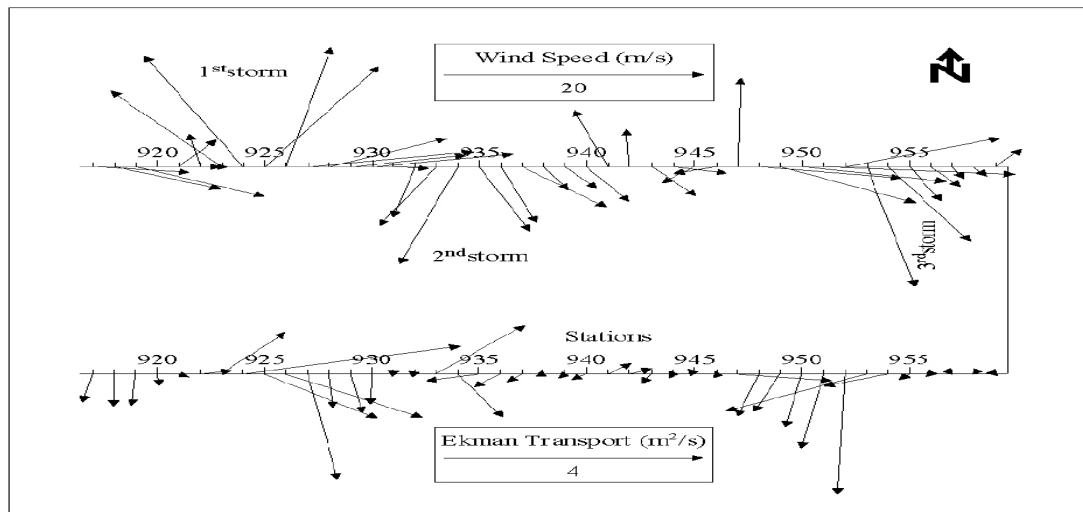
Figure 21. Wind vectors (upper axis) and corresponding estimates of the Ekman transport (lower axis) at hydrographic stations along the whole transect.
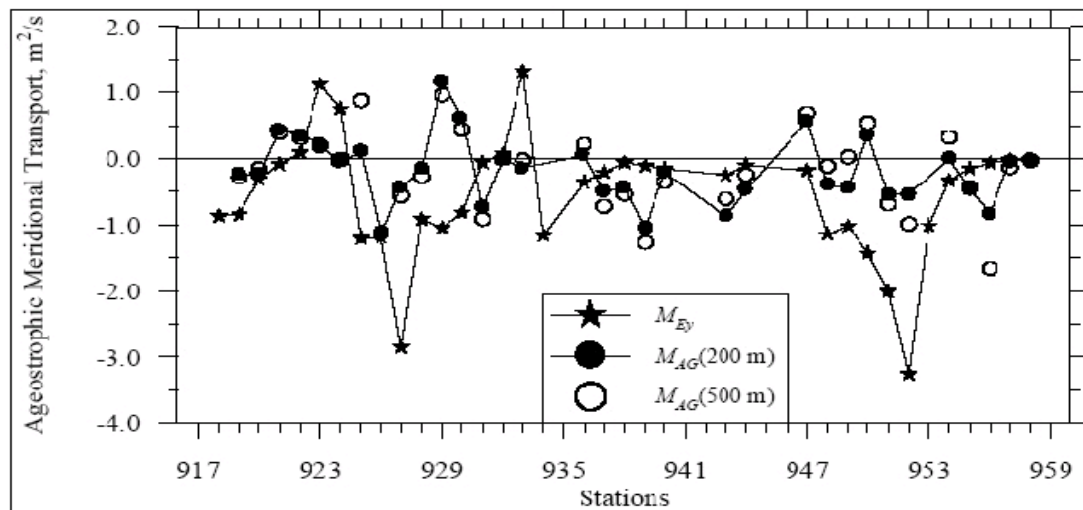
Figure 22. The wind– stress–based Ekman transport (stars) and the MLD ageostrophic transport at 200 m (solid circles) and 500 m (open circles) reference level obtained from ADCP and CTD measurements.

station can be obtained by integrating V_{ag} over the thickness of this layer. Because current measurements obtained by ship–mounted ADCP are noisy in the upper 15–20–meters layer (Pollard and Read 1989), following recommendations of WFB94, V_{ag} was extrapolated from a depth of 16 meters to the sea surface assuming it to be a constant. The estimates of $M_{AG}(200)$, $M_{AG}(500)$ and the meridional component of wind–stress–based transport M_{Ey} are shown in Fig. 22. In high winds, $|M_{Ey}|$exceeds $|M_{AG}|$, which can account for the uncertainty in extrapolation of ADCP data into the upper 16–meter layer. Although a slab–like current structure is often assumed in upper mixed layer models (Price *et al.* 1986), there is a possibility that current amplitudes may increase significantly toward the sea surface, thus requiring aa more accurate extrapolation scheme of $V_{ag}(z)$ than used here. Note CR91, for example, achieved a reasonable correspondence between M_{AG} and M_{Ey} using a linear increase of V_{ag} above $z = 20$ m.

Although M_{AG} along the $53\,°$N transect is usually smaller than the mean values ($\langle M_{Ey}(200) \rangle = -0.18$ m^{2}s^{-1} and $\langle M_{Ey}(200) \rangle = -0.55$ m^{2}s^{-1}), the directions of M_{AG} and M_{Ey} are generally consistent only for transport amplitudes greater than 0.30 m^{2}s^{-1}; only at Stations 929 and 930 was a significant difference observed. In the later case, the southward Ekman transport M_{Ey}, supposedly driven by strong westerly winds, was found to be opposite to the northward ageostrophic transport $M_{AG} \approx 1.0$ m^{2}s^{-1}. This disparity could be attributed to one or more of the following: (i) the incorrect extrapolation of V_{AG} between 0 and 16 m; (ii) the ageostrophic flow not being wind driven and (iii) the penetration depth of the drift current exceeding 200 m, which is, however, very unlikely. At Station 930, a shallow drift current with distinct southward meridional component is able to impede the northward ageostrophic transport, but at St. 929 the meridional component is positive everywhere while decreasing with depth. Therefore, a significant influence of the non–wind–driven ageostrophic component is possible here and the locally observed winds may not be representative of regional–scale drift currents.

Current reversal depth (CRD) was also analyzed. It is defined as the shallowest depth (below $z = 16$ m) where the ADCP current vector changes its direction of rotation. Two examples of ADCP current spirals showing clockwise and counterclockwise rotation of ADCP vector with depth in the upper layer are given in Fig.

23. Clockwise rotation was observed in 19 out of 34 averaged ADCP profiles. The velocity amplitude, however, did not always decrease with depth as it is supposed to do in the Ekman boundary layer, which is bounded below by the geostrophic flow beneath. The rest of profiles with counterclockwise rotation are not consistent with the Ekman drift. Because the ADCP data returns a combination of dynamical components (wind–induced, geostrophic, buoyancy–forced, inertial oscillations, etc.), the Ekman spiral could have been overshadowed by a more powerful process. It is also possible that, at the time of measurements, the drift currents at a number of stations were far from the stationary state required for a well–defined Ekman spiral.
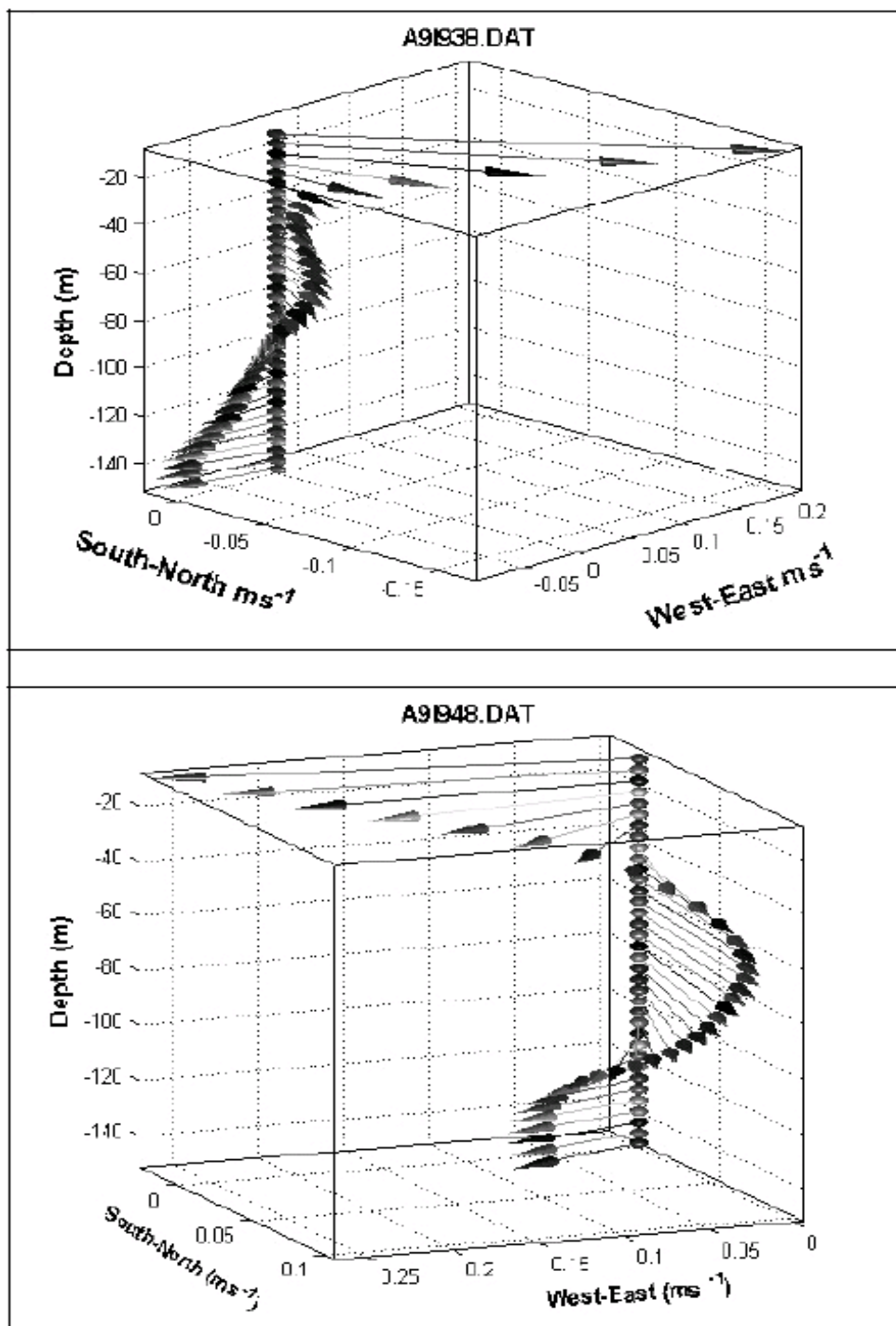
Figure 23. Examples of the ADCP vector spirals showing clockwise (upper panel, Station 938)) and counterclockwise (lower panel, Station 948) rotation in the upper layer.

CHAPTER 5

The mixed layer depth

The upper quasi homogeneous layer (UQHL), as defined in Section 2.2.1, is close to the surface layer where there is little or no variation in density with depth (*i.e.* a quasi homogeneous region). This homogeneity is due to the turbulence generated through the action of surface forcing, like mechanical mixing by wind stress and convective mixing by surface buoyancy fluxes. In general, the UQHL comprehends the zone above the top of the pycnocline up to the surface or to a few (usually around 10) meters from it, depending on the existence or not of the ocean surface layer (OSL), also defined in Section 2.2.1. The UQHL generally shows –in most of the places– a strong diurnal cycle with night time convection due to cooling driving active mixing from the surface to the seasonal pycnocline followed by a shallower daytime restratification due to solar heating (Brainerd and Gregg, 1995). Salinity influence in the mixed layer structure is also important as the formation of strong salinity gradients can lead to mixing suppression. Mechanisms governing the depth and properties of the UQHL are widely discussed in the book by Kantha and Clayson (2000b) and its spatial and monthly global ocean variability is examined by Kara *et al.* (2003).

In many fields of theoretical and applied oceanography –e.g. in global climate change studies– it is necessary to understand, and to predict, how atmospheric and oceanic physical parameters (among other parameters not discussed herein) vary for a wide range of space and time scales. One of the most important of those parameters is the depth (h_D) of UQHL. Over this depth mixed layer properties change with time due to changing air–sea fluxes of heat, freshwater, and momentum. Furthermore, its heat content controls the heat fluxes to the atmosphere, and –as a consequence– the regional climate. In addition, the climatology of the mixed layer is modulated by flux divergence due to ocean currents, vertical mixing and entrainment of water

properties from below. Studies of UQHL variability usually involve an analysis of long–term time series stations at a fixed point –like ocean weather stations– or basin wide (or global) observations covering periods as long as possible.

In this chapter the depth of the upper quasi homogeneous ocean layer h_D and that of the isothermal layer depth are calculated and their correlation is explored. A comparison is also made of h_D values obtained from CTD data and those resulting from microstructure temperature profiles. Later, the structure along the transect of both variables is analyzed and, finally, three scalings of h_D are presented: the Monin–Obukhov length–scale, the Ekman length–scale and the Ekman stratified length–scale.

5.1 Calculation of the mixed layer depth

The depth of the UQHL (h_D) is defined as the first depth –from the surface to bottom of the layer– where the absolute value of the difference between the temperature at that depth $T(h_D)$ and the temperature *near* the sea surface T_w exceeds a prescribed limit δT, that is $\delta T < |T(h_D) - T_w|$. (Note that definition of T_w is places it below of the OSL; do not confuse this temperature with T_s –the SST defined in Section 4.2– which is defined inside the OSL.) According to this definition, the depth of the UQHL is the width of the almost–isothermal layer depth (ILD), usually found at the upper part of the ocean–water column (Kara *et al.*, 2000). When the same approach is applied to density profiles, reference is made to the mixed layer depth (MLD), defined as the depth where the absolute value of density differences $\delta\sigma_\theta = |\sigma_\theta(h_D) - \sigma_{\theta w}|$ is less than a specified value for $\delta\sigma_\theta$. Again, $\sigma_\theta(h_D)$ stands for the density measured at h_D and $\sigma_{\theta w}$ for that measured close to surface. Clearly, this definition of h_D depends heavily on the selected values for δT or $\delta\sigma_\theta$. The reported values in the literature are many: Thompson (1976) and Martin (1985) employed two relatively small values for temperature differences [$\delta T = 0.2$ °C and 0.1 °C] in their studies of UQHL; a much larger one [$\delta T = 0.5$ °C] has been used by Price *et al.* (1986), Kelly and Qiu (1995), Obata *et al.* (1996), and Monterey and Levitus (1997); and Lamb (1984), Wagner (1996) and Qu (2003) selected a larger value [$\delta T = 1.0$ °C]. The most commonly used values for the density difference $\delta\sigma_\theta$ lie in the range $(0.10 - 0.13)$ sigma units [Miller (1976), Levitus (1982), Lewis *et al.* (1990), Spall

(1991), Huang and Russell (1994)]. A tighter limit, $\delta\sigma_\theta$ in the range $(0.01 - 0.03)$, was, however, used in the work of Peters *et al.* (1989), Schneider and Müller (1990), and Padman and Dillon (1991).

Alternatively, MLD or ILD can be identified as the layer where vertical gradients of temperature $\left(\frac{\delta T}{\delta z}\right)$ or vertical gradients of specific density $\left(\frac{\delta\sigma_\theta}{\delta z}\right)$ are smaller than a specific prescribed value. Using these criteria assumes the existence of a sharp transitional region between the UQHL and underlying thermohalocline [Bathen (1972), Lukas and Lindstrom (1991), Richards *et al.* (1995) and Brainerd and Gregg (1995)]. Normally, values for threshold gradients are usually set up in the range $0.02 - 0.05$ $°Cm^{-1}$ for the temperature gradient and 0.01 kgm^{-4} for the specific density gradient. An attempt (Korchashkin, 1976) has also been made to identify layers with constant vertical gradients (used not only to identify the UQHL, but any homogeneous layer in a water column) using difference criteria and gradient limits at the same time. Recently, Kara *et al.* (2000) introduced an optimal algorithm for ILD and MLD calculation using a temperature difference criterion. δT and corresponding $\delta\sigma_\theta$ but with an additional requirement: that adjacent temperature (or density) values at consecutive depths must differ by less than $0.1\delta T$ and $0.1\delta\sigma_\theta$.

It should be noted that the use of an objective criterion to calculate the MLD quite often leads to an erroneous outcome, especially if data set being analyzed is significantly heterogeneous (see the discussion in Brainerd and Gregg, 1995). A mix of profiles with sharp and weak pycnoclines underlying the MLD creates a problem when using a unique δT or $\delta\sigma_\theta$ for MLD identification. Therefore, if a specific limited set of data is analyzed, it is useful to verify the results of any automatic MLD processing by visually checking and making any necessary manual corrections. In this work, the analysis of temperature and density profiles obtained with CTD and MSS was done implementing the latest approach and using δT and equivalent $\delta\sigma_\theta$ criteria as initial guidelines, but the final judgment was subjective.

The MLD was calculated using variations of potential density of $\delta\sigma_\theta = 0.02$ as approaching criteria and further visual correction was only applied to four of the CTD profiles. Estimation of the ILD was done using the algorithm of Kara *et al.* (2000) on the same set of CTD profiles but varying δT in the range $0.10 - 0.30$ $°C$ with 0.05 $°C$ increments. Then, results were explored for the best correspondence between the two
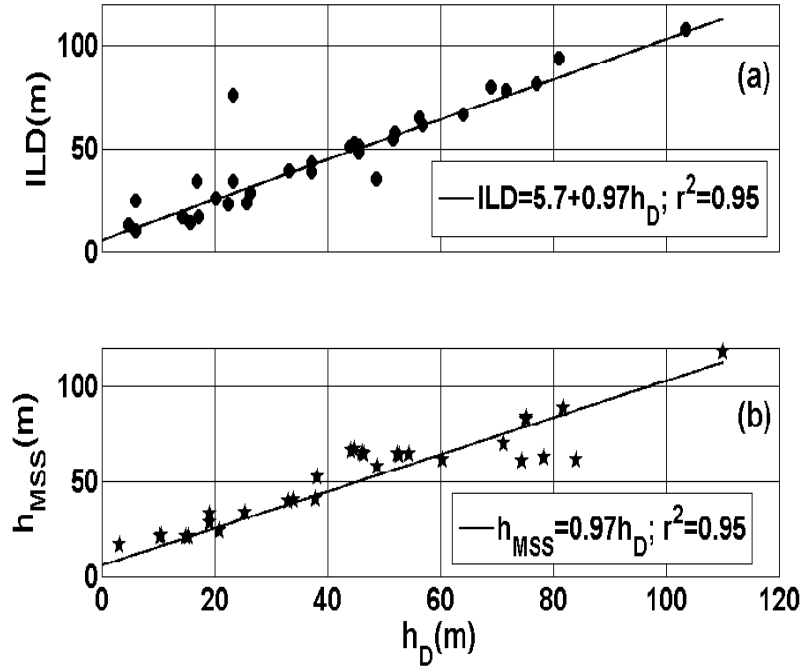
Figure 24. A comparison between: **(a)** the depth of the isothermal upper layer, calculated using the Kara *et al.* (2000) algorithm with $\Delta z = 2$ m and $\Delta T = 0.25\,°$C (ILD) and h_D determined with the difference criteria $\delta\sigma_\theta = 0.02$ sigma units and subjective correction. **(b)** The MLD estimates obtained from NB (h_D) and MSS (h_{MSS}) profiles at the stations where both instruments worked in parallel.

methods, which was obtaining it for $\delta T = 0.25$ °C without any vertical averaging or interpolation. Fig. 24a shows the linear regression between the MLD (labeled h_D) and the best correlated ILD (the regression was obtained using only those profiles with the MLD being greater than six meters and excluding station 934, an obviously wild datum). Results [$ILD = 5.7 + 0.97 * h_D$, with a coefficient of determination $r^2 = 0.95$] indicates that automatically calculated (temperature–based) depths of the UQHL are about 5 m larger than those obtained from potential density criteria; however, both methods fairly consistent outcomes. [In forthcoming analyses only the obtained MLD estimates are used because they permits a more accurate identification of a transition region between the mixed layer and the thermohalocline]. The MLD obtained from the CTD data was also compared with the depth obtained using the same procedure but with the MSS data set. The correlation is shown in Figure 24b,

where the CTD–obtained MLD is labeled h_D and the MLD calculated from the MSS data is labeled h_{MSS}. The correlation between both estimations of the MLD is very high [$h_{MSS} = 0.99 * h_D$, with a coefficient of determination $r^2 = 0.95$]. Any observed scatter may be attributed to up–to–1 hour time shift between NB and MSS casts.

5.2   The variation of h_D along the transect

The along–transect variation of both of the estimations of the mixed layer depth MLD is shown in Fig. 25. In that figure –as in Fig. 24– it can be seen that h_{MSS} obtained from a free falling profiler is usually slightly deeper than h_D obtained with the NB–CTD data. In the last case, the mean $\langle h_D \rangle = 44.5$ m, the median(h_D) = 48 m, rms(h_D) = 25.2 m and the observed mixed layer depth varies in the range of 6–110 m; the deepest being at station 931 and shallowest at 924.

Comparing MLD basic statistics with those of the current reversal depth (CRD) [see Section 4.3], it appears that $\langle CRD \rangle = 46.9$ m and median(CRD) = 48 m are almost the same as the mean and the median of the MLD given above. This may indicate that the mixed layer depth coincides, on average, with the depth penetrated by the drift currents. The correspondence becomes clearer, if it is compared the mean difference between CRD and MLD are compared separately for clockwise and counterclockwise profiles using 2–meter interpolated ADCP data. For the first group (19 stations), the mean MLD CRD difference - is only 2 m, while for the second group it difference is 7.2 m; therefore, the mesoscale spatio–temporal variations of the MLD and the CRD along the transect are broadly consistent. Also note that because of the time shift between NB and ADCP profiles, the differences between observations at individual stations could be due to internal wave displacements and/or horizontal gradients.

Three shaded rectangles shown in Fig. 25 point to regions with notice-able increases of MLD ($h_D > 50$ m) and associated with periods of strong wind ($W > 10$ ms^{-1}) –indicated by hatched rectangles at upper part of the same figure– which precede the enhancing of mixed–layer deepening. The magnitude of out–of–the–ocean heat flux also increases with higher winds (see Fig. 12), ensuring a larger buoyancy flux (J_b) into the ocean. To quantify the relationship between atmospheric
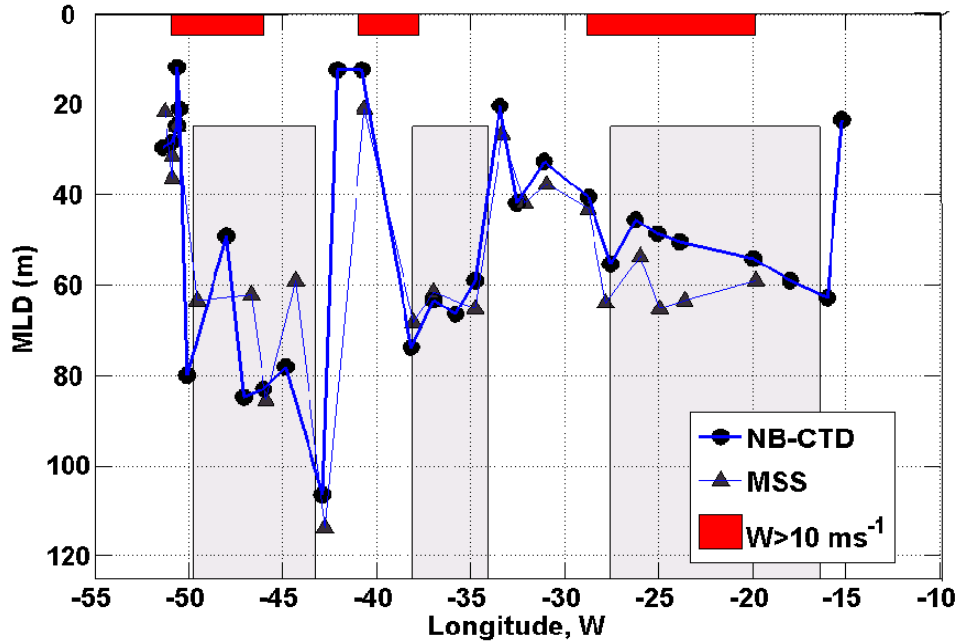
Figure 25. The mixed layer depth (MLD) obtained from NB–CTD (dots) and MSS (triangles) density profiles. Three periods with winds exceeding 10 ms^{-1} are marked along the upper axis. The sections with increase of MLD (shadowed areas) exhibit a space–time shift (delay) in relation to the segments of stormy winds. The time shift, up to 1 hour, between NB and MSS casts is attributed, in part, to the observed differences between the MLD obtained with NB-CTD and the MSS data at several stations.

forcing and the MLD, the normalized cross–correlations function of h_D and u_* [denoted by $R_{hu_*}(\Delta t)$] and for h_D and buoyancy flux J_b [denoted by $R_{hJ_b}(\Delta t)$] were calculated, where Δt is the corresponding time lag. To calculate cross–correlation functions, the MLD and fluxes were interpolated to produce equally–spaced time records through the linear interpolation of measurements at each station. The time step $\Delta t = 6$ hrs. was chosen for the interpolated records, because approximately 12 days of observations provided 49 interpolation points, while the measurements were taken at 42 time locations (stations). Arranging the data for the correlation analysis as a time series, not as space variables, is based on the assumption that the main cause of the mixed layer deepening and restratification is associated with synoptic scale variations of u_* and J_b driven by storm events. Horizontal scales of the regions

where the MLD exceeds 50 m are 250–350 km, wich is consistent with the scales of atmospheric cyclones at these latitudes.
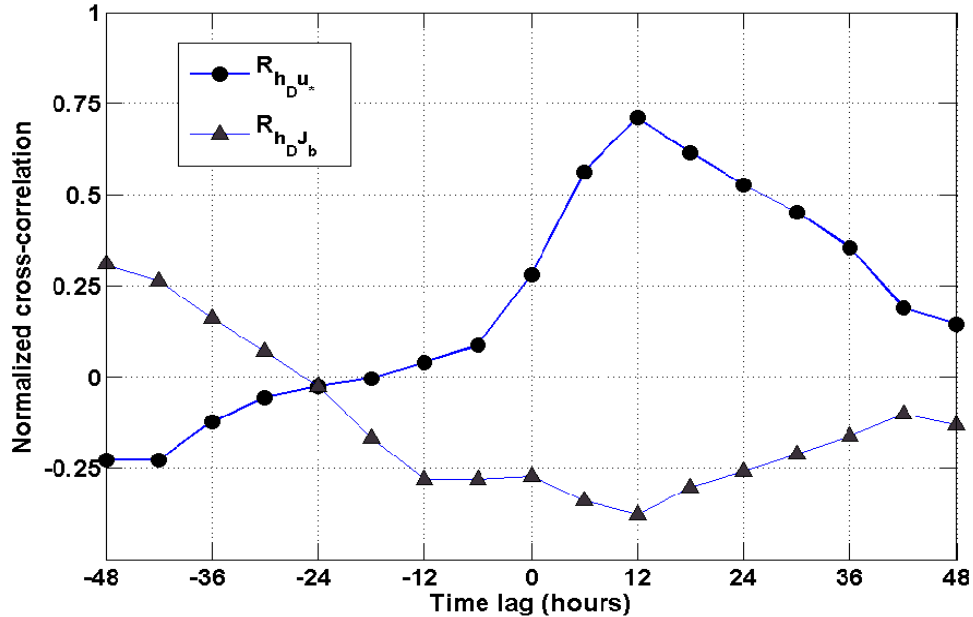
Figure 26. Normalized cross–correlation functions between the mixed-layer depth h_D and friction velocity u_* (dots), and between h_D and the buoyancy flux $-J_b$ (triangles).

The correlation $[R_{hu_*}(\Delta t)]$ between h_D and friction velocity u_* exhibits (Fig. 26) a statistically confident maximum of 0.71 at the time shift $\Delta t = 12$ hrs. While $[R_{hJ_b}(\Delta t)]$, the correlation of h_D and J_b have a maximum value of 0.40 at $\Delta t = 0$ and it is lower elsewhere. Because the 95% confidence level for non–zero correlation is 0.34, then $R_{hJ_b}(\Delta t)$ is considered insignificant at all Δt but $R_{hu_*}(\Delta t)$ is not. These results indicate that the deepening of the mixed layer during measurements was mainly governed by wind stress, the influence of buoyancy flux being of lesser importance. It is possible that the observed time lag is associated with the spin–up time of inertial oscillations, which enhance shear and thus vertical mixing at the base of the mixed layer [see e.g. Pollard et al. (1973)]. A similar result has been reported by Lentz (1992a) for coastal upwelling waters, with the time shift ranging from 5–6 to 10–12 hrs. The results shown here also suggests that winds associated with spring storms in the North Atlantic have to work for about 12 hours in order to effectively

erode the existing stratification, entrain water from the underlying pycnocline, and develop a UQHL with a mean thickness of $\sim$45 m. The above interpretation assumes that the measurements of the MLD represent a quasi–stationary state of the mixed layer. At some stations, especially those where data were taken in the beginning of stormy events, it is definitely not true. Much shorter time is needed, however, for the upper–layer turbulence to respond to rapidly increasing winds [see, for example, Anis and Moum, 1995; Roget *et al.*, 2004]. Finally, turbulence decays quickly when atmospheric boundary forcing ceases and perhaps the obtained correlations are explained by the fact that sampling at most of the stations was done just after the passing of a stormy weather system.

5.3   Scaling of h_D

In this section the MLD is scaled with three different length scales typically used in the analysis of the upper ocean dynamics: the Monin–Obukhov length, the Ekman length–scale and the Ekman stratified length–scale. From these, ideas about the mixing forces and the state of MLD are derived.

5.3.1   Using the Monin–Obukhov length

The Monin–Obukhov (1954) scale defined as $L_{MO} = u_*^3/\kappa J_b$, where $\kappa = 0.40$ is the von Karman constant, determines when the buoyancy production (free convection) dominates over shear production (forced convection). The dependence –with the time record of u_* shifted ahead by $\Delta t = 12$ hrs– between the MLD and the length of Monin–Obukhov (henceforth, LMO) is shown in Fig. 27 with crossed square symbols. The same figure also shows, with a thick continuous line, the power approximation $h_D \sim L_{MO}^{1/3}$ indicating a linear dependence between the MLD and friction velocity. Notice the logarithmic scale used in the horizontal axis. The dependence on the buoyancy flux J_b is weak ($r^2 = 0.58$). Following Lombardo and Gregg (1989), two lines are also shown: $h_d/L_{MO} = 1$, labeled (i) and with a discontinuous, thin trace, and $h_d/L_{MO} = 10$, labeled (ii) and also with a discontinuous, but thick trace. These two lines bound the range of h_D where the wind stress and buoyancy flux play comparable role in the development of the mixed layer. For $h_d/L_{MO} > 10$ (to the left
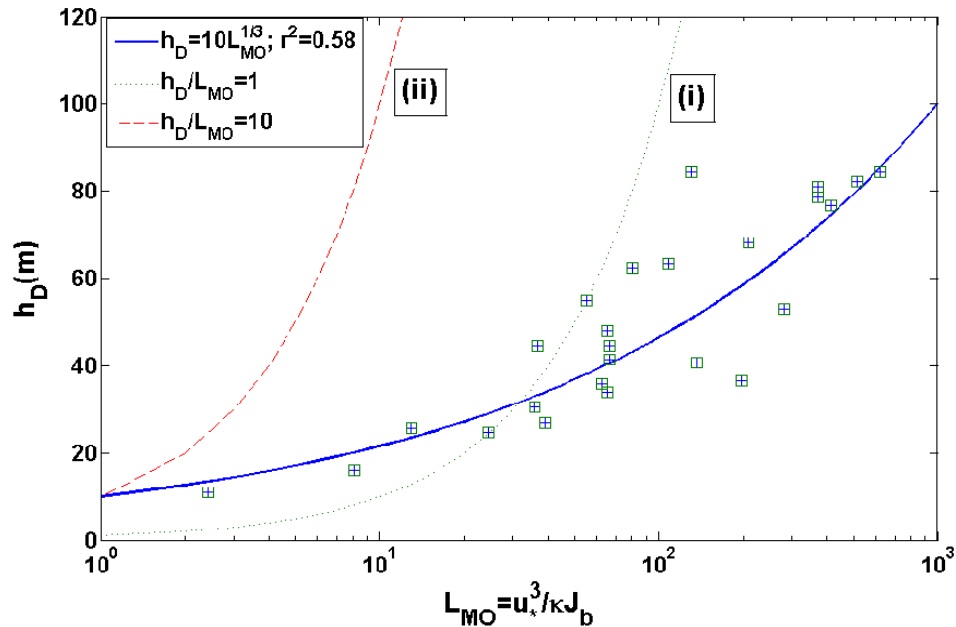
Figure 27. Regressions between the mixed layer depth h_D and Monin-Obukhov scale L_{MO} at Stations 926–954, with the friction velocity u_* shifted in time by 12 hrs. The buoyancy flux J_b calculated at the time of the MLD measurements is the shown. The power trend of h_D growth with the increase of L_{MO} is obtained by a least squared fitting. Line (i) corresponds to $h_D/L_{MO} = 1$; line (ii) gives $h_D/L_{MO} = 10$.

from (ii) line) convection is a dominant force, but for $h_d/L_{MO} < 1$ (to the right from (i) line) the wind stress is the prevailing factor. In Fig. 27 it can also be seen that there are only three stations where the contributions of wind stress and buoyancy flux in shaping the mixed layer depth are comparable. The vast majority of points lie below the $h_D/L_{MO} = 1$ line indicating that, in the region, spring season convection is less important in maintaining the mixed layer depth than wind–induced mixing.

5.3.2   Using the Ekman length–scale

Given the linear dependence of h_D on u_*, it is possible to surmise that the Ekman length–scale, defined as $L_f = u_*/f$, is a better candidate to scale the MLD than Monin–Obukhov length. As shown in Fig. 26 by their correlation, the average response of h_D is delayed by about 12 hrs. from the change of friction velocity, so the regression of h_D and L_f is plotted shifting the records by $\Delta t = 12$ hrs.

Dependence between L_f and shifted in time (space) h_D, as shown in Fig. 28a, is reasonably well approximated by the linear function $h_d = 0.44L_f$ with the coefficient of determination $r^2 = 0.92$. However, this correlation does not hold when the time shift is not used, as can be seen in Fig. 28b. This may be one of the reasons why data in Fig. 28 show a relatively wide scatter around a linear trend. This scatter may be explained by an non stationary state of the UQHL in those stations covered at the beginning of a storm.

5.3.3 Using the stratified Ekman length–scale

The mixed layer results can also be interpreted on the premise that upon introduction of a wind stress, the UQHL deepens until the MLD reaches $L_{fN} = u_*/\sqrt{fN_{pc}}$, where N_{pc} is the buoyancy frequency at the upper boundary of the pycnocline (obtained by a linear fit to the density profiles over the first 10–15 m below the UQHL). As pointed out by Pollard *et al.* (1973), the subsequent growth is slow. Therefore L_{fN} can be a good indicator of the MLD after a storm. Scaling of the MLD by L_{fN} (Pollard *et al.* 1973) has been explored by Weatherly and Martin (1978) and Lentz (1992b) for the bottom boundary layer and by Zilitinkevich and Esau (2002) for the atmospheric boundary layer. Figure 29 shows a plot of h_D versus L_{fN} with u_* shifted ahead in calculating L_{fN}. The goodness of the linear fit in Fig. 29 ($r^2 = 0.9$) is slightly lower than that in Fig. 29a, but this difference is statistically insignificant. A relatively wider scatter in Fig. 29 may indicate that N_{pc} is either calculated with a higher uncertainty (because of highly non–linear density profile in the pycnocline) or it does not significantly influence the MLD at later stages of the mixed–layer deepening. The regression in Fig. 29 shows that, on the average, the ratio $h_d/L_{fN} \approx 1.9$. Values of the same ratio reported by Pollard *et al.* (1973) and by Weatherly and Martin (1978) are 1.7 and 1.3, respectively. Various one–dimensional models of thermocline formation (Niiler and Kraus (1977), Price *et al.* (1986), Lozovatsky *et al.* (1998), and others) suggest that the ratio h_d/L_{fN} tends to reach 1.7 at large times of numerical calculations.
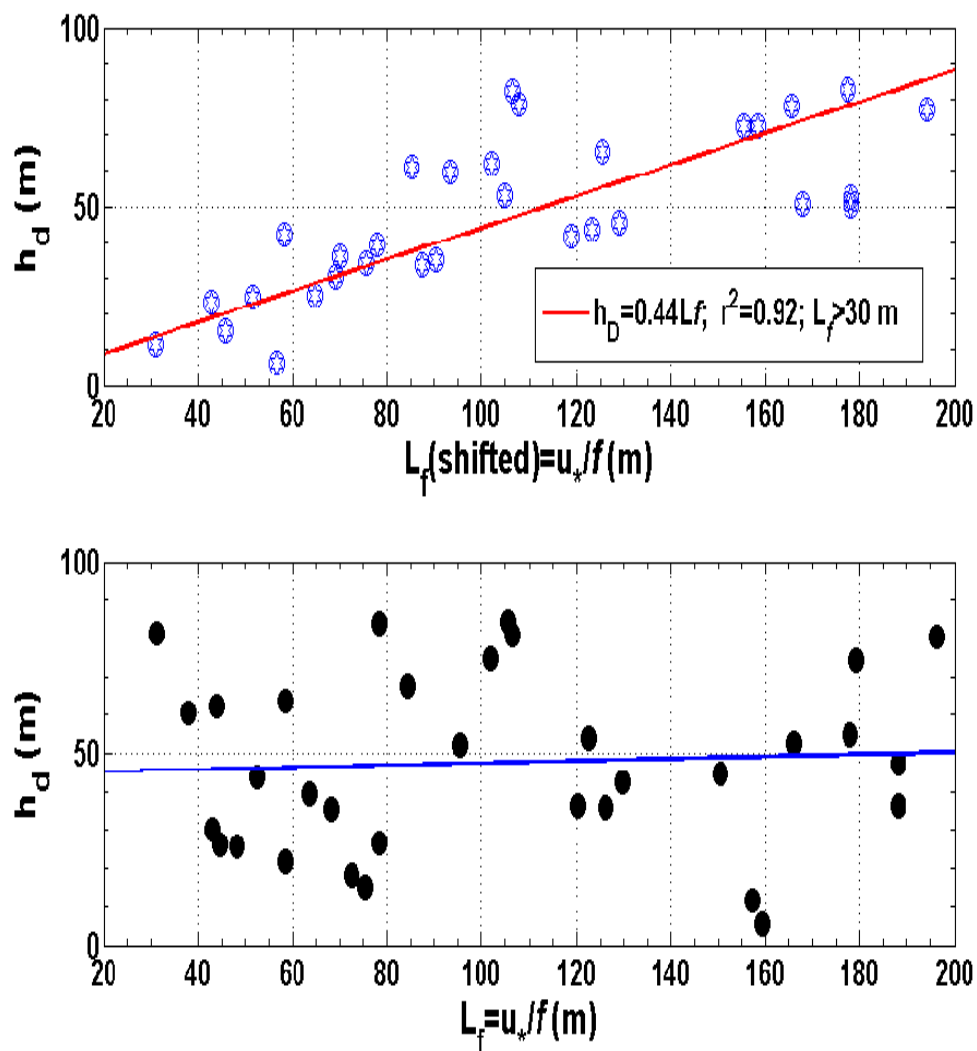
Figure 28. Regressions between the mixed layer depth h_D and the 12–hour forward shifted Ekman scale L_f (a). The same variables without time shift (b). A linear growth of h_D with L_f (for $L_f > 30$m), which is seen in the upper panel, vanishes in the lower panel.
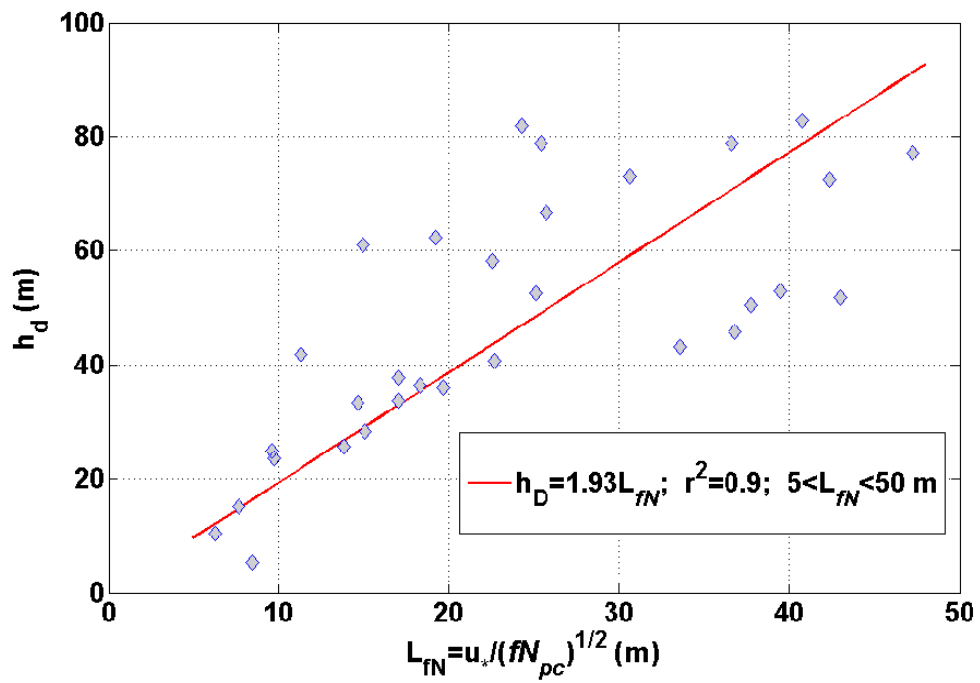
Figure 29. Scaling of mixed layer depth h_D by using the stratified Ekman lengthscale $L_{fN} = u_*/\sqrt{fN_{pc}}$. The estimates of friction velocity u_* are shifted ahead in time by 12 hrs in the L_{fN} calculation.

Turbulence within the MLD

In this chapter an analysis of the obtained KEDR values is presented. The first section analyzes the vertical structure of the dissipation rate: first its dependence on the vertical coordinate (z) explored, then different parameterizations of ϵ in terms of the atmospheric forcing are explored and discussed. In the next section a comparison between mixed and mixing layer depths is made; then an analysis of the statistical distribution of ϵ, R_i and R_b is presented. In the following section the dependence of diffusivity $K_b(R_i)$ on the Richardson number is explored by testing two parameterizations, both in the spirit of the classic work of Munk and Anderson (1948), ending with a mixing scheme proposal. Finally, a comparison is made between the work exerted by the wind (E_{10}) at the ocean–surface and an estimation of the column–integrated dissipation (over the mixing depth) obtained by doing an extrapolation of the best–fitting model to the observational values of ϵ to near–surface level where data are not available.

6.1 Vertical structure of the dissipation rate

This section shows the vertical structure of measured ϵ. First the z dependence of KEDR is explored using an exponential type function for data above the level $z_{cw} = 16$ m (more on this follows), and two inverse power type functions for data below z_{cw}. After this, dependence of ϵ on meteorological forcing is analyzed testing four different parameterizations.

6.1.1 The ϵ dependence on z

A composite plot of individual 1–meter averaged kinetic energy dissipation rate (ϵ) samples (the total number of samples is 2487) taken from the mixed layer at all

of the stations is given in Fig. 30, where the depth–sorted, bin–median estimates of the dissipation $\widehat{\epsilon}(z)$ (100 samples in each bin) are also shown with large filled circles. Two regimes can be easily identified: the first one is defined by a sharp decrease of the bin–median dissipation $\widehat{\epsilon}(z)$ [from 10^{-2} to around $10^{-6.5}$ Wkg^{-1}] within the depth range $z < z_{cw}$, where $z_{cw} = 16$ m was selected through a careful inspection of data and considering the calculation of two empirical fits to be presented next; the second regime is characterized by a much slower decline of $\widehat{\epsilon}(z)$ [from around $10^{-6.5}$ to 10^{-8} Wkg^{-1} or less] in the depth range $z_{cw} < z < h_D$. The least–squared approximations, which were separately calculated for these two sections give the following equations:

$$\widehat{\epsilon}(z) = 1.84 \times 10^{-1} \exp(-0.85z) \text{ for } z < 16 \text{ m} \tag{26}$$

and

$$\widehat{\epsilon}(z) = 1.05 \times 10^{-5} z^{-1.2} \text{ for } z > 16 \text{ m}, \tag{27}$$

respectively. Turbulence in the near–surface layer, $z < z_{cw}$, is significantly affected by surface waves, and the observed exponential decrease of $\widehat{\epsilon}$ with depth generally supports the wave–induced scaling for dissipation like that proposed by Anis and Moum (1995). However, because a falling, not a rising, profiler was used for ϵ measurements in the near–surface layer, data could have been contaminated by the instrument's unsteady falling speed, occasional cable tension, and ship rolling. This kind of contamination can not be filtered out [as discussed in Chapter 3], therefore, this study excludes the depth range $z < z_{cw} = 16$ meters.

Formal power–law fitting given above for $z > z_{cw}$ can also be satisfactorily represented by an inverse power function $\widehat{\epsilon}(z) = 0.75 \times 10^{-5} z^{-1}$, in the spirit of well–known "law of the wall"

$$\epsilon_1 (z) = \frac{u_*^3}{\kappa} z^{-1} \tag{28}$$

which has been used in several studies to represent the dissipation profile in the surface layer [i.e, Dillon et al., 1981; Soloviev et al., 1988]. Despite the bin–median estimates of $\widehat{\epsilon}(z)$ shown in Fig. 30, roughly following Eq. 28, it should be noted that the law of the wall can only be used as a zero order model for $\widehat{\epsilon}(z)$, because the influence of the surface buoyancy flux is not considered in this equation. This is done in following section.
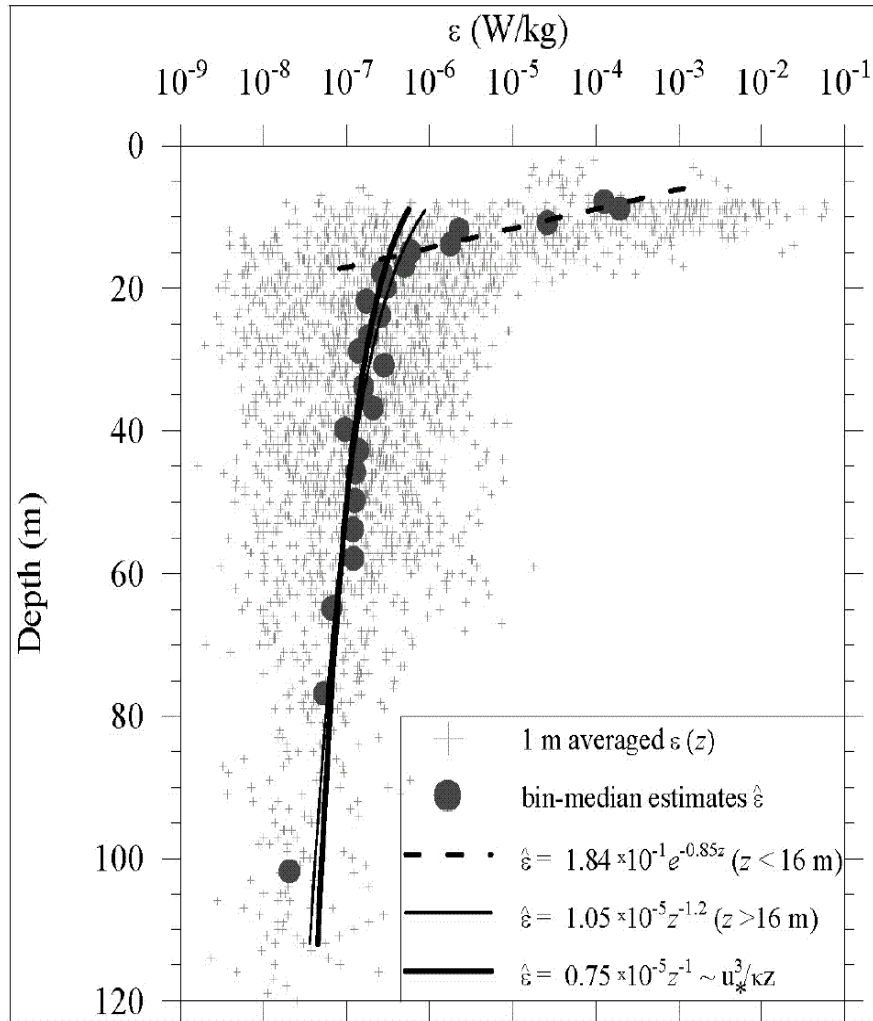
Figure 30. The kinetic energy dissipation rate in the upper turbulent layer at all measurement stations (2487 samples) is indicated by small plus symbols. The depth–sorted, bin–median estimates of the dissipation (100 samples in each bin) $\widehat{\epsilon}$ is shown by solid circles. The best least–squared approximations (exponential: dashed line; power: thin solid line) are given for two sections of the $\widehat{\epsilon}(z)$ profile, 2 m $< z <$ 16 m and 16 m$< z < h_D$, respectively. The thick solid line shows "law of the wall" fitting.

6.1.2 Parameterization of $\langle \epsilon(z) \rangle$ based on meteorological forcing

With the exception of Eq. 28, fitting functions like those previously exposed gives only a *geometric sense* of the vertical distribution of ϵ values. In order to get a more physical feeling about observed distribution, it is necessary to explore the dependence of ϵ on forcing parameters like those characterizing mass, momentum and heat fluxes. Lombardo and Gregg (1989) –hereafter LG98– analyzed a microstructure data set, taken in the upper layer of the Eastern Subtropical Pacific, normalizing h_D in the range $1 < \frac{h_D}{L_{MO}} < 10$ with L_{MO} (see Sec. 5.3.1) and proposed the following equation:

$$\epsilon_2(z) = c_s \epsilon_1(z) + c_b J_b \tag{29}$$

where $\epsilon_1(z)$ is that part of the dissipation induced by the surface stress (*i.e* Eq. 28), J_b is the buoyancy fluxes (see Eq. 24) and c_s and c_b are constants to be determined; in this case, the empirically obtained values for those constants are $c_s = 1.76$ and $c_b = 0.58$. Stips *et al.* (2002) examined Eq. 29 in the context of convective mixing observed in Lake Maggiore, Italy and found a noticeable departure of their measured $\epsilon(z)$ from that of the LG89 scaling. Smyth *et al.* (1997) fitted the dissipation profiles measured in the upper layer of the Equatorial Pacific under light winds, but several hours after the passage of a brief and sudden, violent windstorm, with $c_b = 0.6$ (the value of c_s was not specified in that paper). Next, four parameterizations of the dissipation rate are tested.

In Fig. 31 four normalized profiles of the dissipation rate $\epsilon_n(z_n)$ are shown –subindex n stands for normalized variables– based on the bin–median estimates ($\widehat{\epsilon}$) of the depth–sorted ϵ population (the population includes all individual samples at all stations). Normalization was done by collecting data at all of the stations and sorting them over the normalized depth $z_n = z/h_D$. Bin–median estimates of z_n, and ϵ_n were calculated over 100 consecutive samples in each bin. Here $\epsilon_n = \widehat{\epsilon}/\epsilon_m$, where subindex m indicates the normalized model function used: $m = 1$ refers to Eq. 28 and the resulting normalized profile is plotted in profile 1 of Fig. 31 (filled squares). Case $m = 2$ corresponds to normalizing Eq. 29 with LG89–determined values for coefficients [open circles in Fig. 31]. Case $m = 3$ and $m = 4$ are explained later. The normalized median–bin dissipation is expected to be constant, $\epsilon_n(z_n) = 1$ for

$0 < z_n < h_D$; therefore, when u_* is the only governing parameter it is clear that Eq. 28 reasonably represents the vertical structure of dissipation only in the normalized depth range $\sim 0.4 < z_n < 1$, but not their absolute value, which is overestimated approximately by 3 times ($\langle \epsilon_n \rangle = 3.01 \pm 0.52$). In the surface layer ($0 < z_n < 0.2$), ϵ_n sharply departs from the approximately constant level due to measurement errors and to direct wave forcing. Below $z_n > 1$, ϵ_n also departs from constant values, but for any normalization they are not expected to behave that way there. When normalization is done using Eq. 29 ($m = 2$) with LG89 coefficient values, a shifting of ϵ_n closer to a value of occurs, yielding $\langle \epsilon_n \rangle = 1.46 \pm 0.27$ in the approximated depth range $0.4 < z_n < 1$ (profile 2 in Fig. 31, plotted with open circles). This shows that a combination of ϵ_1 and J_b as given by Eq. 29 improves parameterization, but some modification of the empirical coefficients is needed to achieve a better scaling.

As has been shown in Fig. 27 (Chap. 5) the dataset does not contain measurements obtained during the periods where convective mixing substantially prevailed over the wind–induced turbulence in OSL (the condition $h_D/L_{MO} > 10$ of LG89 is never satisfied; if L_{MO} is calculated based on *in situ* unshifted u_*, the situation does not change). As such, it is not possible to obtain confident estimates of c_b as in the case of almost pure convective balance, $\epsilon \approx c_b J_b$, considered in LG89. Therefore, in order to find a normalized semi–empirical modeling profile of $\epsilon_m(z)$ that gives the best fit to data, two approaches based on the similarity theory are employed. First, note that in the pioneering Monin and Obukhov (1954) paper it is proposed $c_b = 0.6$ is proposed, and subsequent measurements give $c_b = 0.58$ and 0.72 for oceans and $c_b = 0.64$ for the atmospheric boundary layers. Imberger (1985) and Imberger and Ivey (1991) suggest $c_b = 0.46$. According to these reported values for c_b, it is plausible to assume that fixing $c_b = 0.6$ is consistent with considering that any observations of the dissipation rate over $0.6 J_b$ should be attributed to the wind–induced shear production $c_s \epsilon_1$ (thus defining c_s). The best fit for the data gives the normalizing function

$$\epsilon_3(z) = 2.6\epsilon_1(z) + 0.6 J_b, \tag{30}$$

and normalized dissipation is shown in Fig. 31 by profile 3, plotted with filled circles. This gives a very close proximity, on the average, to $\epsilon_n = 1$, yielding $\langle \epsilon_n \rangle = 1.05 \pm 0.25$ in the depth range $0.4 < z/h_D < 1$. Note that for $0.2 < z/h_D < 0.4$, ϵ_n remains
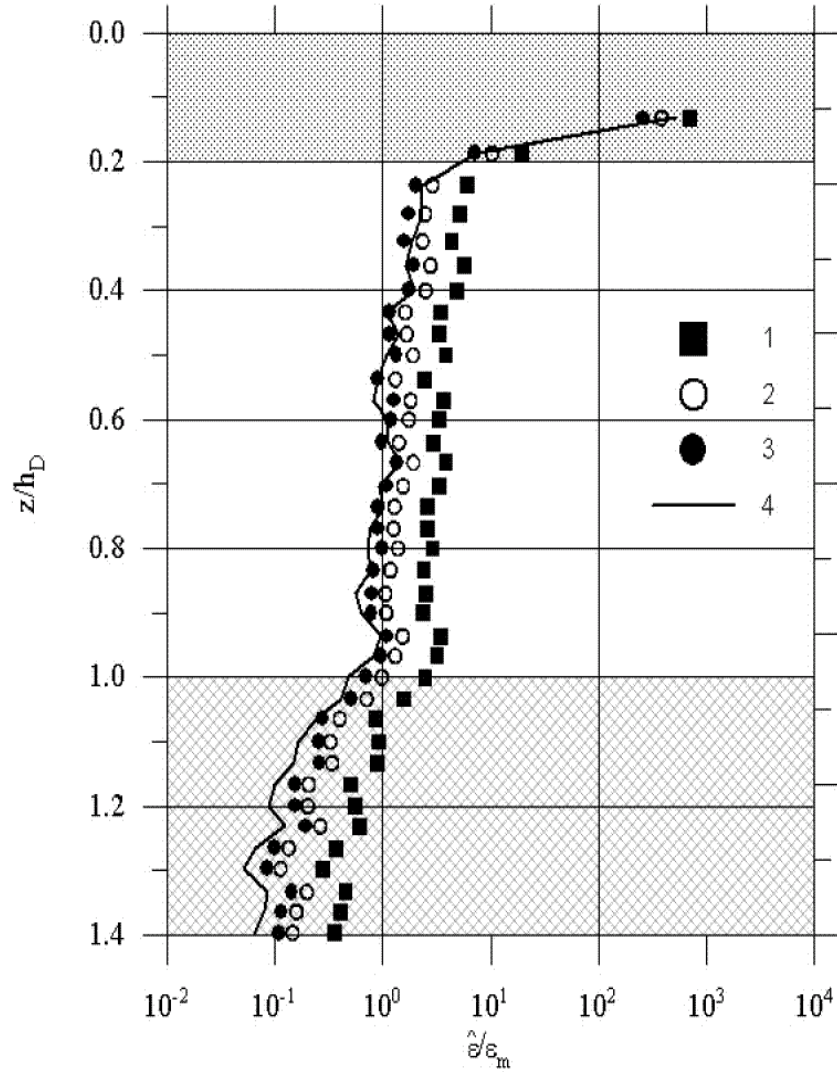
Figure 31. The bin–median profiles of the dissipation rate $\widehat{\epsilon}$ in the upper turbulent (mixing) layer normalized by the modeling dissipation ϵ_m. Here, (1) is the law of the wall given by Eq. 28; (2) is Eq. 29; (3) is a modified formulas of LG89, Eq. 30 is ϵ_n based on the logarithmic–linear similarity model of the velocity profile, and (4) is Eq. 31 with $c_{bm} = 3.7$.

almost constant $\langle \epsilon_n \rangle = 2.3 \pm 0.24$ and only then does the normalized dissipation rapidly increase toward the sea surface.

During the measurements reported by LG89, winds were lower than those observed at $53\,°N$. Their reported values for work done by wind at ten meters are $(E_{10} = 0.2 - 0.6 \text{ Wm}^{-2})$ while at $53\,°N$ the obtained median is $med(E_{10}) = 1 \text{ Wm}^{-2}$, and E_{10} exceeded 0.6 Wm^{-2} for 60% of the data. The downward buoyancy flux, however, was approximately the same in both experiments, about $3 \times 10^{-8} \text{ Wm}^{-2}$ on average. This difference in wind work may possibly account for the larger value of $c_s = 2.6$ (compared to $c_s = 1.76$ of LG89) found in this work.

If high (and possibly low) winds lead to the variation of c_s in equations 29 and 30, the application of $c_s \leq 1.8$ could be limited to a specific range of relatively moderate winds, while a larger constant $(c_s = 2.6$ in the present case) is more appropriate for high winds. This is not an unusual situation in similarity analysis; bulk formulas, for example, employ different values of the friction coefficient when calculating the wind stress for low and high winds.

Alternatively, if all the excessive dissipation above ϵ_1 calculated by Eq. 28 is included into $c_b J_b$ with an empirical constant $c_b = c_{bm}$, then the best fit for $\epsilon_n = \widehat{\epsilon}/\epsilon_{m2}$ is given in Fig. 31 by the continuous profile marked (4) and calculated using $c_s = 1$ and

$$\epsilon_4(z) = \epsilon_1(z) + c_{bm} J_b \tag{31}$$

with $c_{bm} = 3.7$. The proximity of the line given by Eq. 31 to $\epsilon_n = 1$ is good: $\langle \epsilon_n \rangle = 0.98 \pm 0.34$ for $0.4 < z/h_D < 1$. It is interesting to note that the empirical constant c_{bm} falls in the range of values that are often used for stratified atmospheric surface layers with log–linear velocity profiles [Bussinger *et al.* (1971), Dyer (1974), and Stull (1988)]. Eq. 31 can also be interpreted as the result of interaction between shear and convective instabilities, with the latter producing "extra" mixing. In engineering and meteorology, the combined influence of shear and convection is called forced convection.

Although there are different physical assumptions behind the approaches leading to Eqs. 30 and 31, both formulas scale data reasonably well. However, their application for scaling of dissipation in the regions with substantially different hydro–meteorological conditions than those considered here should be done with caution,

given the possible differences in the structure of turbulence and dynamical processes. Despite this uncertainty, it is quite surprising that a simple similarity approach can be used to describe the basic shape of the dissipation profile in the upper oceanic layer, which is influenced by numerous and complex processes such as Langmuir vortices, inertial waves, and others.

6.2   Statistics of the Upper Quasi–Homogeneous Layer

In this section there some basic statistics of turbulence in the UQHL are presented in two parts: first, a comparison between the mixing (h_ϵ) and mixed (h_D) layer is made; then the "lognormality" of the probability distribution function of ϵ, the buoyancy Reynolds number and that of the Richardson number (R_i) is analyzed.

6.2.1   The mixing layer depth

Let's start this part by remembering the definition of mixing layer depth (h_ϵ) introduced in section 2.2.1 as the depth where $\epsilon(z)$ rapidly decreases from about 10^{-7} Wkg^{-1} to $\sim 10^{-8}$ Wkg^{-1}. For active developing turbulence, the depth of mixed (h_D) and that of mixing (h_ϵ) layers (Brainerd and Gregg, 1995) are supposed to be the same, but for decaying or fossil turbulence, h_D should exceed h_ϵ; however, when active turbulence penetrates into a sharp pycnocline h_ϵ can exceed h_D due to incomplete mixing of density stratification. The same correspondence between mixed and mixing layers could be found if atmospheric or shear–induced mixing is developed within an already existing upper quasi–homogeneous layer (UQHL).

Fig. 32 shows four profiles of specific potential density $\sigma_\theta(z)$ and kinetic energy dissipation rate $\epsilon(z)$ to illustrate different regimes of mixing in UQHL (the 1–meter–spaced samples of $\epsilon(z)$ shown were smoothed by a 4–point–running average). The depths h_ϵ and h_D are marked in Fig. 32 by short and longe arrows, respectively. At Station 922/3, where measured winds were relatively low, for example, turbulence is confined to a shallow mixed layer ($h_D = 18$ m) and both depths are very similar i.e. $h_D \approx h_\epsilon$. The depths of mixed and mixing layers are also identical at Sttation 935/2, where active turbulence was generated during the 2nd storm (see Fig. 25) and produced deep $h_D = h_\epsilon = 82$ m. After the same storm, when the wind ceased (Station 936/4), the dissipation profile exhibited a shallower mixing layer ($h_\epsilon = 50$
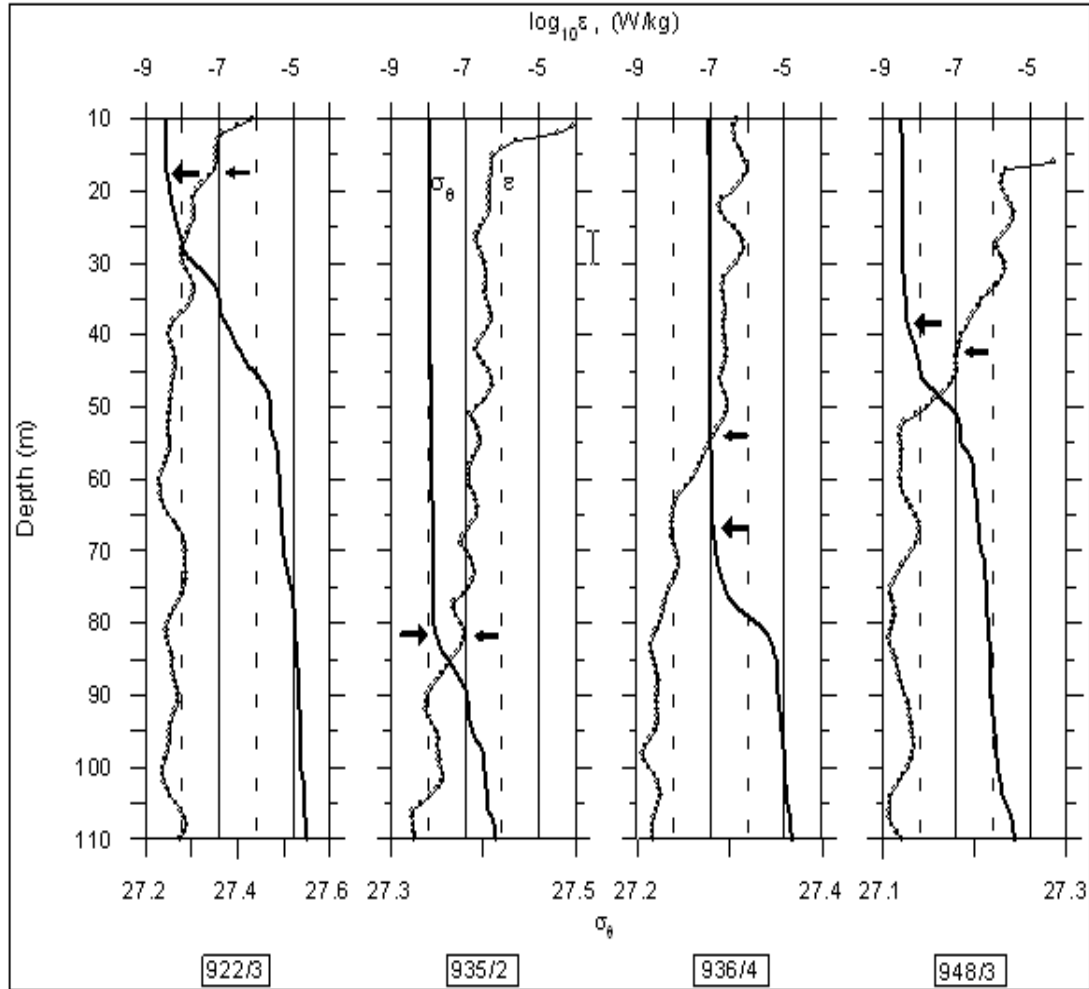
Figure 32. Some examples of the dissipation (dotted lines) and specific potential density (solid lines) profiles showing the depths of mixed (larger arrows) and mixing (smaller arrows) layers at several stations. Station 922/3: turbulence is confined to a shallow mixed layer under relatively low winds. Station 935/2: active mixing induced by the second storm all over the UQHL. St. 936/4: decaying turbulence in a well–mixed layer after the passage of the second storm. Station 948/3: the development of a mixed boundary layer at the beginning of the third storm and related to high–level penetrating turbulence.

m) than a deeper well–mixed layer in the density profile ($h_D = 67$m). This is because the turbulence starts to decay in the lower part of a mixed layer. Finally, at Station 948/3 an example it is found of the situation where the mixing layer ($h_\epsilon = 42$ m) became deeper than the mixed layer ($h_D = 38$m). Energetic turbulence at this last station, which was associated with the beginning of the 3rd storm, is entrained into the pycnocline, developing a homogeneous, well–mixed boundary layer. Note that at Station. 948/3, the dissipation exceeding 10^{-7} Wkg^{-1} penetrates deeper into the pycnocline than the chosen mixing depth. However, at this station h_ϵ clearly indicates the depth where the dissipation within the stratified layer starts to decrease. Figure 32 illustrates various turbulence regimes encountered during the measurements, but at the majority of the stations the depth of the mixed layer was in general agreement with the mixing layer depth. To make a comparison of mixing and mixed layers, a linear regression was calculated between those variables, resulting in $h_\epsilon = 0.97 h_D$, with $r^2 = 0.96$, which is plotted in Fig. 33. To explain this high correlation it must be considered that, during the cruise, the mixed upper layer was generated predominantly by active atmospheric forcing. The average depth of the mixing layer calculated over all available $\epsilon(z)$ profiles is $\langle h_\epsilon \rangle = 48$ m, ranging from 18 to 120 meters.

6.2.2 The probability distribution functions of ϵ, R_i and R_b

Fig. 34a shows the histograms of the logarithm of dissipation rate $[\log_{10}(\epsilon)]$ for all 1–meter averaged samples pertained to the mixing layer ($z < h_\epsilon$). Separately, Fig. 34b gives the distribution of $\log_{10}(\epsilon)$ but only for the data in the depth range $z_{cw} < z < h_\epsilon$, where $z_{cw} = 16$ m as explained in first section of this chapter; below this depth it is supposed that data is not contaminated by surface waves and ship–induced turbulence. The Gaussian approximations of observed distributions are shown by solid lines. The distribution shown in Fig. 34a substantially departs from log–normal approximation, having a long tail of almost equal probability in the range $-4.5 < \log_{10}(\epsilon) < -2$. This indicates that very large values of ϵ, which were mostly observed in the near–surface layer, belong to a different statistical population than those having $\log_{10}(\epsilon) \leq -4$. The probability distribution of ϵ within the mixing layer, at depths $z > z_{cw}$, is perfectly lognormal (Fig. 34b) with $\mu = \langle \log_{10}(\epsilon) \rangle = -0.83$ and

$rms\left(\log_{10}\left(\epsilon\right)\right) = 0.76$; the corresponding mean and median values are $\langle\epsilon\rangle = 2.2\times10^{-6}$ and $med(\epsilon) = 1.5 \times 10^{-7}$ Wkg^{-1}.

If turbulence in the upper layer is generated mainly by wind stress, as discussed in Sec. 5.3.1 , then the mechanism for their generation below the wave–braking zone is related to shear instability of drift currents, which can be analyzed using the probability distribution function of the gradient Richardson number $R_i = N^2/S_h^2$ (see Section 2.3.2). The shear was calculated from ADCP data with 8–meter vertical resolution and then interpolated to $\Delta z = 2$ m in order to match the resolution of buoyancy frequency, which in turn was computed over the sorted NB-CTD density profiles. Further, the S_h^2 and N^2 profiles were low–pass filtered with running averages over 4 points and then interpolated at $\Delta z = 1$ m.

The cumulative distribution function of the Richardson number $F(R_i)$ in the depth range $z_{cw} < z < h_\epsilon$ is given in Fig. 35 (thick curvy lines labeled 1). It shows that the median of R_i is as low as 0.1 –indicated by thin vertical line– and the probability of $R_i < 0.25$ is above 60%, as pointed out by an arrow on the vertical axis. This distribution, as well as that for ϵ, is well approximated by lognormal probability law, whose approximation is shown in the same figure by a solid straight line.

On the other hand, the state and intensity of mixing in UQHL can be specified by two related variables: K_b, and the buoyancy Reynolds number $R_{e_b} = \epsilon/(30\nu N^2)$ –both variables were introduced in section 2.3.2– which can also be expressed as $R_{e_b} = K_b/6\nu$ signifying the ratio between eddy diffusivity and molecular diffusivity ν. The distribution of the buoyancy Reynolds number $F(R_{e_b})$ is also shown in Fig. 35 (thin curvy line labeled 2). It shows a wide range [between 10 and more than 10^6, upper horizontal axis], indicating highly–energetic turbulence almost everywhere in the mixing layer. The median of R_{e_b} is as high as 4×10^3 and its corresponding lognormal approximation (the straight heavy dashed line) fits 80% of the upper end of the $F(R_{e_b})$ distribution starting from $R_{e_b} \sim 5 \times 10^2$. This implies that a fully–developed cascade of turbulent energy [which is characterized by the lognormal distribution of the dissipation (Gurvich and Yaglom, 1966)] exists only in those layers where K_b exceeds the molecular viscosity by a factor of 6×500 or more. About 20% of the samples at the lower end of $F(R_{e_b})$ depart from log–normal approximation
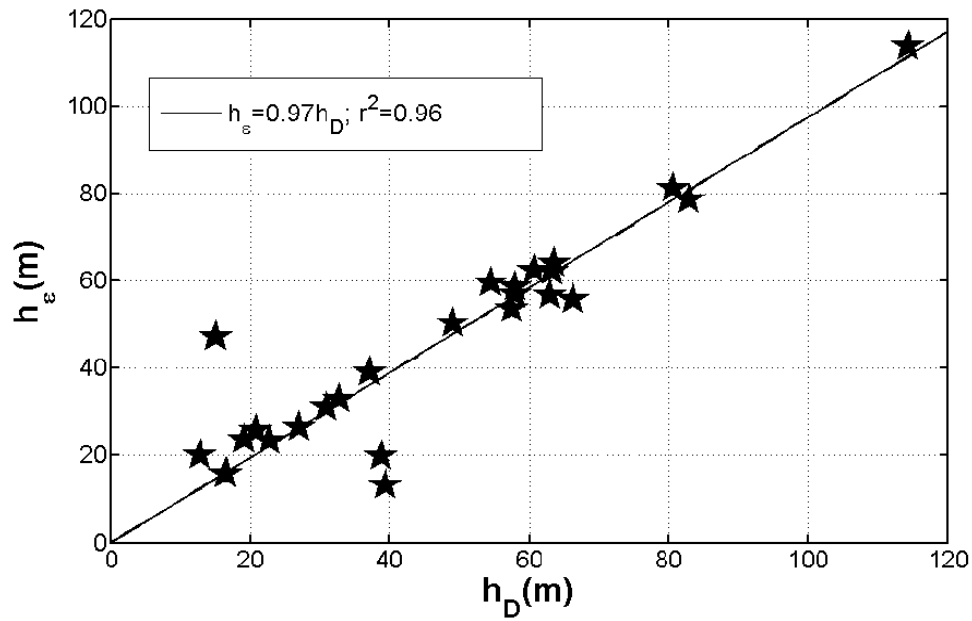
Figure 33. The depth of the turbulent (mixing) layer h_ϵ .*vs.* the mixed layer depth h_D obtained from MSS profiles.
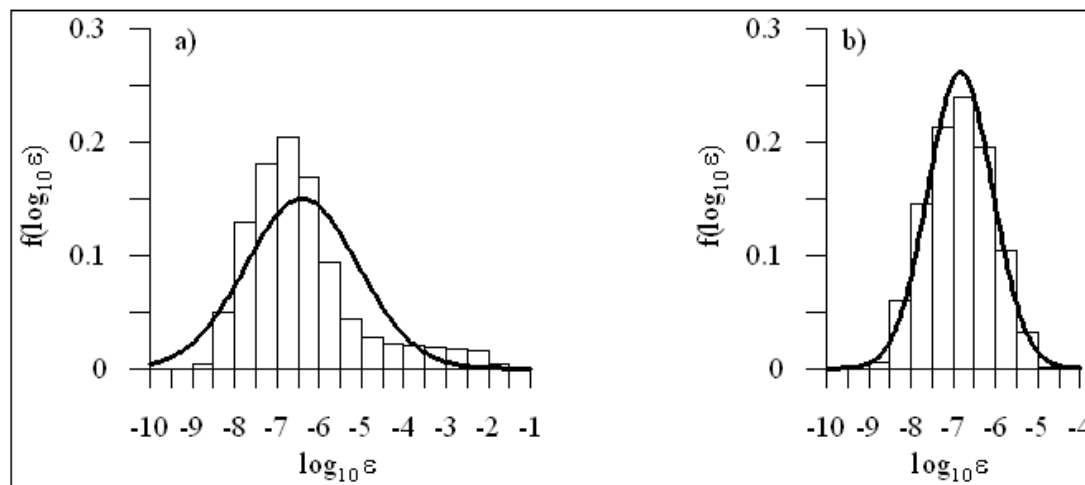
Figure 34. Histograms of the logarithm of the kinetic energy dissipation rate in the depth ranges 2 m $< z < h_\epsilon$ (a) and $z_{cw} < z < h_\epsilon$ (b). h_ϵ is the depth of the upper turbulent layer (mixing layer). Gaussian approximations are shown by heavy lines.
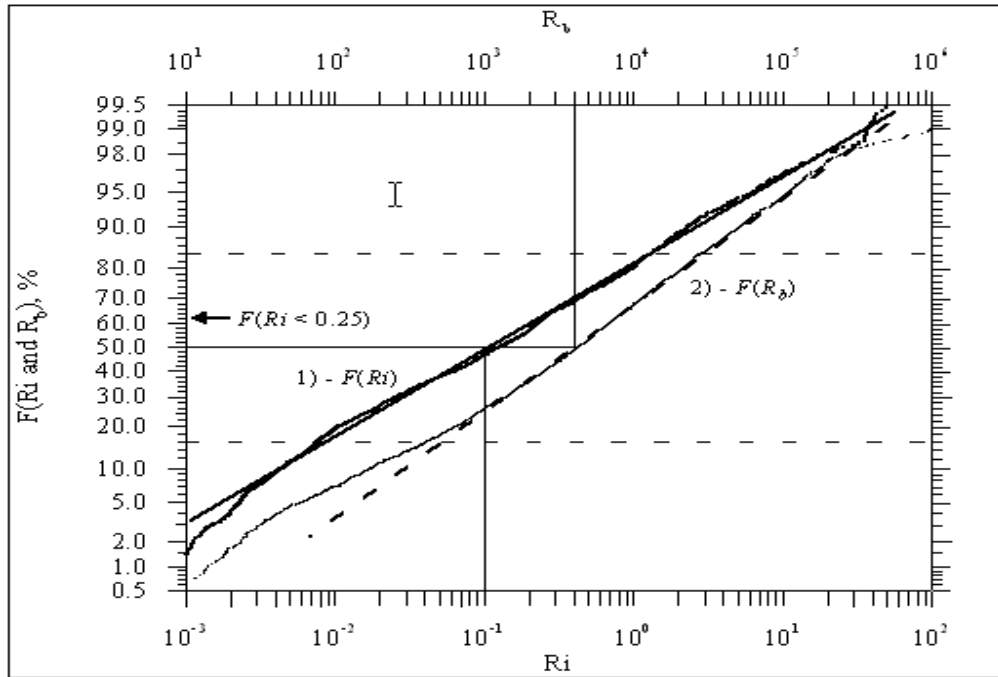
Figure 35. The cumulative distribution functions of the Richardson $F(R_i)$ and buoyancy Reynolds $F(R_b)$ numbers in the depth range $z_{cw} < z < h_\epsilon$. The corresponding lognormal approximations are given by straight and dashed lines. The median of R_b is 4×10^3; for R_i the median is 0.1, and the probability of $R_i < 0.25$ exceeds 60%.

and possibly belong to the base of UQHL, where internal wave breaking generates patches of weak intermittent turbulence, entrained further into the mixing layer.

6.3 Mixing scheme based on R_i

The importance of shear instability in generating mixing within the UQHL (see Secs. 5.3.1 and 6.2.1) along the 53 °N transect, is also illustrated in Fig. 36 by vertical profiles of the diffusivity K_b and Ozmidov scale, $L_O = (\epsilon/N^3)^{1/2} = (K_b/\gamma N)^{1/2}$, and corresponding profiles of sorted density σ_θ, shear, and the Richardson number at two typical stations: 936 (active, but decaying turbulence after the 2nd storm) and 948 (developing turbulence at the beginning of a new storm). The original profiles of the dissipation rate $\epsilon(z)$ are also shown in Fig. 36 to make clear that the general decrease of K_b and L_O with depth is not a simple reflection of changes in stratification, but the consequence of decreasing turbulence. It is interesting that the choice of the mixing

layer depth h_ϵ that has been made using solely $\epsilon(z)$ profiles roughly corresponds to the depths where R_i is close to 0.25 (Station 948), or even below 0.25 (Station 936). While, as said previously, $\langle h_\epsilon \rangle = 48$ meters, the depth, where $R_i < 0.1 - 0.25$ is 38 m on the average. This suggests that h_ϵ does associate with the depth of the critical Richardson number, which varies in the range $R_{icr} = 0.1 - 1$, depending on specifics of local generation process.

The diffusivities in the mixing layer are high ($10^{-2} - 10^{-1} \text{m}^2\text{s}^{-1}$), but K_b sharply decreases entering the pycnocline, where the diffusivity is reduced to typical values of $10^{-5} - 10^{-4} \text{m}^2\text{s}^{-1}$. Slightly below the base of mixing layer, at the depths where R_i is close to 1, the Ozmidov length–scale drops to about 1 m, which is a characteristic value for the lower boundary of the inertial subrange in the kinetic energy spectra of stratified turbulence in oceanic thermocline (Gargett *et al.*, 1981). All this indicates that local shear instability plays an important role in generating turbulence in the UQHL. Note that several modeling and observational studies (*e.g.*, Price *et al.*, 1986) reported a slab–like velocity profile and therefore low shear in the UOL. In these studies, however, measurements of the highest shear were usually observed near the sea surface. The shear continuously decreased with depth, reaching a minimum value near the bottom of the mixing layer or even deeper in the pycnocline (see Fig. 36), unlike in the case of a slab–layer velocity profile.

Two $K_b(R_i)$ dependencies obtained at Stations 933 and 939 are given in Fig. 37. It is believed that these examples represent a typical quasi–stationary balance of turbulence kinetic energy in the mixing layer below the highly turbulent zone near the surface. The reading at the stations were taken after the 1st and 2nd storm, exhibiting relatively high dissipation in the depth range $24 - 48$m, where $R_i < 1$. In both panels of Fig. 37, K_b tends to decrease with the increase of R_i. The trends can be approximated using several semi–empirical models in the spirit of classic Munk–Anderson parameterization (Munk and Anderson, 1948) given by:

$$K_b = \frac{K_0}{\left(1 + \frac{R_i}{R_{icr}}\right)^p} P_{r_t}^{-1} \tag{32}$$

where K_0 is the eddy viscosity in non–stratified flow, P_{r_t} is the turbulent Prandtl
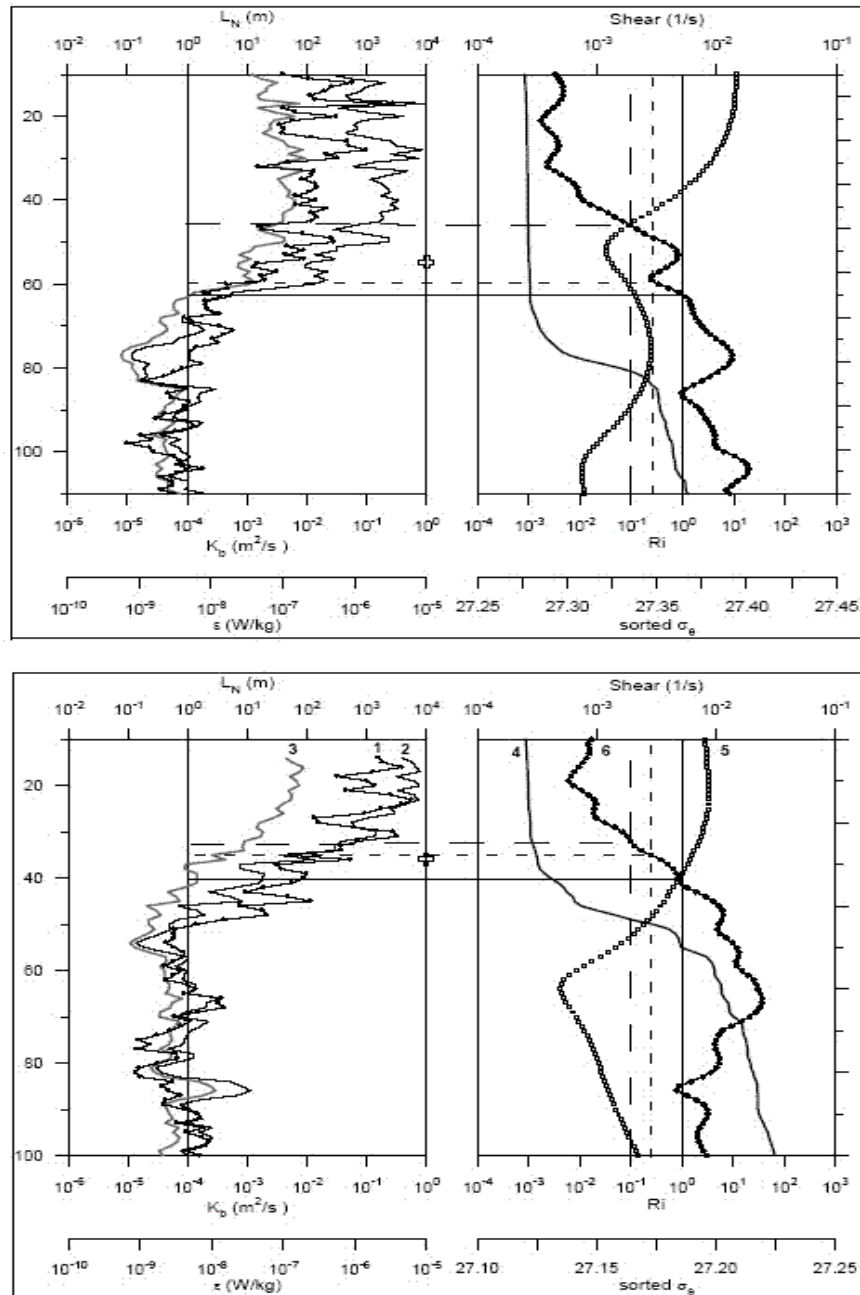
Figure 36. Profiles of the dissipation rate (1), diffusivity (2), and Ozmidov scale (3) (left) and the corresponding profiles of sorted density (4), shear (5), and R_i (6) (right) at Station 936 (upper plot) and Station 948 (lower plot). The horizontal long and short dashed lines and the straight line show the depths where $R_i = 0.1, 0.25$, and 1, respectively. The crosses mark the mixing layer depths h_ϵ which are near the depth where $R_{icr} \approx 0.1 - 0.3$. The Ozmidov scale decreases to ~ 1 m at the depth where $R_i \approx 1$ is observed.

number, which is also thought to be a function of R_i, often written as

$$P_{r_t} = \alpha_t = \left(1 - \frac{R_i}{R_{i\beta}}\right)^{-r}.$$ (33)

and R_{icr} and $R_{i\beta}$ are critical Richardson numbers, which do not necessarily have the same numerical values because R_{icr} is associated with transition from a non–turbulent to turbulent regime (or in other words, from weak to well–developed turbulence). $R_{i\beta}$, on the other hand indicates a specific state of stratified shear turbulent flow when vertical mixing (buoyancy flux) starts to be affected by stratification to a greater extent than the momentum flux. For R_{icr}, the most regularly used values are 0.25 and 0.20 [*e.g.*, Monin and Yaglom, 1981; Pacanowski and Philander, 1981; Peters *et al.*, 1988]. A lower $R_{icr} = 0.1$ has also been suggested in several studies [*e.g.*, Munk and Anderson, 1948; Lozovatsky *et al.*, 1993; Pelegri and Csanady, 1994; Lozovatsky *et al.*, 2000]. The critical $R_{i\beta}$ in Eq. 33 has often been taken to be equal to R_{icr} [*e.g.*, Pacanowski and Philander, 1981; Peters *et al.*, 1988 and others], but some authors used different values for R_{icr} and $R_{i\beta}$ in numerical calculations and data analyses ($R_{icr} = 0.1$ and $R_{i\beta} = 0.3$ [Munk and Anderson, 1948], $R_{icr} = 0.1$ and $R_{i\beta} = 0.05$ [Paka *et al.*, 1999; Toorman, 2000]). A more complex formulation of K_b and α_t than those given by Eqs. 32 and 33 was suggested, for example, by Henderson–Sellers (1982), who analyzed atmospheric measurements of Linden (1979) and Ueda *et al.* (1981) and introduced

$$K_b \sim K_0 \left[1 + \left(\frac{R_i}{R_{icr}}\right)^2\right]^{-1}$$ (34)

with $R_{icr} \sim 0.165$ and

$$\alpha_t = 1 + \frac{0.74R_i}{1 + 37R_i^2}$$ (35)

which leads to the lowest $R_{i\beta} \simeq 0.02$, if the formula for α_t is reduced to Eq. 33. Recent atmospheric turbulent measurements by Monti *et al.* (2002) also support Eq. 33 but require $R_{i\beta} = 0.05$ and $r = 1/2$. The majority of previous studies, however, point to $r = 1$ as a preferable choice in stipulating the power dependence of α_t on R_i. This in turn grants a constant value of the flux Richardson number $R_f = \alpha R_i$ at high R_i, which is consistent with the assumption of a constant mixing efficiency γ (Oakey, 1985) when K_b is calculated. Any r larger than 1 leads to a reduction of

R_f at high R_i that could probably take place in sharp density interfaces but should not be expected in weakly–stratified upper turbulent layer.

Empirically determined values for the exponent p in Eq. 32 range between 0.5 (Munk and Anderson, 1948) and 2 (Pacanowski and Philander, 1982). If the eddy viscosity K_0 in non–stratified shear ocean flow (see Eq. 32) is specified using vertical shear S_h, turbulent kinetic energy e_t or the dissipation ϵ, or $K_0 \sim e_t/S_h^2$ (e.g. Peters et al., 1988), then the most natural choice for p coefficient would be $p = 1$. This makes $K_M \sim \epsilon/N^2$ and at $R_i >> R_{icr}$, which are generally accepted formulas for the eddy viscosity in stratified ocean. The above asymptotic for K_M derived from Eq. 32 is in consonance with the assumption that, in a stratified layer without any local source of shear energy production, the local turbulence scale l_{tr} should be equal to the Ozmidov scale, $l_{tr} = L_O$, providing $K_M \sim l_{tr}\sqrt{e_{tr}}$. Accordingly, in non–stratified shear flow, $l_{tr} = L_{S_h} \sim (\epsilon/S_h^3)^{1/2}$, where L_{S_h} is the Tchen (1954) shear scale.

In an intermediate range of the Richardson numbers ($\sim 0.2 < R_i <\sim 2$), the scale l_{tr} can be specified as $L_R = (\epsilon/N^2 S_h)^{1/2}$ (Lozovatsky et al.,1993), leading to $K_M \sim \epsilon/(N^2 S_h)^{2/3}$, which requires $p = 2/3$. The length–scale L_R, which can also be written as u_{l*}/N using local friction velocity u_{l*}, replaces L_O in spectra of turbulent kinetic energy $E(\kappa)$ if a production subrange, where $E(\kappa) \sim (\epsilon/S_h)\kappa^{-1}$, emerges between the inertial $E(\kappa) \sim \epsilon^{2/3}\kappa^{-5/3}$ and buoyancy $E(\kappa) \sim N^2\kappa^{-3}$ subranges due to locally generated shear–induced turbulence (Lozovatsky, 1996). Therefore, $p = 2/3$ could be a likable choice for the diffusivity parameterization, if turbulence is developed by a combination of non–local (wind stress in this case) and local (inertial oscillations, for example) shear sources.

The original Munk–Anderson exponent $p = 1/2$ gives $K_M \sim \epsilon/(NS_h)$ for $R_i >> R_{icr}$, which does not correspond to any known turbulent spectral length–scale, but correctly reflects the dependence between K_M and major governing parameters of stationary stratified turbulence. Two other popular values of $p = 2$ (Pacanowski and Philander, 1982) and $p = 3/2$ (e.g., Peters et al,. 1988; Pelegri and Csanady, 1994) produce $K_M \sim \epsilon S_h^2/N^4$ and $K_M \sim \epsilon S_h/N^3$, respectively. To satisfy stationary balance of the turbulent kinetic energy, in these cases the flux Richardson number (or γ) should be a function of R_i, which, as mentioned, is unlikely in a weakly stratified UQHL.
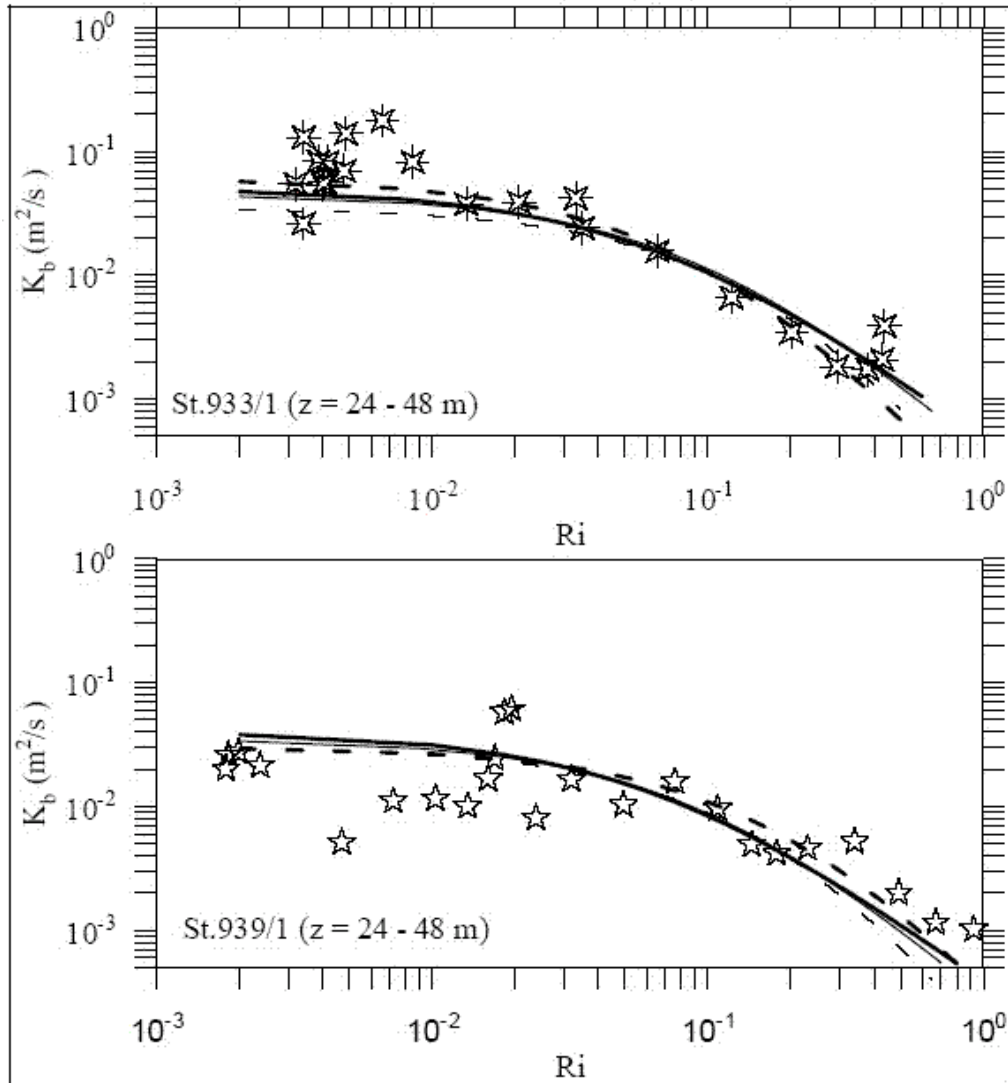
Figure 37. The eddy diffusivity $K_b = 0.2\epsilon/N^2$ .vs. the Richardson number R_i at St. 933 (upper panel) and Station 933 (lower panel). The symbols are 1–meter averaged samples. The modeling dependencies $K_b(R_i)$ given by Eqs. 32 (using $p = 2/3$, bold line, and $p = 1$, continuous line) and 33 with $r = 1$.

The above discussion suggests that $r = 1$ in Eq. 33 is probably the most rational choice for the $\alpha_t(Ri)$ function. Because Eq. 32 with $p = 2/3$ and/or $p = 1$ links $K_b(R_i)$ to a specific spectral structure of turbulent fluctuations (via corresponding length scales L_R and L_O). These p values are favored in comparison to more traditional $p = 1/2, 3/2$ and 2. The critical Richardson numbers R_{icr} and $R_{i\beta}$ were selected from the set of values already discussed ($R_{icr} = 0.1$ or 0.2, and $R_{i\beta} = 0.05$ or $R_{icr} = R_{i\beta} = 0.1$ or 0.2).

Eqs. 32 and 33 fit the individual data samples of K_b at Station 933 and Station 939 reasonably well with $p = 2/3$ as well as with $p = 1$ (Fig. 37, bold and thin continuous lines). The scaling values of eddy viscosities K_0 are 5×10^{-2} and $4.5 \times 10^{-2} \text{m}^2\text{s}^{-1}$ for Station 933 and 4×10^{-2} and $3.5 \times 10^{-2} \text{m}^2\text{s}^{-1}$ for Station 939, respectively. While $p = 2/3$ requires different values of $R_{icr} = 0.1$ and $R_{i\beta} = 0.05$ to fit the data best, the exponent $p = 1$ (which corresponds to the Ozmidov scale L_O) satisfies the data to the same extent with $R_{icr} = R_{i\beta} = 0.1$. Parameterization of Pacanowski and Philander (1982), with the original set of exponents and constants ($p = 2, r = 1, R_{icr} = R_{i\beta} = 0.2$), but slightly higher $K_0 = (3 - 3.5) \times 10^{-2} \text{m}^2\text{s}^{-1}$ compared to their $10^{-2} \text{m}^2\text{s}^{-1}$, deviates from the data more than the first two approximations (see the thin dashed lines in Fig. 37). To fit the data using Eq. 32 with $p = 3/2$ (e.g., Pelegri and Csanady, 1994) used different values of R_{icr} and $R_{i\beta}$ at each station.

Turbulent mixing in the UQHL is forced mainly by wind stress at the sea surface and to a lesser extent by local instabilities. Therefore, in order to compare and parameterize the diffusivities observed under various winds, individual samples obtained at a number of stations are normalized with different friction velocities u_* using the Monin–Obukhov (1954) similarity theory, which gives $K_{sf} = \kappa u_* z$ as the vertical diffusivity profile in the surface boundary layer. The result is provided in Fig. 102, where the bin–median values of $\widehat{K}_{bn}$ and $\widehat{R}_i$ are fitted by formula

$$K_{bn} = \frac{K_b}{\kappa u_* z} = \frac{1}{\left(1 + \frac{R_i}{R_{icr}}\right)^p \left(1 + \frac{R_i}{R_{i\beta}}\right)} \tag{36}$$

with two sets of parameters p, R_{icr} and $R_{i\beta}$. The 90% bootstrap confidence limits for $\widehat{K}_{bn}$ were calculated using 1000 resampled points when the actual number of samples was 15 for each bin. The data were taken from Stations 933, 936, 939, and 948,
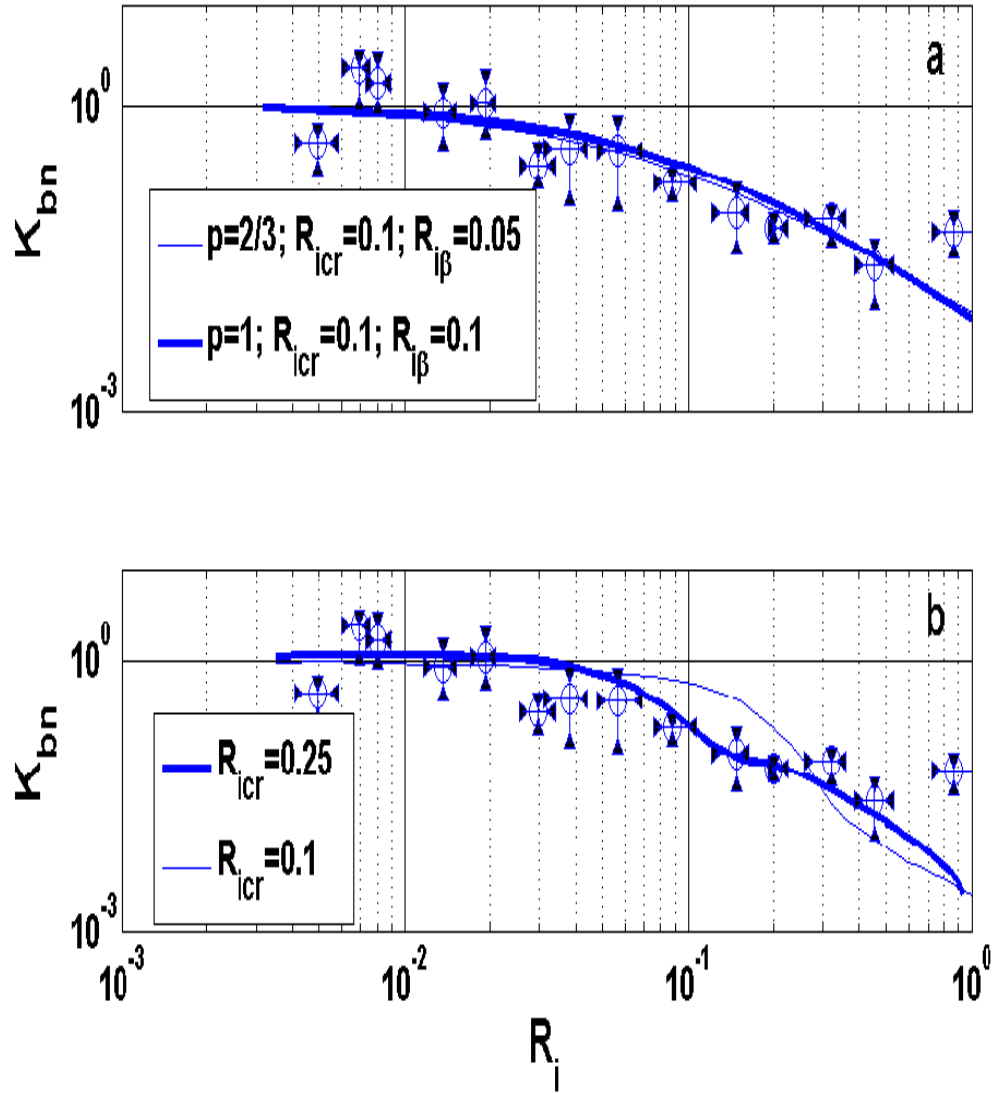
Figure 38. The bin–median estimates of the normalized diffusivity $K_{bn} = K_b/\kappa z u_*$, at the probability–equal R_i–intervals (large circles) with 90% bootstrap confidence limits shown for both variables. The data superimposed by the modeling functions were given by Eq. 36 in panel (a) and Eq. 37 in panel (b). Values used for parameters are indicated in the inserts at each panel; note that the curves in panel (a) are undistinguishable for the parameters values shown.

where MLD = 38 - 56 m and the wind speed varied between 4.5 and 14.3 ms^{-1}. Both lines in Fig. 38 fit the bin–median samples quite well in the range $\widehat{R}_i$ range $1.3 \times 10^{-2} - 5 \times 10^{-1}$, where the coefficients of determination are 0.80 and 0.77 for lines 1 and 2, respectively. At very low levels, $\widehat{R}_i < 0.01$, the data depart significantly from Eq. 36. This could be attributed to insufficient accuracy of N^2 calculations when density gradients become very small. A decrease of $\widehat{K}_{bn}$ at the lowest $\widehat{R}_i$ in Fig. 38a may, however, signify a real tendency for a buoyancy vertical exchange to vanish in non–stratified shear flows. What is evidently clear from Fig. 38a is that analyzed data do not support an explosive growth of the diffusivity at $\widehat{R}_i < 0.25$ as reported by Peters *et al.* (1988) for patch turbulence in equatorial thermocline.

Recently, Soloviev *et al.* (2001) suggested to parameterizing the normalized diffusivity $K_b/(\kappa u_* z)$ at $0 < R_i < R_{icr} = 0.25$ as $(1 - R_i/R_{icr})$ and use the Peters *et al.* (1988) formula for K_b at $R_i > R_{icr} = 0.25$. This leads to

$$K_{bs} = \frac{K_b}{\kappa u_* z} = 1 - \frac{R_i}{R_{icr}} + \frac{5 \times 10^{-4}}{\kappa u_{*z} \left(1 - 5R_i\right)^{2.5}} \tag{37}$$

The authors showed that the results of microstructure measurements taken in the upper turbulent layer of the western Pacific warm pool generally agree with Eq. 37. As the foundation of Eq. 37 most closely corresponds to Eq. 36, it is instructive to compare the two formulas with respect to the bin–median diffusivities obtained in the upper layer of the North Atlantic. The modeling functions (36) and (37) are presented in separate panels of Fig. 38 overlying the same experimental data set. If $\widehat{K}_{bs}$ is calculated using $R_{icr} = 0.25$, the result substantially departs from measurements taken at intermediate $\widehat{R}_i$, but when R_{icr} is reduced to 0.1, the correspondence with experimental data becomes much nicer (see Fig. 38b). The proximity between the data and $\widehat{K}_{bS}(R_i)$, calculated with $R_{icr} = 0.1$, is comparable with that shown in Fig. 38a for formula (36). The corresponding coefficients of determination are 0.7 and 0.74 for Eq. 36 and 0.6 for Eq 37 disregarding two samples at the highest and lowest $\widehat{R}_i$. Note, Soloviev *et al.* (2002) who introduced Eq. 37, show the modeling curve $\widehat{K}_{bS}(R_i)$ with $R_{icr} = 0.25$, which also goes slightly above the averaged data points [Fig. 10 of Soloviev *et al.* (2002)]. The effect is manifested in present work data. This suggests that using Eq. 37 with lower R_{icr} ($R_{icr} = 0.1$) should improve performance of this parameterization making it more comparable to Eq. 36.

6.4   Column–Integrated Dissipation

Because turbulence in the mixed layer was dominated by the wind stress, the wind work –denoted by E_{10}– is compared with the dissipation in the upper turbulent layer, using Eq. 30, and calculating the column–integrated dissipation rate as

$$\widetilde{\epsilon}_{int} = \int_0^{h_\epsilon} dz \rho_w \epsilon(z), \tag{38}$$

where h_ϵ is the mixing layer depth, which in this case, at almost all stations, is equal to MLD. Oakey and Elliot (1982) were among the first to make estimates of the dissipation of the wind work E_{10} in the upper turbulent layer using direct measurements of small–scale shear taken by an airfoil sensor. They reported $\widetilde{\epsilon}_{int} \approx 0.01 E_{10}$ for a 20–meter near–surface boundary layer.

Because it is not possible to retrieve microstructure measurements from the upper near–surface layer ($z < z_{cw}$), the "model" dissipation profiles (Eqs. 30 and 38) were used to calculate $\widetilde{\epsilon}_{int}$ in the mixing layer ($0 < z < h_\epsilon$) with local values of u_*, J_b, and h_ϵ at each station. The integrated "measured" dissipation $\widetilde{\epsilon}_{obs}$ at every station was also obtained for the inner turbulent layer of thickness $h_{obs} = h_\epsilon - z_{cw}$. The estimates of mean dissipations $\overline{\epsilon} = \widetilde{\epsilon}_{int}/h_\epsilon$ and $\overline{\epsilon}_{obs} = \widetilde{\epsilon}_{obs}/h_{obs}$ given in Fig. 39 demonstrate a good correlation, showing that $\overline{\epsilon}$ is about twice $\overline{\epsilon}_{obs}$.

A plot of the dependence of integrated dissipation on wind–work $\widetilde{\epsilon}_{int}(E_{10})$ is given in Fig. 40. It indicates that the data samples can be approximated well by $\widetilde{\epsilon}_{int} = 0.05 E_{10}$ and suggests that, on the average, $\widetilde{\epsilon}_{int}$ may account for about 5% of the wind work at 10 m above the sea surface; the ratio $\widetilde{\epsilon}_{int}/E_{10}$ varies between 3 and 7%. This is consistent with the estimates of Richman and Garrett (1977) that the rate of energy entering the ocean from the wind is in the range $2 - 10\%$ of the wind work E_{10}. It is likely, however, that larger MLDs are associated with higher mean dissipation rates, when turbulence is active within the upper boundary layer and vice versa. Some of the unanswered questions in this context are: Is the fraction of wind work that dissipates during the mixing layer formation independent of the layer depth? and, Does turbulence in deeper layers consume a larger fraction of wind work than that in shallower layers? The answer are given in Fig. 41, where a clear tendency of $\widetilde{\epsilon}_{int}/E_{10}$ growth is associated with larger h_ϵ. The approximated empirical power–law function is simply given to emphasize the trend.
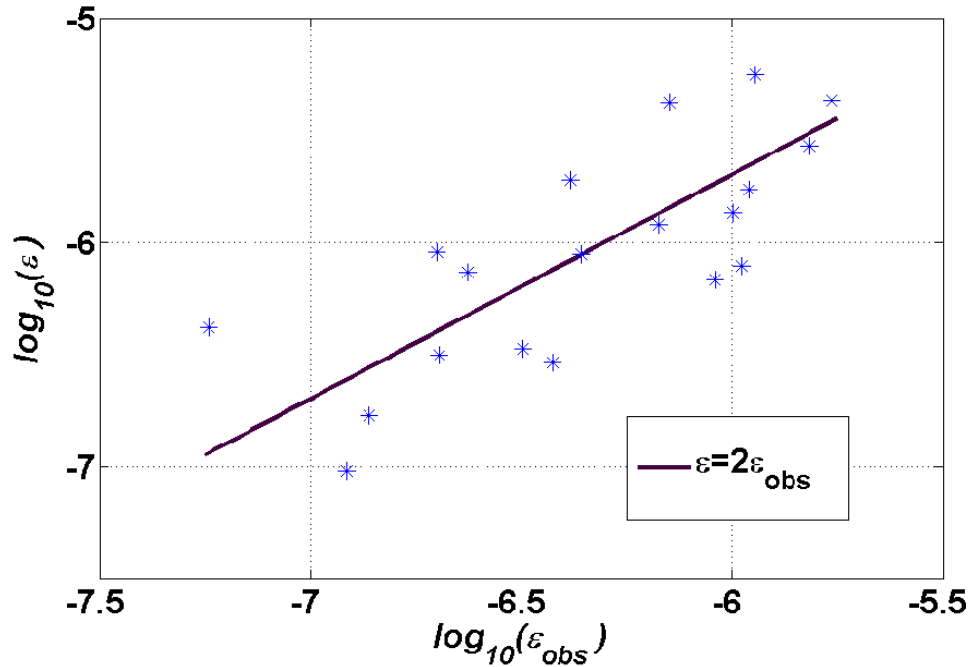
Figure 39. Correlation between the measured ϵ_{obs} and integrated dissipation (ϵ_3 estimated through Eq. 30) per unit depth.

The observed growth of the ratio $\widetilde{\epsilon}_{int}/E_{10}$ with increases of h_ϵ seems to be consistent with results of numerical and laboratory experiments [Kantha and Clayson, 2000a,b] which suggest that in growing turbulent layers, the entrainment rate decreases with time. In other words, as the mixed layer deepens, the entrainment rate decreases due to the increase of the Richardson number or to the inability of eddies to raise dense fluid against the negative buoyancy of thermocline. In order to accommodate this dynamic constraint and realize the bulk energy balance, the column averaged dissipation rate increases in the mixed layer, as was evident from the laboratory mixed–layer measurements of Kit *et al.* (1997). The increase of $\widetilde{\epsilon}_{int}/E_{10}$ ratio may also indicate a change of integrated mixing efficiency $\widetilde{\gamma}$ with respect to E_{10} with the increase of MLD (which is unrelated to the mixing efficiency and flux Richardson number based on local variables). One of the customary assumptions that the averaged buoyancy flux due to entrainment is proportional to the energy imparted by the wind, therefore, should be reconsidered in view of the above finding that this proportionality constant can be variable.
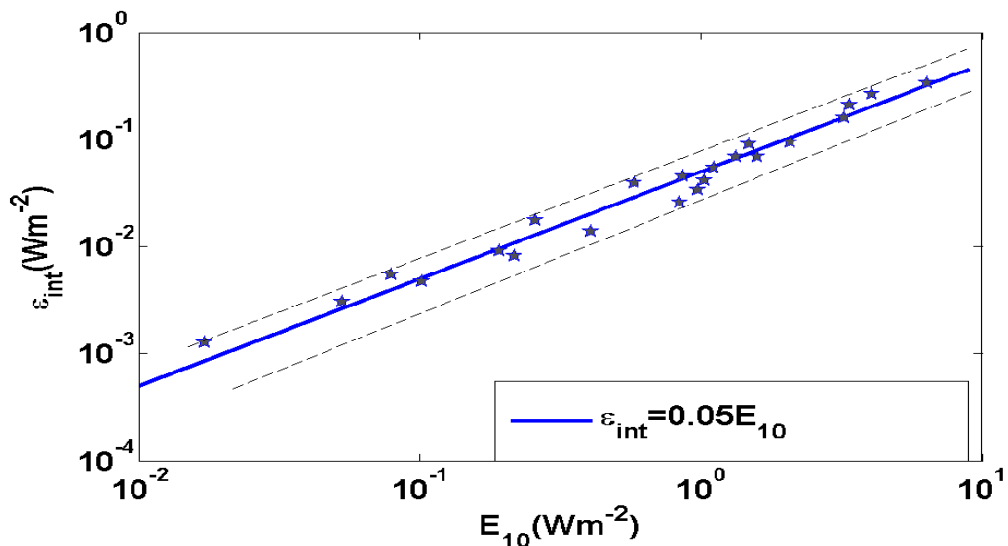
Figure 40. The dependence of integrated dissipation in the upper mixing layer as a function of the wind work. Calculation of ϵ_{int} is explained in text and was done using local values of u_*, J_b and h_ϵ at each station. Upper and lower broken lines show the limits for the linear regression.
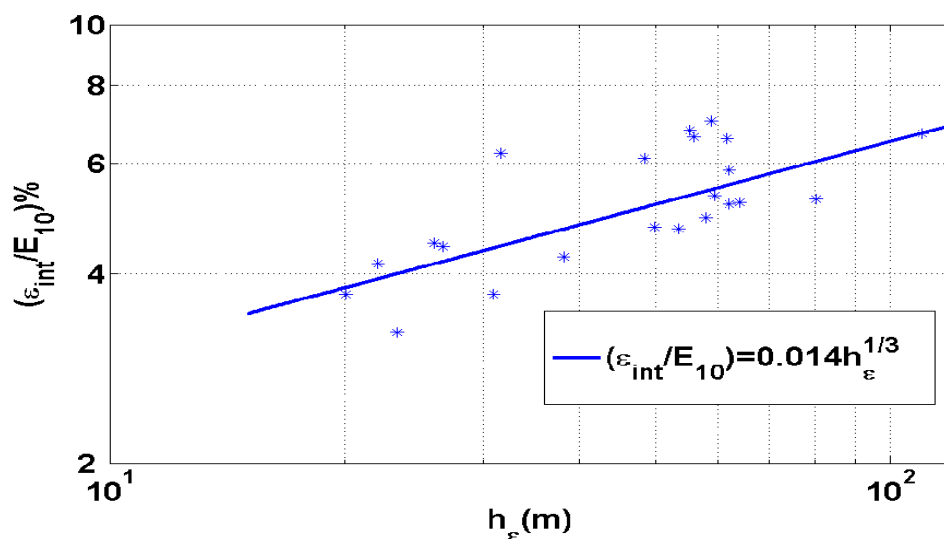
Figure 41. The dependence of thickness of the mixing layer and the ratio ε_{int}/E_{10} the correlation is based on mixing layer depths from 22 stations.

<div align="right">

CHAPTER 7

Summary

</div>

The response of the mixed layer depth (MLD) to short–term (synoptic) variations of atmospheric forcing in the North Atlantic Ocean was analyzed using CTD data, microstructure profiling, ADCP velocities and atmospheric measurements taken during the last 12 days of April 2001 at 42 stations located close to $53\,°$N. To the best of our knowledge, this is the first time an analysis of this kind has been conducted for this important oceanographic region. The main findings of this study are presented in this final chapter.

7.1   General hydrography and ageostrophic currents

• The oceanographic transect, which followed the climatological position of zero annually–averaged wind stress curl (WSC), crosses the Labrador Current and multiple branches and meanders of the North Atlantic Current. The basin–scale variation of WSC is probably responsible for the observed general deepening of the thermocline from west to east. Mesoscale thermohaline frontal intrusions were mainly observed in the pycnocline not affecting the vertical structure of density in the upper mixed layer

• Atmospheric forcing during observations was characterized by relatively high winds (the mean wind speed was 10.7 ms^{-1}) and negative surface heat balance (the sea surface temperature was on the average $2.5\,°$C higher than the air temperature). Three strong storms were encountered during the measurements, and the wind stress at drift stations reached $0.2 - 0.4$ Nm^{-2}. The averaged amplitude of Ekman transport $\langle M_E \rangle$ calculated using the wind stress was about 1 m^{2}s, but during the storms the magnitude of $\langle M_E \rangle$ went up to $3.4 - 3.5$ m^{2}s.

• Estimates of ageostrophic flow were obtained following Chereskin and Roemmich

(1991) and Wijffels *et al.* (1994). Results suggest that the ageostrophic meridional transport across $53\,°$N in the Atlantic is mainly limited to the depths below the upper 200–meter layer. The ageostrophic flows in the upper layer were mainly southward and eastward. The meridional ageostrophic transports, M_{Ey}, were usually larger than those calculated using the residuals between ADCP and geostrophic velocities, M_{AG}, but were in the same direction as M_{Ey} when $|M_{AG}|$ exceeded 0.3 m^{2}s.

7.2   Mixed layer depth

• To identify the MLD at each station, the algorithm developed by Kara et al. (2000) was employed. The deepest observed mixed layer depth h_D was 110 m, the mean $\langle h_D \rangle = 45$ m, the median $med\,(h_D) = 48$ m and $rms\,(h_D) = 25.2$ m. The MLD was compared with the current reversal depth (CRD is specified as the shallowest depth where the current vector changes the sign of its rotation). The mean and median estimates for CRD appeared to be very close to those for MLD (47.9 and 48 meters, respectively), suggesting that the drift currents were mostly confined to the upper mixed layer.

• It was found that the MLD is correlated with the friction velocity u_*, and the correlation coefficient is 0.71 when u_* data were time advanced by 12 hrs. The correlation of MLD with the surface buoyancy flux J_b was weak. The ratio between h_D and the Monin–Obukhov length scale $L_{mo} = u_*^3/J_b$ based on the time shifted u_* indicates that at almost all stations $h_D/L_{MO} < 1$, suggesting the dominance of wind–induced mixing over convection. Parameterization of MLD in terms of the Ekman scale $L_f = u_*/f$ (also with time–shifted u_*) yielded the following linear dependence $h_D \approx 0.44 L_f$ (for $L_f > 30$ m) with the coefficient of determination $r^2 = 0.92$.

• The MLD was also correlated with the "stratified Ekman scale" $L_{fN} = u_*/\sqrt{f N_{pc}}$, where N_{pc} is the buoyancy frequency in the pycnocline, assuming that the growth of MLD is arrested by buoyancy when MLD reaches L_{fN}. Using L_{fN} with time shifted u_*, a linear regression of the form $h_D \approx 1.9 L_{fN}$ was obtained with reasonable statistical confidence. Given that numerical calculations show that in the steady

state MLD is about $1.7L_{fN}$, the above result suggests that the mixed layer at most stations may have achieved or come close to achieving an equilibrium state. This suggests that L_{fN} can be a good indicator for storm–induced MLD.

7.3   Turbulence within the mixing layer depth

7.3.1   Statistics of turbulence in the UQHL

• Techniques for the general processing of microstructure data –edition, despiking, calculation of falling velocity of the instrument and smoothing– were developed and compared to those recommended in the literature [mainly by Prandke *et al.* (2000)].

Mixing layer depth (h_ϵ) is defined as the layer where $\epsilon > 10^{-7}$ Wkg^{-1} and below which dissipation rapidly decreases to 10^{-7} Wkg^{-1}. Mixing and mixed layers are found to be highly correlated $[h_\epsilon = 0.97h_D$, with $r^2 = 0.96]$ because, during the cruise, the mixed upper layer was generated predominantly by active atmospheric forcing.

• **Probability distributions and state of turbulence.**   Probability distributions of the kinetic energy dissipation rate (ϵ) show that, for $z > 16$ m, it is lognormal. In the nearsurface layer, where measurements are strongly affected by waves and also possibly contaminated by ship movement, the distribution departs from lognormality. The corresponding mean and median values of ϵ are $\langle\epsilon\rangle = 2.2 \times 10^{-6}$ and $med(\epsilon) = 1.5 \times 10^{-7}$ Wkg^{-1}. Turbulent diffusivity (K_b), the gradient Richardson number (R_i) and buoyancy Reynolds number (R_{e_b}) also present a lognormal distribution. The median of the buoyancy Reynolds number $med\,(R_{e_b}) = 4000$ is high, indicating energetic turbulence within the mixing layer. The R_i distribution function also shows high probability of shear instability in the upper weakly-stratified layer, where $med(R_i) = 0.1$ and the probability of $R_i < 0.25$ is above 60%. It appears that the depth where R_i is close to 0.25 roughly corresponds to the mixing layer depth h_D, suggesting that local shear instability may play a comparable role in the turbulence generation, specifically in the lower part of the mixing layer. Diffusivity (K_b) there is in the range $10^{-2} - 10^{-1}$ m^{2}s^{-1} but it sharply decreases to $10^{-4} - 10^{-5}$ m^{2}s^{-1} at the upper boundary of the pycnocline.

7.3.2   Vertical structure of ϵ

• The microstructure data was used to estimate ϵ, and CTD and atmospheric measurements taken concurrently permitted the evaluation of buoyancy flux and surface wind stress in the upper turbulent layer at high–mid–latitudes. Momentum and buoyancy fluxes were used to explore different scalings for the vertical structure of $\epsilon(z)$. When only wind induced shear stress (the law of the wall) is considered it is found that the vertical structure of $\epsilon(z)$ is not reasonably represented, but that if buoyancy production is included, as proposed by Lombardo and Gregg (1989), fitting improves considerably. A better fitting to the data was obtained with two approaches based on the similarity theory. First, by considering a weighting factor of 0.6 for buoyancy flux (like in the original work of Monin and Obukhov, 1954) it is obtained a parameterization of the form $\epsilon(z) = 2.6\epsilon_1(z) + 0.6J_b$ where $\epsilon_1 = u_*^3/\kappa z$ is the law of the wall. Second, a very close correspondence to the data is also obtained when it is assumed that all "excessive" dissipation above ϵ_1 is due to buoyancy production of forced convection, in this case $\epsilon(z) = \epsilon_1(z) + 3.7J_b$. The factor 3.7 weighting the influence of J_b is surprisingly close to the one often used for stratified atmospheric surface layer with log–linear velocity profiles. Despite turbulent mixing in the upper layer being influenced by numerous complex dynamical processes such as Langmuir circulation and wave breaking, it appears that simple parameterizations based on similarity approaches, with some modifications, can be used to describe essential features of the dissipation profile in the upper oceanic layer.

• Assumptions behind approaches leading to $\epsilon(z) = 2.6\epsilon_1(z) + 0.6J_b$ and $\epsilon(z) = \epsilon_1(z) + 3.7J_b$ are different, however both formulas scale data reasonably well and employing them to scale dissipation in regions with substantially different hydro–meteorological conditions than those considered here should be done with caution, given the possible differences in the structure of turbulence and dynamical processes.

• The column–integrated dissipation rate int $\widetilde{\epsilon}_{int}$ over the mixing layer may account, on the average, for about 5% of the wind work at 10 m above the sea surface E_{10} (However, the ratio $\widetilde{\epsilon}_{int}/E_{10}$ varies between approximately 3 and 7%). The ratio $\widetilde{\epsilon}_{int}/E_{10}$ also shows a positive correlation with MLD, indicating the increased column averaged dissipation at a higher MLD. This calls for a rethinking of the commonly

used modeling assumption of the proportionality between the buoyancy flux due to entrainment and the rate of wind work imparted on the surface.

7.3.3   Mixing parameterization

- Different combinations of numerical values of governing parameters that are commonly used in various versions of the Munk-Anderson [1948] type formulas were analyzed to parameterize the diffusivity K_b as a function of R_i. For the turbulent Prandtl number, an inverse function on R_i ($P_{r_t} = \alpha_t = \left(1 - \frac{R_i}{R_{i\beta}}\right)^{-r}$ was adopted with $r = 1$) and the critical $R_{i\beta} = 0.05$ or 0.1. The exponent p in formula $K_b = \left(K_0 / \left(1 + \frac{R_i}{R_{icr}}\right)^p\right) P_{r_t}^{-1}$, which is used to parameterize the eddy viscosity, was assigned a value of 0.5 by different authors. It was shown that $p = 1$ makes $K_M \sim \epsilon/N^2$ at $R_i >> R_{icr}$, and the Ozmidov scale serves as the main turbulent length–scale for such a dependence of $K_b(R_i)$. In non–stratified shear flow, $p = 1$ leads to the Tchen (1954) shear scales. These links give theoretical support to $p = 1$ compared to the other mostly empirical values of p. It was also suggested that $p = 2/3$ specifies another turbulent length scale $L_R = (\epsilon/NS_h)^{1/2}$ that separates the inertial and production subranges when they appear in spectra of turbulent kinetic energy. The use of $p = 2/3$ and/or $p = 1$ links $K_b(R_i)$ to specific spectral structures of turbulent fluctuations, when more traditional values of p (0.5, 1.5, and 2) do not. The best fit to the experimental data was obtained with $R_{icr} = 0.1$ and $R_{i\beta} = 0.1$ for $p = 1$, but $R_{i\beta} = 0.05$ works better for $p = 2/3$.

- When turbulence in the upper layer is mainly driven by wind stress, the diffusivity K_b can be specified using friction velocity at the sea surface, which leads to the well–known $K_{sf}(z) = \kappa u_* z^{-1}$. A simple parameterization of K_b ($\frac{K_b}{\kappa u_* z} = 1 - \frac{R_i}{R_{icr}} + \frac{5\times10^{-4}}{\kappa u_{*z}(1-5R_i)^{2.5}}$) gives a successful fit to the bin–median estimates of the normalized diffusivity with statistical confidence ($r^2 > 0.8$).

BIBLIOGRAPHY

Anis, A. and J. N. Moum (1995). "Surface wave–turbulence interactions: Scaling $\epsilon(z)$ near the sea surface." *J. Phys. Oceanogr.* 25(9), 2025–2045.

Appel, J. R. (1987). *Principles of Ocean Physics.* San Diego, CA: Academic Press.

Batchelor, G. K. (1967). *An Introduction to Fluid Dynamics.* Oxford, England: Cambridge University Press.

Bathen, K. H. (1972). "On the seasonal changes in the depth of the mixed layer in the North Pacific Ocean." *J. Geophys. Res.* 77, 7138–7150.

Beljaars, A.C.M. (1994). "The parameterization of surface fluxes in large scale models under free convection." *Quert. J. Roy. Meteor. Soc.* (121), 255–270.

Berliand, M. and T. Berliand (1952). "Determining the net long–wave radiation of the earth with consideration of the effect of cloudiness." *Isv. Akad. Nauk. SSSR Ser Geofis.* 1, 64–78.

Bolding, K., H. Burchard, T. Pohlmann, and A. Stips (2002). "Turbulent mixing in the Northern North Sea: A numerical model study." *Continental Shelf Res.* 22(18–19), 2707– 2724.

Brainerd, K. E. and M.C. Gregg (1995). "Surface mixed and mixing layer depths." *Deep–Sea Res.* 42(9), 1521–1543.

Broecker, W. S. (1987). "The biggest chill." *Natural History Magazine* 97, 74–82.

Bunker, A. F. (1976). "Computation of surface energy and annual air–sea interaction cycles of the North Atlantic Ocean." *Mon. Weather Rev.* 104, 1122–1140.

Burchard, Hans (2002). *Applied Turbulence Modelling in Marine Waters*, Volume 100 of *Lecture Notes in Earth Sciences*. Berlin. Heidelberg: Springer–Verlag.

Burchard, H., K. Bolding, T.P. Rippeth, A. Stips, J.H. Simpson, and J. Sundermann (2002). "Microstructure of turbulence in the Northern North Sea: A comparative study of observational and model simulations." *J. Sea Res.* 47(3-4), 223–238.

Bussinger, J.A., J.C. Wyngaard, Y. Issumi, and E.F. Bradley (1971). "Flux profile relationship in the atmospheric surface layer." *J. Atmos. Sci.* 28, 181–189.

Caldwell, D.R. and J.N. Moum (1995). "Turbulence and mixing in the ocean." *Rev. Geophys.* 33, 1385–1394.

Charnock, H. (1955). "Wind stress on a water surface." *Q. J. R. Meteorol. Soc.* 81, 639.

Chen, D., A. J. Busalacchi, and L. Rothstein (1994). "The roles of vertical mixing, solar–radiation, and wind stress in a model simulation of the sea–surface temperature seassonal cycle in the Tropical Pacific Ocean." *J. Geophys. Res.* 99(C10), 20345–20359.

Chereskin, T. K. and D. Roemmich (1991). "A comparison of measured and wind–derived Ekman transport at 11 n in the Atlantic Ocean." *J. Phys. Oceanogr.* 21(6), 869–878.

DeCosmo, J., K.B. Katsaros, S.D. Smith, R.J. Anderson, W.A. Oost, K. Bumke, and H. Chadwick (1996). "Air–sea exchange of water vapour and sensible heat: The humidity exchange over sea (HEXOS) results." *J. Geophys. Res.* 101(C5), 12001–12006.

Denman, K. L. (1994). "Scale–determining biological–physical interactions in oceanic food webs." In Paul S. Giller, Alan G. Hildrew, and David G. Raffaelli, eds., *Aquatic Ecology: Scale, Pattern and Process*, Aquatic Ecology: Scale, Pattern and Process, Oxford, UK, pp. 377–402. University College: Blackwell Scientific.

Dickson, R. R. and J. Brown (1994). "The production of North Atlantic deep water: Sources, rates, and pathways." *J. Geophys. Res.* 99(C6), 12319–12341.

Dillon, T. M., J.G Richman, C. G. Hansen, and M. D. Pearson (1981). "Near–surface turbulence measurements in a lake." *Nature* 290, 390–392.

Doneland, M.A. (1990). "Air–sea interaction." In B. LeMehaute and D.M. Hanes, eds., *The Sea*, pp. 239–299. J. Wiley and Sons.

Donlon, C. J., P. J. Minnett, C. Gentemann, T. J. Nightingale, I. J. Barton, B. Ward, and M. J. Murray (2002). "Toward improved validation of satellite sea surface skin temperature measurements for climate research." *J. Climate* 15, 353–369.

Donlon, C. J. and I.S. Robinson (1997). "Observations of the thermal skin in the Atlantic Ocean." *J. Geophys. Res.* 102, 18585–18606.

Dyer, A.J. (1974). "A review of flux–profile relations." *Boundary Layer Meteorology* (7), 363–372.

Ehret, L.L. and J.J. O'brien (1994). "Scales of the North Atlantic wind stress curl determinated from the comprehensive ocean–atmospheric data set." *J. Geophys. Res.* (94), 831–841.

Ewing, G. and E. D. McAlister (1960). "On the thermal boundary layer of the ocean." *Science* 131(3410), 1374–1376.

Fairall, C. W., E. F. Bradley, D. P. Rogers, J. B. Edson, and G. S. Young (1996). "Bulk parameterization of air sea fluxes for tropical ocean–global atmosphere coupled–ocean atmosphere response experiment." *J. Geophys. Res.* 101, 3747–3764.

Fernando, H.J.S. (1991). "Turbulent mixing in stratified fluids." *Ann. Rev. Fluid Mech.* 23, 455–493.

Frisch, U. (1995). *Turbulence: The Legacy of A.N. Kolmogorov.* Cambridge University Press.

Fung, I. Y., D. E. Harrison, and A. A. Lacis (1984). "On the variability of the net longwave radiation at the ocean surface." *Rev. Geophys. Space Phys.* (22), 177–103.

Gargett, A.E., P.J. Hendricks, T.B. Sanford, T.R. Osborn, and A.J. Williams (1981). "A composite spectrum of vertical shear in the upper ocean." *J. Phys. Oceanogr.* 11(9), 1258–1271.

Gargett, A. and J. Marra (2002). "Effects of upper ocean physical processes (Turbulence, Advection and Air–Sea Interaction) on oceanic primary production." In James J. McCarthy, Allan R. Robinson, and Brian J. Rothschild, eds., *The Sea*, Volume 12 of *The Sea*, Chapter 2, pp. 19–49. New York, NY: John Wiley and Sons, Inc.

Gargett, A. E (1989). "Ocean turbulence." *Ann. Rev. Fluid Mech* (21), 419—452.

Garrat, J.R. (1992). *The Atmospheric Boundary Layer.* New York: Cambridge Univ. Press.

Garret, C. (1993). "A stirring tale of mixing." *Nature* (364), 670–671.

Garret, C., P. MacCready, and P. Rhines (1993). "Boundary mixing and arrested Ekman layers: Rotating, stratified flow near a sloping boundary." *Ann. Rev. Fluid Mech.* 25, 291–323.

Geernaert, G.L. (1990). "Bulk parameterization for the wind stress and heat fluxes." In G.L. Geernaert and W.J. Plant, eds., *Surface Waves and Fluxes, Vol.*, pp. 91–172. Norwell, Mass.: Klwer Academic.

Gibson, C. H. (1999). "Fossil turbulence revisited." *Journal of Marine Systems* 21, 147–167.

Gill, A. E. (1982). *Atmosphere–Ocean Dynamics.* London and New York: Academic Press.

Godfrey, J.S. and A.C.M. Beljaars (1991). "On the turbulent fluxes of buoyancy, heat and moisture at the air–sea interface at low wind speeds." *J. Geophys. Res.* (96), 22043–22048.

Grant, H.L., R.W. Stewart, and A. Moilliet (1961). "Turbulence spectra from a tidal channel." *J. Fluid Mech.* 12, 241–263.

Grant, H. L., B. S. Hughes, W. M. Voguel, and A. Moilliet (1968). "Some observations of the occurrence of turbulence in and above the thermocline." *J. Fluid Mech.* 34, 1443–1448.

Gregg, M.C. (1987). "Diapycnal mixing in the thermocline: A review." *J. Geophys. Res.* 92(C5), 5249–5286.

Gregg, M.C. (1991). "The study of mixing in the ocean: A brief history." *Oceanography* 4(1), 39–45.

Gregg, M. C. (1999). "Estimation and geography of diapycnal mixing in the ocean." In *Physical Processes in Lakes and Oceans*, pp. 305–338. AGU Publ.

Gregg, M. C., D. P. Winkel, T. B. Sanford, and Peters H (1996). "Turbulence produced by internal waves in the ocean thermocline at mid and low latitudes." *Dyn. Atmos. Oceans* 24, 1–14.

Gurvich, A. C. and A. M. Yaglom (1966). "Breakdown of eddies and probability distribution for small–scale turbulence." *Phys. Fluids* 10, 59–65.

Halpern, D., W. Knauss, O. Brown, M. Freilich, and F. Wentz (1994, March). "An atlas of monthly distributions of SSM/I surface wind speed, ARGOS buoy 2

drift, AVHRR/2 sea surface temperature, AMI surface wind components, and ECMWF surface wind components during 1992." Technical Report 94–4, Jet Propulsion Lab.

Hamming, R. W. (1983). *Digital Filters, 2nd. Ed.* Englewood Cliffs, New Jersey: Prentice–Hall, Inc.

Hellerman, S. and M. Rosenstein (1983). "Normal monthly wind stress over the world ocean with error estimates." *J. Phys. Oceanogr.* (3), 1093–1104.

Henderson-Seller, B. (1982). "A simple formula for vertical eddy diffusion coefficients under conditions of nonneutral stability." *J. Geophys. Res.* 87(C4), 5860–5864.

Huang, R. X. and S. Russell (1994). "Ventilation of the subtropical north Pacific." *J. Phys. Oceanogr.* 24, 2589–2605.

Hunt, J.C.R., N. D. Sandham, J. C. Vassilicos, B. E. Launder, P. A. Monkewitz, and G. F. Hewitt (2001). "Developments in turbulence research: A review based on the 1999 programme of the Isaac Newton Institute, Cambridge." *J. Fluid Mech.* 436, 353–391.

Imberger, J. (1985). "The diurnal mixed layer." *Limnol. and Oceanogra.* 30(4), 737–770.

Imberger, J. and G.N. Ivey (1991). "On the nature of turbulence in a stratified fluid. Part 2: Application to lakes." *J. Phys. Oceanogr.* (21), 659–680.

Inall, M. E., T. P. Rippeth, and T. J. Sherwin (2000). "Impact of nonlinear waves on the dissipation of internal tidal energy at a shelf break." *J. Geophys. Res.* 105(C4), 8687–8705.

Kantha, L. H. and C. A. Clayson (2000a). *Numerical Models of Oceans and Oceanic Processes.* San Diego: Academic Press.

Kantha, L. H. and C. A. Clayson (2000b). *Small Scale Processes in Geophysical Fluid Flows*, Volume 67 of *International Geophysics.* San Diego: Academic Press.

Kara, A.B., P. A. Rochford, and H.E. Hulburt (2000). "An optimal definition for ocean mixed layer depth." *J. Geophys. Res.* 105(C7), 16803–16821.

Kara, A. B., P. A. Rochford, and H. E. Hurlburt (2003). "An optimal definition for ocean mixed layer depth." *J. of Geophys. Res.* 105, 16803–16821.

Kelly, K. A. and B. Qiu (1995). "Heat flux estimates for the western north Atlantic: Part I, assimilation of satellite data into mixed layer model." *J. Phys. Oceanogr.* 25, 2344–2360.

Kit, E., E. Strang, and H.J.S. Fernando (1997). "Measurements of turbulence near shear–free density interfaces." *J. Fluid Mech.* (334), 293–314.

Kolmogorov, A. N. (1941a). "Energy dissipation in locally isotropic turbulence." *Dokl. Akad. Nauk. SSSR* 32, 19–21. (in Russian).

Kolmogorov, A. N. (1941b). "Local structure of turbulence in an incompressible fluid at very high reynolds number." *Dokl. Akad. Nauk SSSR* 30, 299–303. (in Russian).

Korchashkin, N. N. (1976). "Statistics of fine structure of hydrophysical fields in the ocean." *Okeanologiya* 14, 602–607. in Russian.

Kraus, E.B. and J.A. Businger (1994). *Atmosphere–Ocean Interactions*, Volume 27 of *Oxford Monographs on Geology and Geophysics*. Oxford: Oxford University Press.

Kumar, P. and E. Foufoula-Georgiou (1997). "Wavelet analysis for geophysical applications." *Review of Geophysics* 35(4), 385–412.

Kundu, P. K. (1990). *Fluid Mechanics*. San Diego, CA: Academic Press.

Lamb, P.J. (1984). "On the mixed layer climatology of the north and tropical Atlantic." *Tellus* 36, 292–305. Ser. A.

Large, W. G. and S. Pond (1982). "Sensible and latent heat flux measurements over the ocean." *J. Phys. Oceanogr.* 12, 464–482.

Lass, H. U., H. Prandke, and B. Liljebladh (2003). "Dissipation in the baltic proper during winter stratification." *J. Geophys. Res.* 108(C6). 3187, doi:10.1029/2002JC001401.

Lazier, J.R.N. and D.G. Wright (1993). "Annual velocity variations in the Labrador Current." *J. Phys. Oceanogr.* 23(4), 659–678.

Ledwell, J.R., E.T. Montgomery, K.L. Polzin, L.C. St. Laurent, R.W. Schmitt, and J.M. Toole (2000). "Evidence for enhanced mixing over rough topography in the abyssal ocean." *Nature* 403, 179–182.

Lentz, S.J. (1992a). "The surface boundary layer in coastal upwelling regions." *J. Phys. Oceanogr.* 22(12), 1517–1539.

Lentz, S. J. (1992b). "The surface boundary layer in coastal upwelling regions." *J. Phys. Oceanogr.* 23(4), 1517–1539.

Lesieur, M. (1997). *Turbulence in Fluids* (3th. ed.), Volume 40 of *Fluid Mechanics and its Applications*. Dordrecht: Kluwer Academic Publ.

Levitus, S. (1982). "Climatological atlas of the world ocean." In *NOAA Prof. Pap. 13*, pp. 173. Washington, D. C.: U.S. Govt. Print. Off.

Lewis, M. R., M. Carr, G. Feldman, W. Esaias, and C. McClain (1990). "Influence of penetrating solar radiation on the heat budget of the Equatorial Pacific Ocean." *Nature* 347, 543–544.

Linden, P.F. (1979). "Mixing in stratified fluids." *Geophys. Astrophys. Fluid Dyn.* 13, 3–23.

Lombardo, C.P. and M.C. Gregg (1989). "Similarity scaling of viscous and thermal dissipation in a convecting surface boundary layer." *J. Geophys. Res.* (94), 6273–6284.

Lorke, A. (1998). "Investigation of turbulent mixing in shallow lakes using temperature microstructure measurements." *Aquat. Sci.* 60, 210–219.

Lozovatsky, I.D. (1996). "Turbulence decay in stratified and homogeneous marine layers." *Dyn. Atmosph. Oceans* 24, 15–25.

Lozovatsky, I.D., A.S. Ksenofontov, and H.S.J. Fernando (2000). "The formation of step–like structure in near surface and near–bottom pycnoclines." In G. Lawrence, R. Pieters, and N. Yonemitsu, eds., *Stratified Flows II*, Vancouver, Canada, pp. 1215–1220. Univ. of British Columbia.

Lozovatsky, I. D., A. L. Berestov, and A. S. Ksenofontov (1998). "Phillips theory of turbulence generated fine–structure: Numerical and stochastic modeling." In *Abstracts of Johns Hopkins Conference in Environmental Fluid Mechanics*, Baltimore, MD, pp. 102–103.

Lozovatsky, I. D., T. M. Dillon, A. Yu. Erofeev, and V. N. Nabatov (1999). "Variations of thermohaline and turbulent structure on the shallow black sea shelf in the beginning of autumn cooling." *J. Marine Systems* 21, 255–282.

Lozovatsky, I. D., A. S. Ksenofontov, A. Yu. Erofeev, and C. H. Gibson (1993). "Modeling of evolution of vertical structure in the upper ocean by atmospheric forcing and intermittent turbulence in the pycnocline." *J. Marine Systems* 4, 263–273.

Lukas, R. and E. Lindstrom (1991). "The mixed layer of the Western Equatorial Pacific." *J. Geophys. Res* 96, 3343–3357.

Luketina, D. A. and J. Imberger (2001). "Determining turbulent kinetic energy dissipation from batchelor curve fitting." *J. Atmos. Oceanic Technol.* 18, 100–113.

MacIntyre, F. (1974). "The top millimeter of the ocean." *Sci. Am.* 230, 62–77.

Makin, V.K. (1996). "Parameterization of sensible heat and moisture fluxes." Technical Report KNMI MEMO WM-96-21, De Bilt.

Makin, V.K. (1999). "A note on wind speed and sea state dependence of the heat exchange coefficient." *Boundary–Layer Metorology* 91(1), 127–134.

Marotzke, J. (1997). "Boundary mixing and the dynamics of the three–dimensional thermohaline circulation." *J. Phys. Oceanogr.* 27, 1713–1728.

Marshall, J., H. Jhonson, and J. Goodman (2001). "A study of the interaction of the North Atlantic Oscillation with ocean circulation." *J. Climate* (14), 1399–1421.

Marshall, J. and F. Schott (1999). "Observations, theory and models." *Rev. Geophys.* 37, 1–64.

Martin, P.J. (1985). "Similation of mixed layer at OWS novembre and papa with several models." *J. Geophys. Res.* 90, 903–916.

McPhee, M.G. (1990). "Small scale processes." In W. Smith, ed., *Polar Oceanography*, pp. 287–334. San Diego: Academic Press.

McPhee, M.G., S.F. Ackley, P. Guest, B.A. Huber, D.G. Martinson, J.H. Morison, R.D. Muench, L. Padman, and T.P. Stanton (1996). "The Antartic Zone Flux Experiment." *Bull. American Meteorol. Soc.* 77(6), 1221–1232.

McPhee, M. G. and T. P. Stanton (1996). "Turbulence in the statically unstable oceanic boundary layer under artic leads." *J. Geophys. Res. -Oceans* 101(C3), 6409–6428.

McPhee-Shaw, E. and E. Kunze (2001). "Boundary layer intrusions from a sloping bottom: A mechanism for generating intermediate nepheloid layers." *J. Geophys. Res.* 107(10), 10.1029.

Miles, J.W. (1961). "On the stability of heterogeneous shear flows." *J. Fluid Mech.* 10, 496–515.

Miller, J. R. (1976). "The salinity effect in a mixed layer ocean model." *J. Phys. Oceanogr.* 6, 29–35.

Mohammad, R. and J. Nilsson (2004). "The role of diapycnal mixing for the equilibrium response of thermohaline circulation." *Ocean Dynamics* 54, 54–65.

Monin, A.S. and R.V. Ozmidov (1985). *Turbulence in the Ocean.* New York: D. Reidel Publishing.

Monin, A.S., A.M. Obukhov (1954). "Basic turbulent mixing laws in the atmospheric surface layer." *Trudy Geofiz. Inst.* 24(151), 163–187.

Monin, A. S. and A. M. Yaglom (1981). *Statistical Fluid Mechanics: Mechanics of Turbulence.* Mass.: MIT Press.

Monterey, G. and S. Levitus (1997). *Seasonal Variability of Mixed Layer Depth for the World Ocean,* Volume 14 of *NOAA Atlas NES–DIS.* Washington, D. C.: U. S. Govt. Print. Off.

Monti, P., H.J.S. Fernando, M. Princevac, W.C. Chan, T.A. Kowalewski, and E. R. Pardyjak (2002). "Observations of flows and turbulence in the nocturnal boundary layer over a slope." *J. Atmospheric Sci.* 59(17), 2513–2534.

Moore, G. W. K., M. C. Reader, J. York, and S. Sathiyamoorthy (1996). "Polar lows in the labrador sea. a case study." *Tellus* 48, 17–40.

Moum, J. N. (1996). "Energy–containing scales of turbulence in the ocean thermocline." *J. Geophys. Res.* 101, 14095–14109.

Moum, J. N., D. R. Caldwell, and C. A. Paulson (1989). "Mixing in the equatorial surface layer and thermocline." *J. Geophys. Res.* 94, 2005–2022.

Moum, J. N., M. C. Gregg, R. C. Licen, and M. E. Carr (1995). "Comparison of turbulence kinetic energy dissipation rate estimates from two ocean microstructure profiles." *J. Atmos. Oceanic Technol.* 12(2), 346–365.

Moum, J. N. and R. G. Lueck (1985). "Causes and implications of noise in oceanic dissipation measurements." *Deep–Sea Res.* 32(4), 379–390.

Müller, P. and C. Garrett (2004). "Near-boundary processes and their parameterization." . *Oceanography* 17(1), 107–116.

Munk, W. (1966). "Abyssal recipes." *Deep-Sea Res.* 13, 707–730.

Munk, W.H. and E.R. Anderson (1948). "Notes on the theory of the thermocline." *J. Mar. Res.* 3, 276–295.

Nashmyth, P. W. (1970). *Oceanic Turbulence, Ph. D. Dissertation.* Ph.D. thesis, University of British Columbia, Vancouver, Canada.

Navier, L. M. H. (1822). "Memorie sur le loi du mouvement des fluides." *Mémoire de l'Académie des Sciences de l'Institut de France* 6, 389–440.

Nihoul, J.C.J. (1980). *Marine Turbulence: Proceedings of the 11th International Liege Colloquium on Ocean Hydrodynamics.* New York: Elsevier Scientific Publishing Company.

Niiler, P. P. and E. B. Kraus (1977). *One–Dimensional Models.* Modeling and Prediction of the Upper Layers of the Ocean. New York: Pergamon.

Oakey, N.S. and J.A. Elliot (1982). "Dissipation within the surface mixed layer." *J. Phys. Oceanogr.* (12), 171–185.

Oakey, N. S. (1985). "Statistics of mixing parameters in the upper ocean during JASIN phase II." *J. Phys. Oceanogr.* 15, 1662–1675.

Obata, A., J. Ishazaka, and M. Endoh (1996). "Global verification of critical depth theory for phytoplankton bloom with climatological in situ temperature and satellite color data." *J. Geophys. Res.* 101, 20657–20667.

Osborn, T. (1986). "Turbulence in the upper layer." In J.D. Burnon, P.G. Brewer, and R. Chesselet, eds., *Dynamic Processes in the Chemistry of the Upper Ocean*, New York, pp. 93–105. Plenum Press.

Osborn, T. R. (1974). "Vertical profiling of velocity microstructure." *J. Phys. Oceanogr.* 4, 109–115.

Pacanowski, R.C. and S.G.H. Philander (1981). "Parametrization of vertical mixing in numerical models of tropical oceans." *J. Phys. Oceanogr.* 11, 1662–1675.

Padman, L. and T. M. Dillon (1991). "Turbulent mixing near the Yermak Plateau during the coordinate eastern Artic experiment." *J. Geophys. Res.* 10, 4769–4782.

Paka, V. T., V. N. Nabatov, I. D. Lozovatsky, and T. M. Dillon (1999). "Ocean microstructure measurements by BAKLAN and GRIF." *J. Atmos. Oceanic Technol.* 16, 1519–1532.

Panchev, S. and D. Kesich (1969). "Energy spectrum of isotropic turbulence at large wave–numbers." *Comptes rendus de l'acadmie des Sciences* 22, 627–630.

Panofsky, H.A. and J.A. Dutton (1984). *Atmospheric Turbulence.* New York: Wiley–Interscience.

Payne, R. E. (1972). "Albedo of the sea surface." *J. Atm. Sci.* 29, 959–970.

Pelegri, J.L. and G.T. Csanadi (1994). "Dyapicnal mixing in western boundary currents." *J. Geophys. Res.* 99, 18275–18304.

Peters, H., M. C. Gregg, and J. M. Tool (1989). "Meridional variability of turbulence through the equatorial undercurrent." *J. Geophys. Res.* 94, 18003–18009.

Peters, H., M. C. Gregg, and J. M. Toole (1988). "On the parameterization of equatorial turbulence." *J. Geophys. Res.* 93, 1199–1218.

Phillips, O.M. (1991). "The Kolmogorov spectrum and its oceanic cousins: A review." *Proc. R. Soc. Lond.* A, 434–438.

Pickard, G.L. and W.J. Emery (1990). *Descriptive Physical Oceanography, 5th Edition.* New York: Pergamon Press.

Piera, J., E. Roget, and J. Catalan (2001). "Turbulent patch identification in microstructure profiles: A method based on wavelet denoising and thorpe displacement analysis." *J. Atmos. Oceanic Technol.* 19, 1390–1402.

Pollard, R.T., P.B. Rhines, and O.R.Y. Thompson (1973). "The deepening of the wind–mixed layer." *Geophys. Fluid Dynamics* (3), 381–404.

Pollard, R. T. and J. Read (1989). "A method for calibrating shipmounted acoustic doppler profilers and the limitations of gyro compasses." *J. Atmosp. Oceanic Technol.* 6, 859–865.

Prandke, H., K. Holtsh, and A. Stips (2000). "MITEC technology development: The microstructure–turbulence measuring system MSS." Tech. Rep. EUR 19733 EN, Ispra Joint Research Center, European Comission, Ispra, Italy.

Prandke, H. and A. Stips (1998). "Test measuremente with an operational microstructructure–turbulence profiler: Detection limit of dissipation rates." *Aquatic Sci.* 60, 191–209.

Prandke, H. and H. Stips (1996). "Investigation of microstructure and turbulence in marine and limnic waters using the MST profiler." Tech. Note I.96.87, Ispra Joint Research Center, European Comission, Ispra, Italy.

Press, W. H., B. P. Flannery, S. A. Teukolsky, and W. T. Veteerling (1990). *Numerical Recipes. The Art of Scientific Computing.* Cambridge University Press.

Price, J. E., R. A. Weller, and R. Pinkel (1986). "Diurnal cycling: Observations and Models on the Upper Ocean Response to Diurnal Heating, Cooling and Wind Mixing." *J. Geophys. Res.* 91, 8411–8427.

Qu, P. (2003). "Mixed layer heat balance in the Western North Pacific." *J. Geophys. Res.* 108(C7), 3242. doi:10.1029/2002JC0015326.

Rahmstorf, S. (2003). "The Current Climate." *Nature* 421, 699.

Reynolds, O. (1895). "On the dynamical theory of incompressible viscous fluids and the determination of the criterion." *Phil. Trans. R. Soc. Lond.* 186, 123–164.

Richards, K.J., M.E. Inall, and N.C. Wells (1995). "The diurnal mixed layer and upper ocean heat budget in the western equatorial pacific." *J. Geophys. Res.* 100, 6865–5879.

Richman, J. and C. Garrett (1977). "The transfer of energy and momentum by the wind to the surface mixed layer." *J. Phys. Oceanogr.* (7), 876–881.

Roget, E., J. M. Figueroa, and I.D. Lozovatsky (2004). "From small–scale shear measurements to the dissipation rates in natural waters,." In A. Babiano, P. Fraunie, J.M. Redondo, and P. Basiliscos, eds., *Environmental Fluid Dynamics*, Barcelona. CIMNE. (In press).

Ruddick, B., A. Anis, and K. Thompson (2000). "Maximum likelihood spectral fitting: The batchelor spectrum." *J. Atmos. Oceanic. Technol.* 17, 1541–1555.

Sanchez, X. (2001). "Determining turbulent kinetic energy dissipation rate from thermal spectra." Master's thesis, University of Girona. 66p.

Saunders, P. M. (1967). "The temperature at the ocean–air interface." *J. Atmos. Sci.* 24, 269–273.

Schmitt, R.W. (1994). "Double diffusion in oceanography." *Annual Review of Fluid Mechanics* 26, 255–285.

Schneider, N. and P. Muller (1990). "The meridional and seasonal structures of the mixed–layer depth and its diurnal amplitude observed during the Hawaii–to–Tahiti Shuttle Experiment." *J. Phys. Oceanogr.* 20(9), 1395–1404.

Shay, T. J. and M. C. Gregg (1984). "Convectively driven turbulent mixing in the upper ocean." *Natur* 310, 282–285.

Simpson, J. H., W. R. Crawford, T. R. Rippeth, A. R. Campbel, and J. V. S. Cheok (1996). "The vertical structure of turbulent dissipation in shelf seas." *J. Phys. Oceanogr.* 26, 1579–1590.

Smith, S.D. (1980). "Wind stress and heat flux over the ocean in gale force winds." *J. Geophys. Res.* (10), 709–726.

Smith, S.D. (1988). "Coefficients for sea surface wind stress." *J. Geophys. Res.* (93), 15467–15472.

Smith, S. D:, C. W. Fairall, G. L. Geernaert, and L. Hasse (1996). "Air–sea fluxes: 25 years of progress." *Boundary–Layer Meteorol.* 78, 247–290.

Smyth, W.D. and J.N. Moum (2000). "Anisotropy of turbulence in stably stratified mixing layers." *Phys. of Fluids* (12), 1343–1362.

Smyth, W.D., P.O. Zavialov, and J.N. Moum (1997). "Decay of turbulence in the upper ocean following sudden isolation from surface forcing." *J. Phys. Oceanogr.* 27(5), 810–822.

Soloviev, A. R., R. Lukas, and P. Hacker (2001). "An approach to parameterization of oceanic turbulent boundary layer in the western pacific warm pool." *Journal of Geophysical Research* 106(C3), 4421–4435.

Soloviev, A. V., N. V. Vershinsky, and V. A. Bezverchnii (1988). "Small–scale turbulence measurements in the thin surface layer of the ocean." *Deep-Sea Res.* 35, 1859–1874.

Spall, M.A. (1991). "Diagnostic study of the wind and buoyancy–driven North Atlantic circulation." *J. Geophys. Res.* 96, 18509–18518.

St. Laurent, L.C., J.M. Toole, and R.W. Schmitt (2001). "Buoyancy forcing by turbulence above rough topography in the abyssal Brazil basin." *J. Phys. Oceanogr.* 31, 3476–3495.

Stewart, R. W. and H. L. Grant (1962). "Determination of the rate of dissipation of turbulent energy near the sea surface in presence of waves." *J. Geophys. Res.* 67, 3177–3180.

Stips, A. H., H. Burchard, K. Bolding, and W. Eifter (2002). "Modeling of convective turbulence with a two–equation $\kappa - \epsilon$ turbulence closure scheme." *Ocean Dynamics* 52, 153–168.

Stokes, G.G. (1845). "On the theories of internal friction of fluid in motion, and of the equilibrium and motion of elastic solids." *Trans. Cambridge Philos. Soc.* 8, 287–305.

Storch, H. Von and F. W. Zwiers (1999). *Statistical Analysis in Climate Research.* Cambridge University Press.

Stull, R.B. (1988). *An Introduction to Boundary Layer Meteorology.* Dordrecht/Boston/London: Kluwer Acad. Publish. 666pp.

Talley, L. D. (1996). "North atlantic circulation, reviewed for the CNLS conference." *Physica D* 98, 625–646.

Tchen, C.M. (1954). "Transport processes as foundations of the heisenberg and obukhoff theories of turbulence." *Phys. Rev* 93(4), 4–14.

Tennekes, H. and J.L. Lumley (1972). *A First Course on Turbulence.* Cambridge, MA: MIT Press.

Tereshchenkov, V. P., S. M. Shapovalov, S. A. Dobrolyubov, and E. G. Morozov (2002). "Cruise 9 of R/V akademikk ioffe." *Oceanology* 42(2), 298–301.

Terray, E.A., M.A. Donelan, Y.C. Agrawal, W.M. Drennan, K.K. Kahma, A.J. Williams III, P.A. Hwang, and S.A. Kitaigorodski (1996). "Estimates of kinetic energy dissipation under breaking waves." *J. Phys. Oceanogr.* 26(5), 792–807.

Thompson, R. (1976). "Climatological models of the surface mixed layer of the ocean." *J. Phys Oceanogr.* 6, 496–503.

Thorpe, S. A. (1999). "A comparisom of stable boundary layer in the ocean and the atmosphere." *Boundary–Layer Meteorology* 90, 521–528.

Toorman, E.A. (2000). "Stratification in fine–grained sediment–laden turbulent flows." In G. Lawrence, R. Pieters, and N. Yonemitsu, eds., *Stratified Flows II*, Vancouver, Canada, pp. 945–950. Univ. of British Columbia.

Tritton, D. J. (1989). *Physical Fluid Dynamics, 2nd. Ed.* Oxford, England: Clarendon Press.

Ueda, H., S. Mitsumoto, and S. Komori (1981). "Buoyancy effects on the turbulenct transport processes in the lower atmosphere." *Q.J.R. Meteorol. Soc.* 107, 561–578.

Wagner, R. G. (1996). "Decadal scale trends in mechanisms controlling meridional sea surface temperature gradients in the tropical Atlantic." *J. Geophys. Res.* 101, 16683–16694.

Weatherly, G.L. and P.L. Martin (1978). "Structure and dynamics of oceanic bottom boundary–layer." *J. Phys. Oceanogr.* 8(4), 557–570.

Webb, E. K., G.I. Pearman, and R. Leuning (1980). "Correction of flux measurements for density effects due to heat and water vapour transport." *Quart. J. Roy. Met. Soc.* 106, 85–100.

Wijffels, S. E., E. Firing, and H. L. Bryden (1994). "Direct observations of the ekman balance at 10 n in the pacific." *J. Phys. Oceanogr.* 24, 1666–1679.

Willebrand, J. (1978). "Temporal and spatial scales of the wind field over the North Pacific and North Atlantic." *J. Phys. Ocenogr.* (8), 1080–1094.

Woodcock, A. H. and H. Stommel (1947). "Temperature observed near the surface of a fresh water pond at night." *J. Met,* 4, 102–103.

Worthington, L.V. (1981). "The water masses of the world ocean: Some results of a fine–scale census." In B.A. Warren and C. Wunsch, eds., *Evolution of Physical Oceanography*, Chapter 2, pp. 42–69. Boston, MA: MIT Press.

Wyngaard, J.C. (1992). "Atmospheric turbulence." *Annual Review of Fluid Mechanics* (24), 205–233.

Yamazaki, H., H.L. Mackas, and K.L. Denman (2002). "Coupling small–scale physical processes with biology." In James J. McCarthy, Allan R. Robinson, and

Brian J. Rothschild, eds., *The Sea*, Chapter 3, pp. 51–112. New York, NY: John Wiley and Sons, Inc.

Yamazaki, H. and T. Osborn (1993). "Direct estimation of heat flux in a seasonal thermocline." *J. Phys. Oceanogr.* 23, 503–516.

Zilitinkevich, S. S. and I. N. Esau (2003). "On integral measures of the neutral barotropic planetary boundary layer." *Boundary–Layer Meteorology* 104(3), 371–379.

Convicciones Personales

- Humano soy, nada de lo humano me es ajeno. Terencio P. (190-159 A. C.)

- La construcción de la Comunidad Europea es un experimento social maravilloso, sobre todo si no olvidamos que apenas ayer –sesenta años son nada en la escala histórica– se mataban unos a otros. Aprender a convivir les ha costado sesenta millones de vidas. Ojalá que el lado positivo del ejemplo cunda.

- En México, mi país, la injusticia y la desigualdad son verdades irrefutables. El abismo entre pocos que lo tienen todo y muchos que no tienen nada es cada vez más insalvable.

- Aunque mucho hay de cierto cuando se dice que la injusticia en México se gestó en 300 años de coloniaje español y 200 de agresiones repetidas de otros estados como Estados Unidos de Norteamérica y Francia entre los más visibles, no es menos cierto que ya deberíamos de haber encontrado nuestro camino.

- Ese camino pasa necesariamente por la educación y no pasa por las políticas delirantes que hasta ahora han aplicado todos los que nos han gobernado, con dos luminosas excepciones: Benito Juárez y Lázaro Cárdenas.

- Continúa vigente la frase: "México viene padeciendo hace ya algunos años una crisis que se agrava día con día; pero como en los casos de enfermedad mortal en una familia, nadie habla del asunto, o lo hace con un optimismo trágicamente irreal. Y, como de costumbre, todos los grupos políticos continúan obrando guiados por los fines más inmediatos, sin que a ninguno parezca importarle el destino final del País". Daniel Cosío Villegas, 1946.

- Tierra y Libertad. La tierra debe se ser para quien la trabaja. ¡Zapata Vive!, ¡la lucha sigue!...¡No termina nunca!.

- Un día llegará en que los únicos ejércitos que existan sean de trabajadores, de maestros, de niños camino a la escuela, de obreros y de campesinos. Pancho Villa.

- Hay que vivir sembrando, siempre sembrando.

- Por una mirada, un mundo. G. A. B.

**Sin verte tendrá
menos gracia el mundo,
la luna, el cielo, la piedra,
la playa, el parque, el cine
y todo. Cuando ya no estés
se habrá acabado el cuento.**